Fall 2019

Bison Simulation-Based Identification of Important Design Criteria for U3SI2 Fuels With Composite-Monolithic Duplex Sic Cladding

Jacob A. Yingling

BISON SIMULATION-BASED IDENTIFICATION OF IMPORTANT DESIGN CRITERIA FOR
U3SI2 FUELS WITH COMPOSITE-MONOLITHIC DUPLEX SIC CLADDING

by

Jacob A. Yingling

Bachelor of Science
Brigham Young University, 2014

_____

Submitted in Partial Fulfillment of the Requirements

For the Degree of Master of Science in

Nuclear Engineering

College of Engineering and Computing

University of South Carolina

2019

Accepted by:

Travis W. Knight, Director of Thesis

Elwyn Roberts, Reader

Cheryl L. Addy, Vice Provost and Dean of the Graduate School

Dedication

To my wife Rebecca, for her patience and long-suffering. To my brother, Erik, for his inspirational tenacity in his own academic pursuits. To my parents, Kirt and Joyce, for their mindset of growth and curiosity. And lastly, to Gwyneth Cravens author of, "Power to Save the World", who convinced me that nuclear power is the clear answer to our environmental and electrical power needs.

Acknowledgements

Travis W. Knight, who gave me the opportunity to pursue research while I was a distance student working to fulfill my military commitment to the Navy. Elwyn Roberts, for showing me how much I need to learn and how to ask the right questions. Theodore Besmann, for his advice, patience, and funding while I finished the later stages of this thesis in anticipation of working in his group with molten salts.

Abstract

Accident Tolerant Fuels (ATF) require a combination of fuel and cladding which have comparable longevity characteristics to UO2 while improving resistance to radiological release during and after accidents. U3Si2 has been proposed for use in ATF concepts for its high uranium density and high thermal conductivity which provide improved fuel performance. However, some of U3Si2's material properties are not well understood. One such property, thermal creep of U3Si2, is an important contributing factor to U3Si2's viability as an ATF. No experimentally derived thermal creep model is published for U3Si2, and previous analyses of compressive thermal creep experimental data lack statistical means of controlling for variability in the original data. This work uses previous compressive creep testing at the University of South Carolina to meticulously document the development of a thermal creep model for U3Si2 and implement that model in a BISON finite element simulation of a U3Si2 fuel SiC clad concept ATF. Rigorous statistical processes are used to ensure data are reproducible and reliable for use in the developed thermal creep model. This concept ATF shows significant delay to fuel-cladding contact when compared to traditional fuels of equal radial geometry and operational history. Sensitivity studies on fuel thermal creep rate, cladding thermal conductivity, cladding irradiation creep, cladding gap size, and cladding thickness demonstrate that research priorities for this concept ATF should revolve around reducing cladding thickness and improving U3Si2 plasticity.

Table of Contents

List of Tables

List of Figures

Chapter 1 Introduction

1.1 Motivation

High visibility nuclear accidents, such as have occurred at the Chernobyl, Three Mile Island and Fukushima Daiichi nuclear plants, have extreme long-term negative environmental and financial consequences. Considering the negative associations caused by the public upheaval and financial burden of remediating these nuclear incidents, it is evident why nuclear power has declined from its place of hotly pursued growth in the early 70s to an era of dwindling production and plant closures. Such accidents have been a motivating influence on driving governments to increase regulation which has in turn caused the international nuclear industry to seek improved methods and designs to help mitigate the environmental and public risk of operating nuclear power plants.

Internationally, the nuclear power industry needs to provide assurances that its plants can be operated safety. In the immediate aftermath of the 2011 Fukushima accident, international governments began a nearly wholesale reduction in use of nuclear power. Though current day nuclear usage has nearly returned to pre-Fukushima levels, questions regarding the safety of nuclear power have led several countries to adopt long term plans to reduce nuclear power in their energy portfolios. Germany, an especially evocative example, has reversed its position entirely, and enacted an entirely

non-nuclear strategy with a goal to eliminate nuclear power from their energy portfolio by 2022.

In late 2018, the Department of Energy awarded over 111 million USD to Westinghouse, General Electric, and Framatome to advance the development of Accident Tolerant Fuels (ATF). Each of these nuclear industry partners has conceptualized and developed plans for fuels designed to meet elevated fuel performance criteria under accident conditions. These fuels are to be compatible with existing nuclear plant infrastructure with a goal to create a drop-in replacement that can reduce the dangers of Loss Of Coolant Accidents (LOCA).

U_3Si_2 is among the fuels under consideration for use as an ATF. Its improved uranium density and thermal conductivity, compared to uranium oxide fuels, means it can provide improved performance while improving heat transfer under accident conditions. When combined with an advanced SiC cladding, with much lower oxidation potential at high temperature compared to zircaloy, these fuels exhibit greatly improved resistance to production of explosive gasses at elevated temperatures. Provided the SiC cladding barrier remains intact, this reduced chemical reactivity with the coolant results in less degradation of the fuel to coolant barrier leading to improved retention of fission products during accidents.

Despite these important advantages, the combination of U_3Si_2 fuel and SiC cladding is not a straightforward solution. U_3Si_2 characterization performed by Metzger at the University of South Carolina revealed that at low temperature, U_3Si_2 is prone to brittle chipping under regular handling conditions [1]. Additionally, U_3Si_2 is highly

reactive with oxygen and water which is counterproductive to the goals of ATFs should a cladding breach occur. SiC forms reaction products with U3Si2, which can cause the formation of brittle phases in the cladding. These reaction products would reduce the cladding's reliability during contact and make it more susceptible to failure. Given the drive of fuel manufacturers to use U3Si2, proper selection of a cladding that provides a large margin to failure comes of eminent importance.

To date, there are no in-pile data of a U3Si2 fuel with a SiC cladding. Indeed, current experiments are limited and have achieved only low burnups [2]. Further, no U3Si2 thermal creep mechanism is in the literature which limits U3Si2 fuel model accuracy under contact and high burnup. On the other hand, experimental data for SiC are readily available and important physical models have been developed for mechanical properties, irradiation response, thermal expansion, thermal conductivity, and irradiation swelling. Prior to full core testing of U3Si2 fuels with SiC cladding, a fully-coupled physical model needs to be developed to investigate the performance characteristics of this fuel-cladding combination under steady state and accident conditions.

1.2 Research Objective

Because of the anticipated advantages of this combination of fuel and cladding, but with an expectation of the difficulties that exist surrounding its development, a need exists for a predictive comparison between UO2-Zry and U3Si2-SiC fuels. To this end, finite element simulation methods are used to see how current day material property models regarding this combination of fuel and cladding perform relative to

expectations and the status quo. A research pathway can then be developed for fuel and cladding parameters that have the largest impact on predicted results. Researchers are benefited through identification of key design elements which focus their efforts on the most important areas for development of this concept ATF.

This research provides an analysis of a finite element model of U3Si2 fuel with a two-layer SiC cladding concept developed with the latest findings from the open literature. First in Chapter 4, a comparison of U3Si2 creep mechanisms is shown from models derived using in-house data from compressive creep testing at the University of South Carolina. Second, the performance of the proposed fuel/cladding combination is compared to a typical UO2 rod for typical dimensions of a Westinghouse 17 x 17 fuel assembly. Third, a parameter sensitivity study on U3Si2 thermal creep, SiC thermal conductivity, fuel-cladding gap, and composite SiC plastic compliance will show the effect of variance of these fuel property parameters on pellet clad mechanical interaction between U3Si2 and SiC. These studies under steady-state conditions provides an acute view as to the suitability of this fuel as an Accident Tolerant Fuel candidate.

The preceding give rise to the objective of this work which is to: (1) Develop a transparent data-driven grain size dependent model for secondary thermal creep of U3Si2. The developed model addresses concerns with the method's employed in earlier work. (2) Develop a finite element BISON simulation with best available material models to simulate the impact of U3Si2 thermal creep on fuel to clad contact. (3) Test the sensitivity of fuel to clad interactions on fuel-cladding gap, SiC thermal conductivity, and

the U3Si2 creep parameters developed in (1). Fuel manufacturers and researchers will

benefit from this work by having clear fuel and cladding design targets that have been

shown to optimize fuel performance of the U3Si2-SiC concept.

Chapter 2 Literature Review

2.1 Previous Work

 The University of South Carolina has developed U3Si2 models since 2016 when

Metzger completed a chemical and mechanical characterization of sintered U3Si2

pellets fabricated by Idaho National Laboratory (INL) [1]. Since U3Si2 has a significant

thermal conductivity and uranium density advantage over UO2 fuels, Metzger

developed a simple BISON finite element simulation of U3Si2 with a single layer of

monolithic SiC to quantify the extent of these material benefits [3]. Metzger's work

showed that U3Si2 with monolithic SiC cladding can deliver higher burnup, longer time

to PCMI, and lower peak fuel temperatures. Although her research provides a favorable

outlook on the steady-state performance of U3Si2, it lacked a U3Si2 thermal creep

model based on experimental data. Considering her observations of the brittle nature of

U3Si2 and SiC cladding, inclusion of thermal creep is of high importance to more

accurately predict strains within the fuel and cladding [1].

2.1.1 Thermal Creep Model

 Further work was completed by Mercado at the University of South Carolina to

address the need of a U3Si2 thermal creep model [4]. Mercado conducted compressive

creep testing of U3Si2 samples provided by INL at expected LWR temperatures and

stresses for U3Si2 fuel rods for similar geometries as the work completed by Stone [5].

Though Mercado had trouble in early testing with his experimental apparatus, his work

culminated in the development of an impressive compressive creep test rig and the production of reliable compressive creep data in later tests.

Mercado's early creep tests were often interrupted by equipment failure and a lack of PID temperature control led to sporadic temperature fluctuations. Despite these difficulties, every test conducted was used to determine creep parameters regardless of data quality. Further, Mercado did not provide any indication of the requirements for statistical discrimination among good and bad data or the conditions for which secondary creep was calculated. Mercado's challenges in early testing combined with a lack of documented procedure in data handling make it difficult to unquestionably accept the secondary thermal creep rate in U3Si2 he calculated especially in cases where tests have poor data quality. Despite these difficulties, his work developed an experimentally derived model for thermal creep of U3Si2:

$$\dot{\epsilon} = A\sigma^n e^{-\frac{Q}{RT}} \tag{2.1}$$
$$A = 8.78E\text{-}16 \qquad n = 1.94 \qquad Q = 168 \text{ kJ/mol}$$

Mercado's work is invaluable for its collection of raw creep data and early analysis of U3Si2 thermal creep parameters. However, his final creep model is calculated using all data points taken from his experimental research without regard to error incurred by the difficulties he experienced. To resolve these issues, Freeman implemented a reliable method of calculating creep rate using Mercado's data and developed a thermal creep model that excludes creep rate data from tests that failed early or were considered too short to be representative of secondary creep. Freeman's work was an important step forward in the analysis of Mercado's compressive creep testing and provides a

computational method using python scripting for reducing noise within the data.
Although Freeman's updated U3Si2 thermal creep rate results were documented in his
thesis, the details of his method for reducing noise in Mercado's data were never
adequately described in any published report. Freeman describes the thermal creep of
U3Si2 as:

$$\dot{\epsilon} = A\sigma^n e^{-\frac{Q}{RT}} \tag{2.2}$$

A = 2.5544E-22   n= 2.348   Q = 88.87 kJ/mol

Creep parameters determined by Freeman use an algebraic method described in
his thesis and relies upon assumptions that temperatures within 20K and 15 MPa are
the same [6]. Some tests were excluded for failure to meet a minimum creep time
specification of 100 hours. While algebraic methods for calculating creep parameters
are convenient, Freeman's assumptions indelibly propagate error to his creep model.
Also, his 100-hour creep requirement excluded important creep tests that will be shown
to reliably fit within the model developed in this present work. Additionally, Freeman
used a subset of his thesis creep rate data to develop a separate creep rate model for
use in his BISON accident tolerant fuel simulation. His reasons for using this U3Si2 creep
model based on a smaller data set is unexplained, and thus the use case for this thermal
creep model is unknown. However, since these creep parameters were used in
Freeman's BISON simulation, they have been taken by the community and are the
parameters that are currently in use in the BISON repository:

$$\dot{\epsilon} = A\sigma^n e^{-\frac{Q}{RT}} \tag{2.3}$$

A = 2.0386E-4   n= 1.2063   Q = 195.55 kJ/mol

The data used in the development of this model excludes all the later tests that have smaller total strain. The later tests are those which are of a different grain size and in general have more statistically consistent test data due to improvements in Mercado's compressive creep testing. For the purpose of developing a statistically relevant general use U3Si2 creep model, it is important to include the maximum amount of data possible from within the data that are considered reliable. A completely transparent approach to the development of a U3Si2 secondary creep model is implemented in this work to allow full understanding of the proper use case of the developed thermal creep model.

2.1.2 U3Si2-SiC Simulation

Freeman's BISON accident tolerant fuel simulation is a monolithic-outside composite-inside duplex SiC cladding concept as recommended by Stone [5]. The radial geometries for Freeman's simulation generally follow those used by Stone, which due to a large assumed cladding thickness, results in a larger exterior diameter of the simulated fuel rod and a smaller coolant channel. Modifications to exterior fuel geometries are to be avoided since they negatively impact thermo-hydraulic design considerations of the entire fuel package and may lead to hot channel violations in LWR designs. For the performance of an ATF simulation to be relevant to a comparison of its performance relative to existing UO2 fuels, the exterior thermal-hydraulic performance of the ATF must be comparable to existing fuel designs. External fuel geometry, therefore, must remain the same when comparing candidate ATFs against UO2 performance.

SiC and U3Si2 are under investigation and material models for simulating its performance continue to be developed. Since Freeman's work in early 2018 there have been developments in some of the material models used in his BISON simulation. Most importantly, irradiation creep of SiC was not included in Freeman's simulation based on the statement by Stone that irradiation creep is negligible within SiC [6]. However, although recent publications by Katoh and Koyanagi make it clear that irradiation creep has a relatively small effect, its influence isn't trivial and is important to accurately describe in-reactor mechanical behavior of SiC. In addition to the development of a U3Si2 creep model previously described, this work expands upon the simulation work done by Freeman to include this important irradiation creep material property along with other material property updates that have been made in the literature.

Proper finite element modeling of U3Si2 with SiC cladding depends upon correct application of the most up-to-date material properties already incorporated within the BISON code as well as adding new material properties that are not yet implemented in BISON. To inform the proper use of pre-existing BISON material models and the identification of models needing development or modification, a literature search of material properties of consequence to the finite element model was conducted. The intent of this search is not a complete assessment of the materials used within the BISON simulation but rather an identification of the neutronic, thermal-hydraulic, and mechanical properties of most importance to Finite Element Modeling.

2.2 U3Si2

U3Si2 has been used in aluminum dispersion fuels for many years for its high

uranium density [7]. Until recently, in reactor performance of U3Si2 was limited to

extrapolations from these research grade dispersion fuels. Based on dispersion fuel

testing, U3Si2 is expected to provide low fission gas release and low swelling in

comparison to UO2 [8]. Although the long-term performance of U3Si2 is still unknown,

recent low-burnup post irradiation examinations of U3Si2 fuel fabricated and tested at

INL have validated the expectations set by dispersion fuel analysis [2]. Relative to typical

UO2 performance, U3Si2 demonstrates improved cracking and relocation behavior as

well as structure and phase stability under irradiation. U3Si2 also has low migration of

fission products and resists hardening from swelling strains and irradiation damage.

Overall, experimental evidence suggest U3Si2 is capable of being used in LWRs under

steady-state conditions. No testing of U3Si2 under accident conditions has been

completed.

Some properties of U3Si2 are well known and are collected in the Update to the

U3Si2 Property Handbook by Los Alamos National Laboratory. This document was used

as a baseline on a more thorough search to ensure the most recent data are used. Many

computational studies have calculated predicted U3Si2 material properties, however,

material models based on experimental data are preferable and were chosen for use

within this paper's BISON modeling whenever available.

2.2.1 Density and Thermal Expansion

U3Si2 has a uranium density 16.4% higher than UO2, 11.3 kg-U/m^3 compared to

9.7 kg-U/m^3. Its theoretical density is 12.2 kg/ m^3 with powder sintered pellets produced

at INL reaching 94.7% theoretical density and arc melted plasma sintered samples

reaching 96% theoretical density [9]. Thermal expansion of U3Si2 was most recently

found by Obbard to have a negative deviation with temperature. The linear thermal

expansion coefficient is:$\alpha(\text{T}) = 2.1 \times 10^{-5} - 7.25 \times 10^{-9} \cdot \text{T}$ [10].

Currently within the BISON codebase, densification of U3Si2 is expected to be

like UO2 and is handled using the ESCORE model [11]. However, little to no densification

of U3Si2 due to irradiation effects and high temperature in-pile sintering was found in

recent testing at INL [2]. Given that UO2 completes its period of densification within

10GWday/MTU, the 20 GWday/MTU burnup of the INL post-irradiation examination

would have been sufficient to reveal any densification in U3Si2. To conservatively reveal

any performance difference between UO2 and U3Si2 densification within U3Si2 is not

included in this work.

2.2.2 Melting point, Specific Heat and Thermal Conductivity

U3Si2 has a melting point of 1938K and has a lower thermal conductivity than

UO2 at room temperature. Since its thermal conductivity rises with temperature as

opposed to UO2 which has a progressively lower thermal conductivity as temperature

rises, U3Si2 has a considerable heat transfer advantage when at power. Ranges of

values for the coefficient of thermal conductivity differ based on fabrication technique

and research group, but the empirical relation taken from the U3Si2 handbook is a good

high and low temperature fit to data from sintered U3Si2 [3] Similarly, the handbook

provides an updated value for the specific heat capacity. Both these models are

currently available in the BISON codeset.

2.2.3 Swelling and Fission Gas Release

Low burnup post-irradiation examinations of U3Si2 under LWR conditions have allowed the comparison of computationally derived fission gas release models to experimental data [12]. At low burnup of 7.3 GWd/MTU, these models calculate total fission gas swelling within about 15% of the measured value, an expected amount of error for computational theory derived models. As such these models would seem appropriate for order of magnitude estimates of fission gas swelling at low burnup. This swelling and fission gas release model has already been implemented in the BISON codebase and is unmodified for use in this work.

While this U3Si2 swelling model is reasonably accurate, fission gas release was measured to be less than half of the calculated value. A recently completed post-irradiation examination at INL is expected to allow further refinement of this model and shows a similarly lower than expected amount of gas release [2]. For the present work it is understood that while the calculated amount of swelling is within acceptable limits of a demonstrative example, fission gas release is expected to be much lower than calculated.

2.2.4 Elasticity and Thermal Creep

Porosity dependent elastic and shear moduli have been determined for arc cast samples of U3Si2 by Shimizu and have been deemed approximately accurate by more recent studies by Mohamad and Carvajal-Nunez at fixed porosities [3]. A more recent study of porosity dependent moduli is needed based on modern fabrication strategies but for the present work the approximate elastic and shear moduli are enough to provide a general indication of elastic behavior of U3Si2 in simulation. Least square fits

13

to the combined porosity dependent elasticity and shear moduli are already in place in the BISON codebase.

Lacking from the literature is a thermal creep model for U3Si2 under LWR conditions. Early theoretical work by Metzger, experimental compressive creep work by Mercado and early analysis of these data by Freeman at the University of South Carolina provide a baseline thermal creep model for use in finite element modeling of U3Si2 based ATFs. Lacking from this earlier work is a detailed development of the precise standards and statistical requirements used in the production of a final U3Si2 thermal creep model. Considering the importance of creep to the performance of nuclear fuels, this lack of developed data is a large gap in the understanding of how valid the use of U3Si2 as an accident tolerant nuclear fuels is and how they will perform under steady state and accident conditions.

Beginning in 2015, the University of South Carolina developed an initial characterization of U3Si2 [1]. In 2018, compressive creep testing of INL fabricated pellets allowed the determination of an initial thermal creep model [4, 6]. At the conclusion of these works a thermal creep model was presented using a small subset of the total available data. The reasons for excluding large amounts of test data and the specific methodologies employed in the analysis of the raw creep data were not documented. Further, the results of these studies lack a firm determination of the suspected thermal creep mechanism.

A major goal of this work is to thoroughly document the processes used in the development of a statistically rigorous empirical model of thermal creep in U3Si2 in the

range of conditions covered in the previously accomplished studies. Additionally,

various mechanisms of creep will be investigated to elucidate whether determination of

a mechanism-based creep model is possible.

2.2.5 Fuel Fracture and Relocation

Very few data are available on the cracking and relocation of U3Si2. Despite an

abundance of aluminum-based research and test reactor dispersion U3Si2 fuels, to date

only low burnup irradiation of LWR grade U3Si2 fuel has been accomplished [2]. These

studies agree that rise to power cracking of U3Si2 tends to be lower than expected for

UO2.
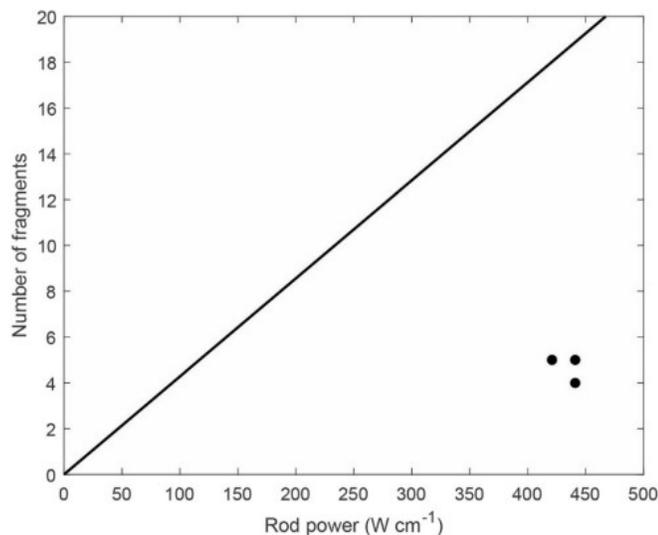
Figure 2.1: U3Si2 cracking relative to expected adapted
from Cappia [2]

Figure 2.1 above shows data from the INL study indicating that at 20 GW-

day/MTU U3Si2 forms about 4.6 fragments on average where UO2 would form about

18.4 fragments [2]. This relative cracking creates a ratio of about 0.25 U3Si2 fragments

for every UO2 fragment created during rise to power. To a first approximation, it may be

expected that this UO2 normalized cracking factor encapsulates the combined

differences between UO2 and U3Si2 with regard to thermal conductivity, thermal

expansion, fracture toughness, and elasticity as they relate to the propensity for U3Si2

to crack.

Since this factor incorporates many condition dependent material properties, it

is expected to be acceptable for use only in the range of conditions established during

rise to power of the INL experiment. The simulated conditions of the present study of

temperature, pressure, and fuel geometry are similar to those of the INL tests with the

exception of the power density of the experiment being much lower. However, since the

operating temperatures are similar, the majority of relative cracking stresses are

expected to be comparable. Thus, for this research cracking and relocation models

developed for UO2 can be used in BISON modeling of U3Si2 when offset by this cracking

factor.

Relocation of UO2 has been understood for many years and is best modeled

using the modified ESCORE model developed by Kramman and already in use in the

BISON codeset. Under the current assumption for U3Si2 cracking, since fuel relocation is

a function of the extent of fuel cracking, U3Si2 may be expected to relocate

proportionately less than UO2 by the same factor determined above for cracking.

2.3 SiC

Selection of an appropriately non-reactive cladding for use with U3Si2 is a key

aspect of accident tolerance. Much research has focused on the use of U3Si2 in

combination with either chromium coated zircaloy or FeCrAl cladding. These claddings

provide reduced chemical reactivity under accident conditions but at a cost of reduced

neutron economy [13]. Development of improved monolithic-composite duplex SiC

claddings has renewed interest in its use as an ATF cladding.

Monolithic and Composite SiC material properties have been extensively studied

and their material properties have been collected in various reports. Since composite

SiC fabrication technique has such a large impact on its materials properties, this

literature review aims to ensure that the material properties presented for inclusion in

the BISON simulation have been gathered for materials that are similar in terms of

fabrication technique.

Different arrangements of SiC claddings have been proposed for use in accident

tolerant fuels. Based on the findings of Stone and others, this work uses the

combination of an inner layer of CVI composite SiC cladding to reduce the hoop stress of

the more brittle monolithic CVD outside layer of the cladding which allows for

hermeticity under load [5]

It is important to note that while the material properties of monolithic SiC are

consistent among polycrystalline variants, significant differences exist among the

various forms of CVI composite SiC [14]. These differences are due to variations in the

method of fiber winding, fiber winding angle, fiber coating and weave method. Since no

single document can provide authoritative material properties consistent among the

many forms of CVI composite SiC, the properties here should be viewed as

representative of average behavior and not a precise model of a single CVI composite.

Thus, the BISON simulation that follows must similarly be viewed only as representative

of typical behavior and not of any existing CVI product.

2.3.1 Elasticity and Compliance

Monolithic SiC is a super high strength material ideal for use in high temperature and stress environments. Its highly crystalline structure makes it susceptible to brittle failure requiring it to be coupled with a composite layer of SiC for nuclear applications where "graceful" failure mechanics are essential. The environmental barrier monolithic SiC assumed in this study is polycrystalline with a temperature and porosity dependent Young's modulus given by Snead [14]. This behavior for monolithic SiC is already incorporated into the BISON codeset, however, since this material model is limited to temperature effects it needs to be modified to account for softening from irradiation that can reduce the young's modulus by as much as 10% [14].

Composite CVI SiC is a more compliant material due to the designed microcracking of the composite SiC matrix prior to loading of SiC fibers. These features allow composite SiC tubes the benefit of plastic like mechanical behavior under load. Several laboratories evaluated the axial properties of composite SiC tubes and determined tubular composite SiC to have a UTS of 236.5 MPa and a PLS of 92.8MPa with a Young's modulus of 201.9GPa [15]. Stress strain data averaged among the various laboratories shows axial strain hardening behavior of composite SiC reminiscent to plastic deformation in metals as the composite matrix cracks above the PLS. Unlike metals, however, strain hardening quickly saturates and the stress strain relationship becomes linear until fiber failure.

While the above is true for uniaxial continuous stress. Composite Matrix Ceramic (CMC) materials have unique characteristics when placed under dynamic loading and unloading. Typically when a hard material plastically deforms, upon relaxation its

Young's modulus remains unchanged. Further cycles of elastic loading and unloading follow the same slope in the elastic region though offset by the amount of plastic strain that has occurred. Composite SiC, a CMC, has been observed to damage the original Young's modulus when thresholds of stress have been exceeded [16]. Since no damaged based relaxation model exists within the BISON codebase, this capability is developed in Chapter 3.

Anisotropy in the mechanical material properties was recently investigated by Singh et al [17]. Radial elasticity modulus is only a third of the axial value, while hoop elasticity is similar to axial. Due to limitations in the coupling of isotropic plasticity tensors with anisotropic elasticity tensors in BISON, this work acknowledges the need for further development to include anisotropic elasticity in future modelling. However, since axial and hoop stresses are of greatest concern in evaluating cladding performance and failure probabilities, this work uses axial composite SiC mechanical properties in isotropic elasticity tensors for its BISON simulations.

The SiC-SiC Material Property Handbook indicates that irradiation effects on mechanical properties of composite SiC are insignificant [18]. However, more recent evidence suggests that the degradation of axial Young's modulus is about 18.4% [17]. As in the case of monolithic SiC, this reduction is expected to follow irradiation swelling and saturate prior to 2 dpa.

2.3.2 Thermal Conductivity

Katoh found that the thermal conductivity of monolithic and composite SiC are highly dependent on the amount of irradiation damage that a fuel has received [19].

This effect was later developed into a model by Stone for monolithic and composite SiC that has been used in previous BISON simulations [5]. Stone's models are convenient for use in BISON modeling but are based on SiC plate data, rather than tube geometries. Since monolithic SiC material properties are less structure dependent as compared to composite SiC, Stone's plate specimen thermal conductivity models for monolithic SiC are adequate and used in this work.

However, in CMC materials thermal conductivity is highly structure dependent and will not be well represented by a single model [18]. Accurate thermal conductivity is needed to better approximate the temperature profile through the fuel. Rather than rely upon plate specimen thermal conductivity, thermal diffusivity data collected by Koyanagi for tubular composite SiC allow for thermal conductivity calculations that are more generally representative of tubular composite SiC [18]. The present simulation will modify Stone's irradiation dependent composite SiC thermal conductivity models to include tube specimen data as provided by Koyanagi.

2.3.3 Irradiative Swelling

A fully descriptive low-burnup study of the irradiation swelling behavior of monolithic and composite SiC has been done by Katoh [20]. SiC has a high degree of swelling that saturates at approximately 1 dpa. Composite SiC is found to have anisotropic swelling with similar axial swelling as monolithic SiC but with measurably less radial swelling in composite SiC. This difference in swelling rate is expected to cause compressive stresses within the composite layer and tensile stress within the monolithic layer of a duplex SiC cladding.

2.3.4 Creep Compliance

SiC undergoes primary thermal creep upon initial loading in cases of extremes in loading and temperature but secondary thermal creep is nearly zero for all but the most elevated stress conditions [14]. Since the observation of primary creep is limited to worst case conditions that are unlikely to be seen by the cladding at LWR conditions, this work assumes primary and secondary thermal creep of SiC to be negligible.

Irradiation Creep in SiC is similar between monolithic and composite variants and is less than other cladding materials [21]. This behavior lends to the high stability of SiC and suggests that time to contact with the fuel will be extended. Work by Koyanagi suggests a swelling coupled region of primary irradiation creep through 1 dpa followed by a steady secondary creep thereafter [21]. This work by by Koyanagi, however, was done using the Bend Stress Ratio technique on monolithic CVD SiC as well as composite SiC fibers which was acknowledged in his later work to be complicated and prone to inaccuracy though properly demonstrative of creep mechanism. Generally, tensile irradiation creep determined via BSR technique was found to be more than an order of magnitude lower than in-reactor tested SiC tubes [22].

Creep compliance (K) for swelling coupled irradiation creep found by Koyanagi, Equation 2.5, is comparable in magnitude to steady-state irradiation creep found by Lewinsohn in Equation 2.6 [23], thus the combined irradiation creep is described as the sum of transient and steady creep, Equation 2.4.

$$\dot{\epsilon}_{irr} = \dot{\epsilon}_{transient} + \dot{\epsilon}_{steady} \qquad 2.4$$
$$\dot{\epsilon}_{transient} = K_1 \cdot \sigma \cdot \dot{S} \qquad 2.5$$
$$\dot{\epsilon}_{steady} = K_2 \cdot \sigma \cdot \phi \qquad 2.6$$

Koyanagi's models are expected to be only an initial description of irradiation creep since they were determined using BSR data from small SiC fibers rather than tube specimen. Further in-pile creep tests were accomplished in the Halden BWR for monolithic CVD SiC tube specimen that show a much higher amount of creep strain under similar temperature conditions [22]. This result combined with the structure variability of the BSR creep data indicate that irradiation creep of SiC is highly dependent on structure and loading scheme.

2.3.5 Thermal Expansion

The foregoing has shown that most SiC material properties have some irradiation dependence. Research by Snead and Koyanagi et al., however, show that thermal expansion in SiC is a property inherent to the material and independent of any outside influence [24]. There are few tube specimen SiC thermal expansion data available, but due to the inherent characteristics of thermal expansion, existing plate specimen data are sufficient for modeling purposes [19].Instantaneous Coefficient of Thermal expansion is very similar between monolithic and composite [19]. A best fit model for calculating the CTE for monolithic CVD and composite CVI types of SiC was found by Katoh that has already been implemented into the BISON codeset.

The preceding collection of U3Si2 and SiC material properties give a basis for the development of a thermal creep model for U3Si2 to be implemented with the material models discussed in this chapter in a full physics BISON simulation. Chapter 3 provides the thought process and assumptions in the development of this BISON simulation.

Chapter 3 Methods

U3Si2 is an intermetallic with mechanical properties between those of a metal and a ceramic [25]. Computational studies predict the electronic structure to conform more similarly to metallic than ceramic structures [26]. As a result, creep behavior of U3Si2 is likely somewhere between that of ceramic UO2 and vanadium, a metal with similar young's modulus and melting point to U3Si2. Ashby diagrams are provided in Figure 3.1 for these two materials to show general creep regime trends at normalized stresses and temperatures for typical LWR conditions [27]:
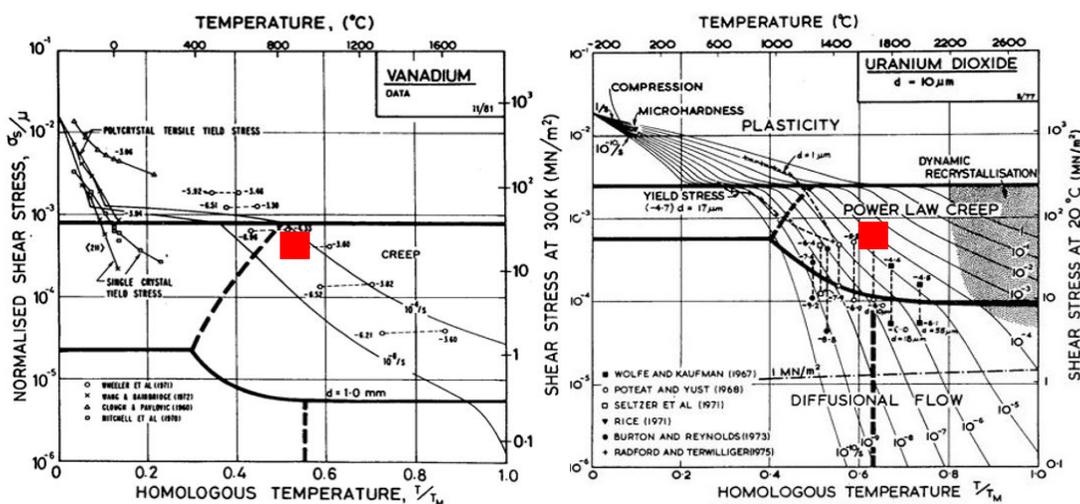

Figure 3.1: Creep regimes adapted from Ashby [27]

Previous BISON tests with typical PWR conditions have shown U3Si2 centerline temperatures to operate in the range of 940K to 1100K and fuel stresses to be higher

than 50 MPa. These conditions are in line with those used during Mercado's U_3Si_2 creep

testing with temperatures between 850 to 1000°C and stress between 25 to 80 MPa.

Considering the melting temperature of U3Si2 is 1938K [1] and its shear modulus to be

67.68 GPa [26], if U3Si2 thermal creep behaves as a compromise between Vanadium

and UO2, we can expect the creep mechanism to follow a power law mechanism.

T/Tm=0.51 and σ/G= 7E-4 indicated by red box in Figure 3.1.

The form for power law creep is generally taken as $\dot{\epsilon} = A\sigma^n e^{-\frac{Q}{RT}}$ with n>3. U_3Si_2

is tetragonal in the P4/mbm space group consistent with the Cu_3Au structure with two

Si atoms in the Au site [26]. Our prediction of power law creep is further enhanced by

the fact that other intermetallics of the Cu_3Au structure are clearly in the power law

creep regime with n=5 [28]. Intermetallics of the Cu3Au structure typically follow the

"Cu3Au Rule" where the creep activation energy is closely related to the dominant

species self-diffusion energy [28]. This rule generally holds true for Cu_mAu_n where

m/n>2. Replacement of the metallic single atom Au site with crystalline Si may

contravene this rule to create unexpected creep modes in U3Si2. In addition to

verification of the stress exponent, creep activation energy consistent with the uranium

self-diffusion energy would indicate creep behavior that fits within the expected

behavior envelop of Cu3Au solids.

3.1 Development of Thermal Creep model

The equation for power law creep can be linearized as $\ln\left(\frac{\dot{\epsilon}}{\sigma^n}\right) = -\frac{Q}{R}\frac{1}{T} + \ln(A)$.

When a variety of data for $\dot{\epsilon}$, σ, and temperature are available, the coefficients A and Q

can be found by iterating over values of n and calculating a least squares linear fit by

plotting $\ln\left(\frac{\dot{\epsilon}}{\sigma^n}\right)$ against $\frac{1}{T}$. Despite the expected power law creep outcome, an analysis

is conducted which elucidates the creep behavior of U3Si2 based on existing data.

Rather than evaluate the creep parameters under an assumed creep mechanism, the

compressive creep data will be fit using the generalized Mukherjee-Bird-Dorn equation,

$\dot{\epsilon} = \frac{AGb}{kT}\left(\frac{b}{d}\right)^m \left(\frac{\sigma}{G}\right)^n D_0 e^{-\frac{Q}{RT}}$, which reduces to Equation 3.1 below where $A' = \frac{Ab^{m+1}D_o}{kG^{n-1}}$

[29]:

$$\dot{\epsilon} = \frac{A'}{T}\frac{\sigma^n}{d^m} e^{-\frac{Q}{RT}} \tag{3.1}$$

This equation is capable of accounting for dislocation and diffusional type secondary

creep through its incorporation of stress, temperature, and grain size dependent

factors. When Equation 3.1 is linearized, A' can be calculated directly from regression.

Use of Equation 3.1 will provide an indication of which mechanism is the

dominant U3Si2 creep mode from Mercado's 2018 experiment which follows based on

the determined creep coefficients for m, n and Q. Once the mechanism of creep has

been loosely established using Equation 3.1, the proposed creep mechanism can be

verified, and a final creep model established.

Data for determining creep coefficients for U3Si2 come from Mercado's

compressive creep testing. His experiment covered a range of temperature, stress, and

total axial strain applicable to expected LWR conditions. A total of 13 tests were

conducted among five different U3Si2 pellets. Creep strain, temperature, stress and

pressure vs time data from Mercado's experiment are included in Appendix A. The five

pellets of U3Si2 from Mercado's experiment come from Batches 3 and 4 received from

INL [1]. The difference between Batches 3 and 4 is that during fabrication, Batch 3 wasn't pressed within two weeks, which may have led to the formation of additional phases within the bulk U3Si2. Phase inconsistency has been identified as a possible cause of U3Si2 mechanical property deviations, fracture toughness for example, between Metzger and later works[9].

3.1.1 Explanation of Original Creep Test Sequencing

To obtain data that adequately represents creep rate, a variety of testing conditions are required. Among the possible creep rate mechanisms, the creep rate is generally a function of stress, temperature, and grain size. To adequately capture the mechanism of creep, a minimum of three tests must be conducted to satisfy the following requirements. 1) Constant temperature with an increase in stress 2) Constant stress with an increase in temperature. 3) A comparison of tests between two pellets which follow 1 or 2 above and vary in grain size.

Among the five U3Si2 pellets, multiple creep tests were conducted on each pellet for a total of 13 tests in the following scheme. The reader is referred to Appendix A for data plots of his original experiment [4]:

Pellet 1 (Sample 150813a): Test 1 and 2 were held at constant temperature to evaluate the effect of varying stress while maintaining a constant temperature. PID temperature control was not yet implemented for these tests, however, a python scripting method to eliminate statistical deviations is described later to allow this test to satisfy requirement 1. Test 3 is not applicable for use in the creep model since a power failure caused Test 3 to end prematurely.

Pellet 2 (Sample 150813b): Test 4 and 5 were intended to evaluate the effect of raising temperature against a constant stress, however, the relatively high creep rate found in Test 5 in combination with a slight decrease in applied stress resulted in a large amount of reduction in true stress. This large variation in true stress in Test 5 prohibits these tests from satisfying requirement 2. However, the smooth variation in stress state in Test 5 provides an interesting opportunity to use subsets of data within the Test 5 for model determination purposes.

Pellet 3 (Sample 161214b): Test 6 and 7 improve upon the result of Test 4 and 5 and hold a relatively constant true stress state in combination with a much larger increase in temperature. The tests of Pellet 3 satisfy requirement 2.

Pellet 4 (Sample 161214a): Tests 8, 9 and 10 hold temperature constant with a sequential increase in true stress. The tests of Pellet 4 satisfy requirement 1.

Pellet 5(Sample 161214c): Tests 11 and 12 hold true stress steady with a large increase in temperature which provide another set of data for validation of requirement 2. Test 13, greatly increases true stress while maintaining temperature the same as Test 12 which helps in the validation of requirement 1.

Note that there is no combination of tests that are exactly compatible with requirement 3. However, even though the temperature and stress states between the tests in Pellet 1 and Pellet 4 are not the same, the type of testing, vis., steady temperature with an increase in true stress, allows these two pellets to be used to satisfy requirement 3. Importantly, the combination of these tests provide ample data

that satisfy the necessary requirements for production of a secondary creep model using Equation 3.1.

3.1.2 Primary Creep

Insufficient statistically reliable data are available to develop a primary creep model that is representative of all creep tests conducted. Lack of PID temperature control creates the appearance of primary creep in Tests 1-2 that is caused by significant drops in temperature throughout those creep tests. Test 4 does not have any clear region of primary creep, and while Test 5 appears to have a region of primary creep, the change in creep rate is caused by a drop in applied stress.

Test 6 and 7 were completed on the first pellet used with PID temperature control and show a clear region of primary creep in Test 6 and no primary creep in Test 7 after an increase in temperature. It is obvious from Test 6 that primary creep is completed after about 130 hours of testing and that an increase in temperature between Test 6 and Test 7 is insufficient to reintroduce primary creep in Test 7. Test 8 was complicated by a lengthy seating process that obfuscated any primary creep that may have occurred.

Despite these data quality problems which prevent development of a primary creep model, it is possible to obtain information about the total contribution of primary creep in certain tests. For the first tests in each pellet, with consistent temperature and stress data, the total contribution from primary strain can be determined by finding the y-intercept of a least squares fit of the steady state strain equation. Thus, if the total creep strain had only been due to secondary creep, the y-intercept of the fit strain

28

equation would be zero. When the secondary creep rate follows a measurable amount

of primary creep, then the y-intercept of the secondary creep equation represents the

amount of primary creep strain prior to onset of secondary creep.

Overall, the data show a small contribution to overall strain from primary creep.

Tests in which primary creep may have been visible were Test 1, 4, 6, 8, and 11. Using

the method described in the previous paragraph, the contribution to total creep was

determined for Tests 4, 6, and 11. As previously mentioned, problems within the data in

Test 1 and 8 make these tests unsuitable for use in determining primary creep.

Contributions from primary creep to total strain were 0.009, 0.005 and 0.003 for Tests 4,

6 and 11 respectively which represent a less than 5% of the total creep in their

respective pellets. Thus, the effect of primary creep is considered negligible in this work.

The reader is referred to Appendix A for a collection of strain data as calculated using

the python scripting methods described later in this chapter.

3.1.3 U3Si2 Grain Size

Determination of post-creep grain size is currently underway at the University of

South Carolina. Without any report with conclusive evidence of a grain growth model,

the calculations in this work will be determined based on archival work by Coleman

Terrapin for pre-creep grain sizes of each creep tested pellet. Notably the U3Si2 pellets

were discovered to have a radial grain size dependence. Therefore, the archival grain

sizes used for this work are the average of the center and outer edge grain diameters for

each pellet which are 15.6um for Tests 1-6 and 26um for Test 7-13.

3.1.4 Pre-strain on Multistage Creep Experiments

Care must be taken while interpreting the data in Mercado's creep tests. Multiple tests were conducted upon each pellet, therefore, the effect of pre-strain on tests that followed the first test in each pellet must be considered. The effect of pre-strain on secondary creep is highly material dependent. In most cases, such as among various grades of steel, pre-strain has the effect of creating hardening dislocations which reduce creep rate [30]. Other metals, such as copper, experience strain hardening and loss of creep ductility in pure samples but in samples that contain oxygen the loss in ductility is offset by the creation of cavitation voids which result in increased creep rate.

Traditional nuclear fuels such as UO_2, a ceramic, are sufficiently brittle that strain hardening can be neglected during compressive creep testing. By contrast, the structure of U_3Si_2 gives it metallic properties and so it is expected to strain harden throughout testing. Since the intent of this work is to provide a thermal creep model for use in simulating the performance of U_3Si_2 as a LWR nuclear fuel, the nature of this use case presupposes the need to understand long-term creep behavior under high burnup conditions where the fuel is understood to have undergone some pre-strain. Therefore, a creep model that properly describes the long-term creep behavior of U_3Si_2 must necessarily include any expected strain hardening that will occur.

3.1.5 Python Scripting Method of Calculation of Strain Rate, Temperature, and True stress

The present work relies upon the same raw time-dependent temperature, true strain, and true stress data that was collected by Mercado and verified by Freeman. The reader will note small differences in the calculated true strain rate, average

temperature, and average true stress found in this work when compared to the results found by Freeman and Mercado. These differences come from variations in the number of raw data points used to determine the strain rate as well as the specific range of time over which the strain rate was calculated for each test.

Mercado's results were provided with minimal indication of the conditions over which secondary creep rate was calculated. Also, while Freeman does indicate some of the general conditions over which his results were determined, his results cannot be reproduced without use of his python scripting tool with built-in conditions much more specific than outlined in his thesis. Rather than substantiate the differences between previous and current results, the present work provides a new set of calculated average strain rates for secondary creep, average temperature, and average true strain along with a detailed explanation of how the raw data were treated for calculation of these average values. Generally, these data are calculated using the same tool as developed by Freeman with some modification using the analysis parameters explained below.

Average strain rate is determined for each test through use of python scripting. Since each U3Si2 pellet was used to facilitate multiple tests, careful treatment of the raw data are needed to allow calculation of secondary creep rate without including data during primary creep modes, transitions between tests, and other data anomalies present due to difficulty in the original experiment. For every test, three analysis parameters are specified to ensure proper and repeatable calculation of average creep rate among an inconsistent data set. Python variables for these parameters are

provided in parenthesis and a python 2.3 code template is provided in Appendix B for

reader reference:

- Sample Seating Skip Time (sample_seating): The length of time skipped at the

  beginning of a pellet's first test. This parameter is needed to skip any primary

  creep that may be present in the initial portion of a pellets testing and resolve

  any issues with sample seating. This parameter is generally 130 hours or more

  for each test as determined from the apparent primary creep of Test 6.

- Transition Skip Time (skip_time): The length of time skipped when transitioning

  between tests. This parameter is at least 20 hours to avoid anomalous data

  during equipment adjustment to new loading conditions.

- Required Test Time (time_frame): The total length of time over which the

  average creep rate, average temperature, and average true stress are calculated.

  This parameter is generally in excess of 100 hours for most tests. However, Test

  8 and 10 are special cases where statistical analysis show reliable steady state

  data for a somewhat shorter period of time. For these tests respectively, 65 and

  82 hours of Required Test Time were specified.

Due to experimental difficulty, the raw data of some tests do not present an

obvious region of secondary thermal creep. This difficulty in the data is overcome by

specifying the analysis parameters described above for each test. The script finds the

highest correlating average true strain rate for each test among the remaining data not

excluded by Sample Seating Skip Time and Transition Skip Time. It does this by finding

the average true strain rate over a length of time equal to the Required Test Time that

provides the highest correlation coefficient (r). In this way the script can find the best average creep rate agreement to the data from within a larger range of available data.

For each highly correlated average strain rate the same range of data points are used to calculate an average temperature and average true stress. Due to a high amount of variability in the temperature and stress data of some tests it is necessary to ensure that the average temperature and stress determined for the highly correlated strain rates is over a range of similarly well correlated temperature and stress data. To accomplish this, a limit to the acceptable amount of variation in the data is established.

The Coefficient of Variation (CV), the ratio of the data's standard deviation to its arithmetic mean, is a common statistical measure of data variation. Average temperature and true strain for the calculated values for strain rate were required to have CV of less than 3.5% to guarantee strain rates were only calculated for ranges of data with consistent values of temperature and stress. This requirement ensures that the mean normalized standard deviation of the temperature and stress data over the range of calculated strain rate values remain close to the average temperature and average stress. This strategy greatly improves creep model development over previous work by guaranteeing well clustered temperature and stress data for each calculated strain rate.

In summary, the calculated average strain rates, average temperatures, and average true stress were calculated based on the following requirements:

(1) Fit within a timeframe equal to Required Test Time and outside the time excluded by Sample Seating Skip Time and Transition Skip Time.

(2) Average strain rate must have a coefficient of correlation greater than 0.90.

(3) Average temperature and true stress must have a CV less than 0.035.

A collection of average strain rate, average temperature, and average true stress graphs overlaid on the raw testing data are provided in Appendix A. A summary of the data calculated using the scripting strategy described above is found below in Table 3.1:

Table 3.1: Summary of calculated strain rate, temperature, and true stress

Test #	Creep Rate (1/s)	Average Temperature (K)	Average True Stress (MPa)
1	8.7327E-8	1218.37	44.10
2	1.1342E-7	1205.18	71.77
3	N/A	N/A	N/A
4	1.7042E-8	1121.22	77.66
5-A	1.3081E-7	1223.89	65.13
5-B	6.4806E-8	1210.07	57.71
6	1.5728E-8	1173.59	46.43
7	4.6342E-8	1223.59	45.21
8	1.5486E-8	1223.60	29.51
9	2.7472E-8	1223.53	49.73
10	7.1920E-8	1223.64	63.62
11	1.1171E-8	1223.69	26.91
12	1.8750E-8	1273.61	26.45
13	2.9831E-8	1273.61	47.79

Test 5 was unique due to a large amount of true stress variation over the course of the test. This large true stress variation provides an opportunity to extract more than one set of data for use within the model. Two ranges of data that meet the requirements described above were observed in the range of data not excluded by Transition Skip Time and that provide enough Required Test Time. Hence two different average strain rates were calculated from Test 5. These have been denoted Test 5a and Test 5b.

The creep parameters A, Q, m, and n are determined from the data in Table 3.1 by linearizing Equation 3.1 and plotting $\ln\left(\frac{\dot{\varepsilon}Td^m}{\sigma^n}\right)$ against $\left(\frac{1}{T}\right)$. Once linearized in this form it is possible to directly calculate the values of A and Q for a combination of m and n. There is a relatively small number of possible combinations of m and n with m in the expected range of 0.00 to 3.00 and n in the expected range of 1.00 to 7.00 which allows each combination of m and n to be determined computationally and evaluated using standard statistical fitness techniques described below.

Generally, in linear regression statistics r^2 approaching unity indicates the model perfectly describes variation in the data. It is a measure of how tightly the data adhere to the model. A large r^2 indicates a model that accurately describes variation in the data, but r^2 alone does not provide an indication of model validity since it cannot indicate the likelihood of the correlation occurring by chance. To test whether the model is likely to have represented the data by random chance, two-sided p-values were determined at the 0.01 significance level. In regression statistics this means that an established null-hypothesis of no correlation between the data and the regressed line (zero slope) can be rejected for p-values less than 0.01. For any p-value less than 0.01 we could expect the model to give a similarly good agreement due to random chance in only 1% of similar experiments. A smaller p-value is generally consistent with a model that is less likely to fit the data due to random chance.

For each combination of m and n, the r^2 and p-value is calculated for the linear form of the creep data tested against the linearized form of the creep model. Since the p-value is a measure that indicates confidence to reject the null-hypothesis, the null

hypothesis being that the slope of the linear regression does not correlate to the data, for p-value<0.01 we can confidently reject the null hypothesis. Thus, p-values less than 0.01 indicate that the calculated values for A, Q, m, and n provide a strain rate calculated from a statistically significant model. Provided the test for significance is met, higher r^2 indicates a more accurate model.

3.2 BISON Material Models

Finite element analysis methods were used to determine the impact of the developed U3Si2 secondary thermal creep model on the performance of the concept ATF. BISON is a finite element analysis code that has been thoroughly described by others in the development of fuel performance models. Metzger and Freeman used BISON to produce U3Si2 fuel SiC clad simulations in varying levels of model complexity [6] [1]. The model provided in this work is an improvement with respect to physical geometry as well as material models that have been developed or updated by various authors.

Based on the information obtained during the literature search performed in this work the following material models and physical properties are deemed most appropriate for inclusion in the BISON simulation based on the merits of each described in Chapter 2. Based on the author's search of the relevant literature they are believed to be the most up to date material models available at the time of writing. Material models that are used as provided by the various authors will not be further described in this section. For that purpose, the reader is referred to the various cited works of Chapter 2. However, key assumptions for each material model that have been modified are

described here to provide the reader with a transparent view of the methods used in developing this BISON simulation.

3.3 U3Si2 material models

3.3.1 Thermal Creep

Chapter 4 details the development of a thermal creep model for U3Si2. Different creep modes are investigated in Chapter 4 to provide models suitable to conditions where creep must be calculated using a mechanistic model outside the range of available experimental data. However, since the conditions of the BISON simulation in this work stay within the bounds of Mercado's original experiment, the Mukherjee-Bird-Dorn empirical relationship is adequate for the simulation in Chapter 4. Equation 3.1 is reproduced below for convenience along with its creep parameters provided in Table 3.2

$$\dot{\epsilon} = \frac{A' \ \sigma^n}{T \ d^m} e^{-\frac{Q}{RT}}$$

Table 3.2:Creep parameters for Equation 3.1

Q	A'	n	m
223076.62 J/mol-K	4.841E-19	1.936	1.86

3.3.2 Fracture and Cracking

Given that U3Si2 has approximately a quarter of the rise to power fracture normally evident in UO2, this work utilizes the existing BISON UO2 relocation model reduced by a factor of 0.25. In using this approach, it is assumed that relocation is proportional to the amount of cracking present in the fuel. Standard UO2 fuel cracking and relocation in BISON is handled using the ESCORE relocation model [31] that has been linearly modified as described above to: $\Delta D = 0.2Q \left(\frac{G_o}{D_o}\right) (0.005Bu^{0.3} - 0.2D_o + 0.3)D_o$, where Bu, D_o, and G_o are the burnup, as-fabricated diameter and fuel-clad gap

respectively. Note, this model is a combined cracking and relocation model that adjusts the diametral strain of the fuel without any need for a stress state. It is essentially a non-physical strain to account for fuel relocation that is added to the total strain from all other sources in the simulation.

The above relocation model does nothing to account for actual stress redistribution in the fuel upon cracking. In most materials there exists a direct relationship between the stress distribution in a region of a material and the failure crack length of the material. For simple geometries this relationship is described by $Y = K_{Ic}/\sigma_f\sqrt{\pi a}$ where KIc is the material toughness and a is the crack length [32]. The geometrical factor Y is approximately unity where specimen size is much larger than crack length [32].

Metzger reported a U3Si2 fracture toughness of $0.930 \text{ MPa}\sqrt{m}$, however, samples of U3Si2 produced using improved arc melting strategies have shown fracture toughness in U3Si2 to be as high as $3.25 \text{MPa}\sqrt{m}$ [1] [9]. The average fracture crack length of 72um and fracture toughness taken from Mohamad results in a cracking stress of approximately 216 MPa.

Cracking of the fuel in the present simulation is based on an isotropic smeared exponential softening model already designed into the BISON codebase with a cracking stress of 216 MPa. When stress exceeds $\sigma_c = 216$ MPa in any principle direction then the model cracks the fuel reducing the stress exponentially according to $\sigma = \sigma_c(\sigma_{res} +$

$$(1 - \sigma_{res}) \exp\left(\frac{\alpha\beta}{\sigma_c}\left(\epsilon_c^{max} - \epsilon_c^{init}\right)\right)$$ where the residual stress $\sigma_{res} = 0$ and the fitting

parameters αβ are assumed to be the negative of the Young's modulus for U3Si2 [33].

3.4 SiC material Models

3.4.1 Elasticity

As was shown in Chapter 2, the elasticity of SiC is affected by irradiation to a

small degree. This effect is coupled to the irradiative swelling of SiC which saturates at

low fluence. Since the majority of swelling in SiC is accomplished very early in the life of

the fuel, the monolithic Young's modulus will simply be reduced linearly over

approximately 2 dpa by 10% to 414GPa. This way a great majority of simulated time will

use the irradiated monolithic SiC young's modulus while accounting for the early burnup

transient. Similarly, the axial unirradiated Young's modulus for composite SiC is reduced

by 18.4% to 181.71 MPa.

Though composite SiC is a highly anisotropic material, the material properties

must be implemented isotropically in BISON due to unavailability of anisotropic

plasticity tensors in BISON. Anisotropic elasticity tensors are available for composite SiC

that can be implemented without plasticity models, however, plasticity of SiC is an

important point in SiC modelling efforts and should not be neglected. Since hoop and

axial elasticity moduli are in the same range of values the results of the simulation in

this work are considered adequate, however, the need for further development to

incorporate anisotropic plasticity tensors into BISON is acknowledged.

3.4.2 Plasticity

Compliant composite SiC materials have been developed to allow SiC to behave

more like a metal under conditions where monolithic SiC would brittlely fail. CMC

materials demonstrate unique plastic-like behavior that doesn't follow the same mechanism as most ductile materials. Generally for CMCs, rather than retaining full elasticity upon unloading, when thresholds of stress are exceeded the Young's modulus is permanently damaged and the material follows a different stress-strain path upon unloading.

To simulate this behavior a damage-based plasticity model was developed. In this model, damaging of the composite SiC Young's modulus occurs whenever the CMC matrix cracks. The stress-strain relationship for multiple loading and unloading cycles is shown in Figure 3.2 below:
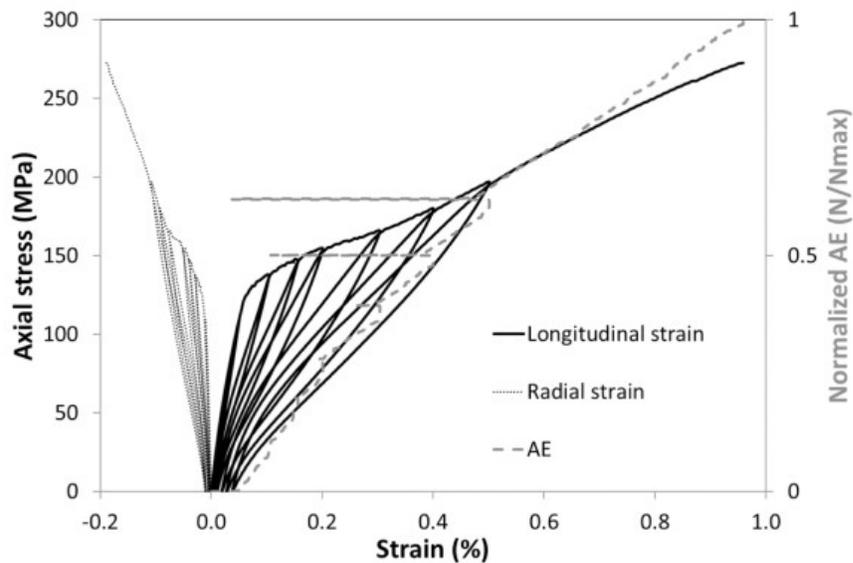
Figure 3.2: Axial stress vs strain of composite SiC [16]

As seen in the figure above, J. Braun and others have shown that composite SiC follows a cracking based damaged Young's modulus loading and unloading scheme. Since a model for this kind of behavior does not exist in the BISON codeset, it was necessary to develop a model that adjusts the Young's modulus whenever the maximum

von mises stress exceeds the previous maximum and recomputes a new modulus from

the data in Figure 3.3 adapted from Braun below:

An important assumption in the development of this cracking model is that there were

no other stresses applied to, or present, in the specimen used in Braun's experiment. In
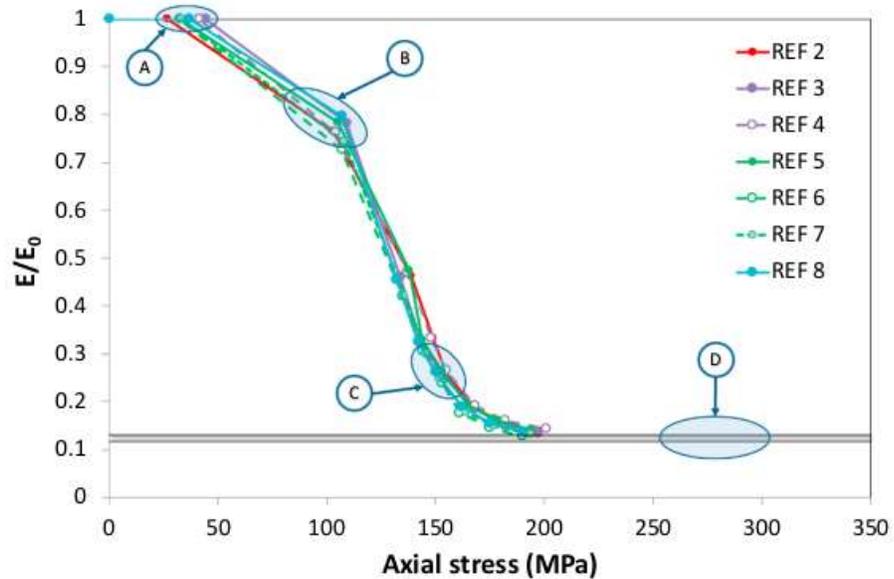
Figure 3.3: Composite SiC damage factor based on attained stress

this case, the axial stress data equal the von mises stress state.

3.4.3 Thermal conductivity

To account for the wide variety of thermal conductivities possible through

differences in composite SiC cladding microstructures, average values for unirradiated

thermal diffusivities reported by Koyanagi are used to calculate the nonirradiated

thermal conductivity [18]:

$$k_{nonirr} = \alpha \rho C_p \tag{3.2}$$

Density and heat capacity are provided from their respective coupled variables within

the BISON simulation.

Thermal resistivity, $R = k^{-1}$, is convenient for adding varying conductivities in series where $R_{tot} = R_{irr} + R_{nonirr}$. It is assumed that irradiation will damage all composite SiC structures similarly and so the thermal resistivity due to irradiation, R_{irr}, is assumed to follow the swelling coupled relations for composite SiC provided by Stone [5]:

$$R_{irr} = 15.11 \cdot S \tag{3.3}$$

Total thermal conductivity is then computed by $K_{tot} = R_{tot}^{-1}$. The total thermal conductivity for composite SiC is calculated by using the Koyanagi relation for unirradiated thermal resistivity and the Stone relation for irradiated thermal resistivity.

3.4.4 Irradiation swelling

The Katoh model swelling model identified in Chapter 2 comprises several nested temperature dependent functions that cannot be analytically integrated. Numerical integration of these relations are highly sensitive to simulation timestep size. During BISON simulation, error caused by this non-linearity prior to 1 dpa is minimized by use of sub steps within each BISON time step to calculate irradiation swelling. 100 substeps is the default for the Katoh model in the BISON codebase, however, 300 substeps are used in this work to ensure that numerical integration errors aren't propagated through the remainder of the solution.

The Katoh swelling model makes no attempt to distinguish between axial and radial swelling. Since irradiation swelling is implemented as an eigenstrain in BISON, it is believed that incorporating anisotropic swelling in future work would be possible. However, although measurable differences between axial and radial swelling have been

reported, these differences are somewhat small and come from plate specimen data which may have considerable differences from tube specimen [20]. Until such time that tube specimen data are sufficient to produce an anisotropic swelling model for composite SiC, considering the small differences involved it is enough to assume isotropic irradiation swelling in this simulation.

3.4.5 Irradiation creep

A combination of models is used to model irradiation creep in SiC. Transient swelling coupled irradiation strain rate is described by Singh in below:

$$\dot{\epsilon}_{pri} = K_{pri}\sigma\dot{\epsilon}_{vol}, \tag{3.4}$$

$$K_{pri} = 3.5626 \cdot 10^{-4}T^2 - 4.1704 \cdot 10^{-1}T + 156.8507 \tag{3.5}$$

where $\dot{\epsilon}_{vol}$ is the strain rate due to irradiation swelling. Equation 3.5 is shown here as reported in the literature [34]. The units for this equation should be MPa^{-1} based on the context of the paper, but as the exact units aren't reported there is some difficulty as the calculated irradiation creep rate is many orders of magnitude too high when the equation is used as provided.

To illustrate, composite cladding temperatures are approximately 800K based on the author's prior simulation experience. Typical mid-life burnup cladding hoop stresses are compressive at approximately 40MPa. Assuming a very small swelling rate near saturation of 0.0002s⁻¹, then:

$$\dot{\epsilon}_{irr} = 51.2 \text{ MPa}^{-1} * 40\text{MPa} * 0.0002\text{s}^{-1} = 0.41\text{s}^{-1}$$

Strain rates near 40% per second are unreasonable especially considering this would be the strain rate near where the swelling coupled creep should be nearly saturated. Clearly, K_{pri} is many orders of magnitude too high.

Earlier work by Koyanagi suggests a steady state creep coefficient of about $1 - 2 \cdot 10^{-7} (\text{MPa dpa})^{-1}$ for composite and monolithic SiC at LWR temperatures [21]. Lewinsohn's much earlier work on monolithic SiC tube specimen agrees, $3.16 \cdot 10^{-7} (\text{MPa dpa})^{-1}$, after unit conversion where $1 \ dpa$ of fluence is assumed to be 10^{25}n/m^2 for consistency with most SiC irradiation creep literature [23]. For steady irradiation creep and a typical assumed damage rate, $\phi = 10^{-6} \text{dpa/s}$, then the steady state creep rate:

$$\dot{\epsilon}_{ss} = K_{ss}\sigma\phi = 2 \cdot 10^{-7} (\text{MPa dpa})^{-1} \cdot 40\text{MPa} \cdot 10^{-6} \text{dpa s}^{-1} = 8 \cdot 10^{-1} \ \text{s}^{-1}$$

Even with admittedly rough calculations it is immediately evident that the equation for K_{pri} is perhaps 10 orders of magnitude too high. To rectify this problem, transient and irradiation creep were combined into a single model to allow comparison against data:

$$\dot{\epsilon}_{tot} = \dot{\epsilon}_{ss} + \dot{\epsilon}_{pri} = K_{ss}\sigma\phi + K_{pri}\sigma\dot{\epsilon}_{vol} \tag{3.6}$$

Equation 3.6 is used to calculate cladding creep rate. When the same calculation is done using creep coefficient data as provided by Koyanagi [21], the transient and steady irradiation creep rates are comparable when K_{pri} is adjusted by a factor of 10^{-6}. In Figure 3.4 below, a test calculation is performed to compare the creep of monolithic SiC when determined with interpolated Koyanagi data against our units adjusted creep coefficient model.
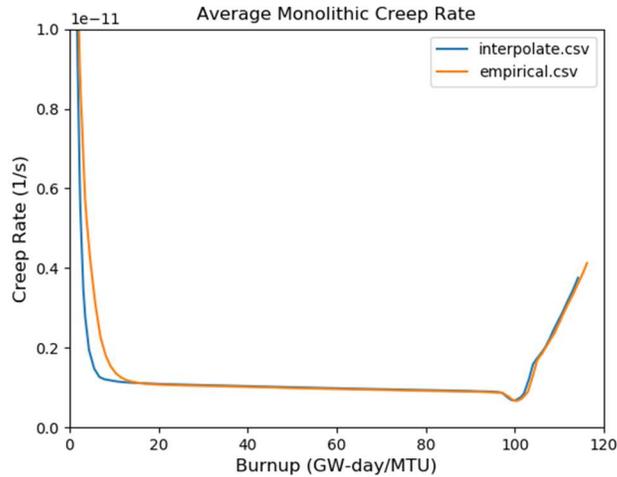
Figure 3.4: Calculation of SiC creep rate

As evidenced in Figure 3.4 all major order of magnitude differences have been resolved. The remaining differences during the swelling coupled transient region are immediately explained by the fact that the empirical model accounts for variations in the temperature dependent characteristic fluence, γ_{sc}, and swelling rate constant, k_s, that would not have been present in the data as provided by Koyanagi for the conditions simulated in this example [21]. Since k_s trends upward and γ_{sc} trends lower as temperature goes down, and the simulation temperatures are generally lower than those in the Koyanagi data, the calculated creep rate is expected to be higher and the saturation burnup shifted to the right. The adjustment factor on K_{pri} gives a result consistent with this expectation and will be used in our combined model for irradiation creep.

More recent in-reactor SiC tube specimen creep data have shown creep rates about 3.67 times higher than SiC BSR creep data show [22]. An adjustment to the irradiation creep model proposed above in Equation 3.6 is needed to account for this

difference. Since the BSR data have well documented the existence of transient and steady irradiation creep regimes, the models developed to describe this behavior are considered sound in quality but quantifiably low in their representation of actual tube specimen irradiation creep. To account for lower calculated irradiation creep, the models presented by Singh are adjusted by the above factor to bring them in line with the measured Halden BWR SiC irradiation creep data [22] [34]

3.4.6 Rod Geometry and Simulation Conditions

The finite element fuel rod mesh used in this simulation is designed to be a drop-in fit to PWR 17 x 17 fuel assemblies such as those in use at the Seabrook Station reactor [35]. Generally, the radial external design and conditions of the simulated PWR concept ATF follows those specified in Appendix K of Todreas' text. The intent of this simulation is to evaluate steady-state performance under worst case nominal core conditions. That is, the outside radius of the concept U3Si2/SiC fuel rod is 4.75mm, rod pitch is 12.6mm, coolant mass flux is $3675.4 \text{ kg m}^{-2} \text{ s}^{-1}$, coolant inlet temperature is 599.95 K and coolant pressure is 15.31MPa. To save computation time the assumed peak $\text{LHGR} = 44.62 \text{ KW m}^{-1}$ is used over a small rodlet of ten 9.8mm height pellets.

For the case of this study, the rodlet is imagined to represent the center most region of the hot-channel in a PWR design. As such, average calculated temperatures and stresses of this rodlet represent what would be expected to be the peak local temperatures and stresses at the axial centerline of a Seabrook hot channel.

3.4.6.1 LHGR Variation

Though the Seabrook Station peak LHGR is quite high, local reactivity depletion reduces the local heat generation over time. A common parameter in core analysis that

46

describes overall core neutron multiplicity is K_{inf} which accounts for neutron production

and loss factors related to core materials while neglecting geometry considerations.

Since the present simulation is designed to mimic the maximum local behavior of a fuel

rod designed with benchmark material conditions, it stands to reason that variations in

K_{inf} for a benchmark reactor would adequately describe changes to the local LHGR in this

simulation.

To account for variation in the LHGR over burnup, calculated slope of K_{inf} based

on the BEAVRS reactor benchmark shown in Figure 3.5 below is applied to the simulated

maximum LHGR over simulation time [36]. In this manner, simulated LHGR varies from

its maximum down to 24.3 kW/m over the simulated timeframe.
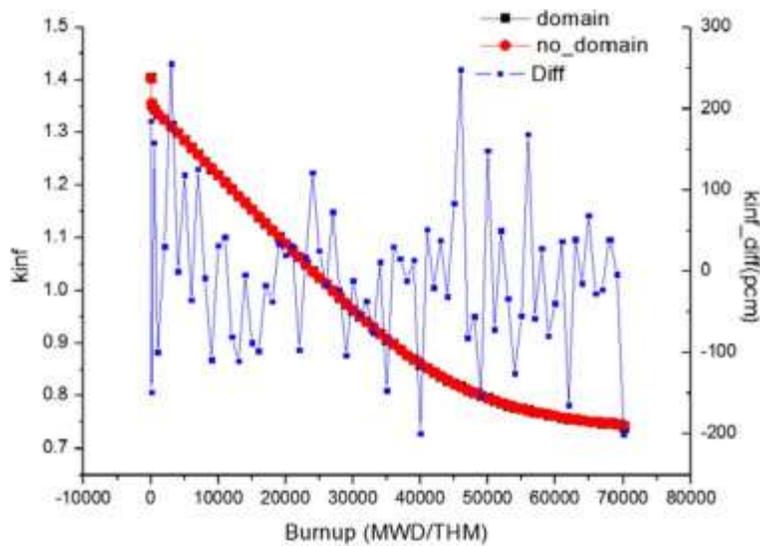
Figure 3.5: Variation in K_{inf} [36]

3.4.6.2 Plenum Volume

The coefficient of thermal expansion of U3Si2 is approximately 1.5 times greater

than UO2. However, the Seabrook standard plenum height to heated fuel height ratio of

1.059 does not require adjustment. Since the fuel is loaded at room temperature and

47

UO2 operates at higher peak operating temperatures, the expected plenum size

increase factor is:

$$\frac{\Delta L1}{\Delta L2} = \frac{a1}{a2} \cdot \frac{\Delta T1}{\Delta T2} = \frac{15}{10} \cdot \frac{900}{1400} = 0.96$$

Thus, the rod length to fuel height ratio is similar to the original design and does not

need adjustment. Total rodlet fuel plenum height is then 10.38cm from a heated fuel

height of 9.8 cm.

3.4.6.3 Cladding Thickness

Cladding thickness has a large impact on the performance of nuclear fuels due to

its deleterious effect on heat transfer, i.e. thicker claddings cause higher temperatures

and thermal expansion throughout the fuel which can reduce time to fuel clad contact.

Although the external radial fuel geometries remain unchanged from the nominal

Seabrook specifications, use of U3Si2 as fuel with duplex SiC cladding necessitates

changes to internal design. Weaving of SiC fibers in the production of composite SiC

prevents the use of nominal Seabrook cladding thicknesses of 0.572mm.

Current production CVI composite SiC structures are commonly produced with a

total thickness of about 0.75-1.1 mm [3], however, the composite SiC layer can be made

as small as 0.35mm [37]. As typical production of composite SiC materials results in

thicknesses approaching 1mm [3], such a thick cladding thickness necessarily causes a

reduction in available fuel volume.

By maintaining a 1mm SiC cladding thickness, a minimum reduction in fuel

volume of 37.7% would occur if normal fuel enrichments are to be maintained:

$$1 - \frac{V}{V_o} = 1 - \frac{\pi r^2 h}{\pi r_o^2 h_o} = 1 - \frac{r^2}{r_o^2} = 1 - \frac{3.75^2}{4.75^2} = 37.7\%$$

U3Si2 is more uranium dense than UO2 by 17%, however, despite this volumetric fuel density advantage, U3Si2 would likely need enrichment when using a 1mm cladding thickness. Nominal Seabrook fuel radius is $r_o = 4.096$ mm, if an allowable 17% reduction in fuel volume is assumed and all other considerations remain equal, a minimum fuel radius of $r = \sqrt{0.83 \cdot r_0^2} = 3.732$ mm in U3Si2 is needed to maintain equal reactivity contribution as compared to UO2. Provided total rod outer radius is maintained at 4.75 mm and an assumed fuel-clad gap of 0.08mm, then:

$$4.75 \text{mm} - 1 \text{mm} - 0.08 \text{mm} = 3.67 \text{mm}$$

Clearly, there is insufficient thickness available for a 1mm cladding thickness without enrichment.

Reliable tube CMC SiC have been produced with a combined thickness of 0.75mm [37]. It is assumed that since experimental length specimen can be reliably produced at a thickness of 0.75mm that reactor scale duplex CMC tubes of 0.8mm combined thickness are certainly possible. Hence, for this work a total cladding thickness of 0.8mm is assumed. The minimum assumed monolithic thickness is 0.2mm to provide a substantial environmental barrier and seal for the porous composite SiC. This configuration allows for enough fuel reactivity by exceeding the minimum fuel diameter while also exceeding the minimum industry production thicknesses.

Chapter 4 Results and Discussion

4.1 Thermal creep model

4.1.1 Mukherjee-Bird-Dorn

The strategies discussed in chapter 3 to produce the data in Table 3.1 are used in

the development of a thermal creep model for U3Si2. Here, a fitness comparison of

power law, coble, and Nabarro-Herring creep is conducted. Equation 3.1, can be used to

provide an empirical best fit to thermal creep data and provide an indication of the

creep mechanism. This analysis finds the creep parameters for this form to inform the

further analysis of creep mechanism candidates that are likely to have been present in

Mercado's original experiment.

Equation is linearized and produces the following creep coefficients when a best

fit linear equation is calculated against the data from Equation 3.1:
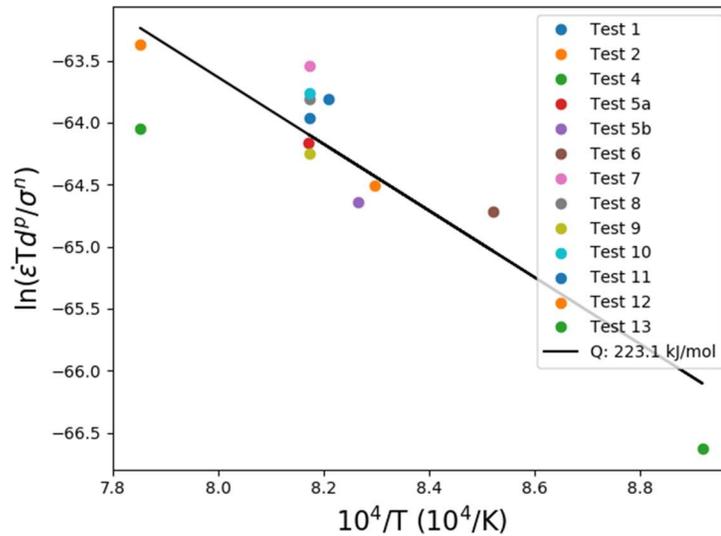
Figure 4.1: A=4.841e-19, n=1.936, m=1.86, Q=223kJ/mol-K

When these parameters are used to plot experimental data against calculated model data a high degree of correlation and statistical confidence are found.
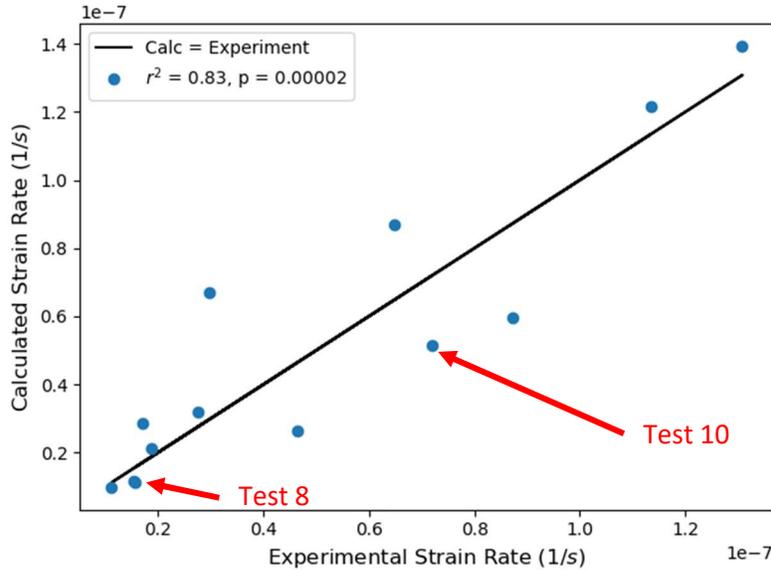
Figure 4.2: Equation 3.1 compared to data

Tests 8 and 10, previously excluded by Freeman, are shown to fit well with other Tests demonstrating the importance of statistical control of experimental data. Values of n above 1 indicate a possible power law creep mechanism. Also, m above one shows a grain size dependence that will be present for diffusional creep modes such as Coble and Nabarro-Herring creep. Since Equation 3.1 fits best with n=1.936 and m=1.86, the possibility of power law and diffusional creep modes must be considered. Creep parameters for all three of these creep models will be determined and compared to provide an indication of which creep mode dominates.

4.1.2 Power law creep

The most common model for creep is that of power law of the form:

$$\dot{\epsilon} = A\sigma^n e^{-\frac{Q}{RT}} \qquad (4.1)$$

51

This equation is linearized and plotted in the same manner as above. A best fit linear

regression to the linearized form of Equation 4.1 is used to find the values for n, Q and

A:
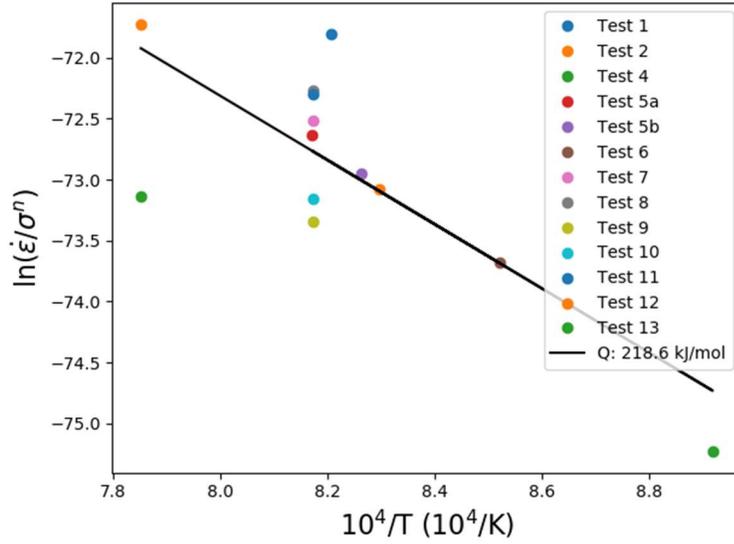
Figure 4.4: A=5.385e-23, n=3.156, Q=218582.5 J/mol-K
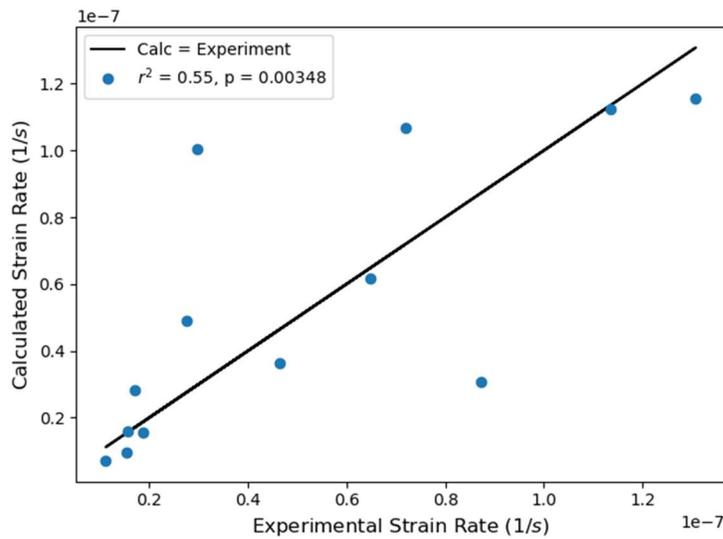
Figure 4.3: Equation 4.1 compared to data

While the preceding is a fair fit to the data in terms of correlation, the power law

creep models are clearly less statistically confident than the Mukherjee-Bird-Dorn

relationship suggests is possible although still lower than the rejection threshold. With

n>3 we have some evidence that dislocation creep does contribute to the overall creep

of U3Si2.

An improved power law creep form as shown by Dartmouth University [38] with

inverse temperature is given in Equation 4.2. When linearized and plotted against data

we have results similar to the more common form of power law creep:

$$\dot{\epsilon} = \frac{A}{T}\sigma^n e^{-\frac{Q}{RT}} \tag{4.2}$$
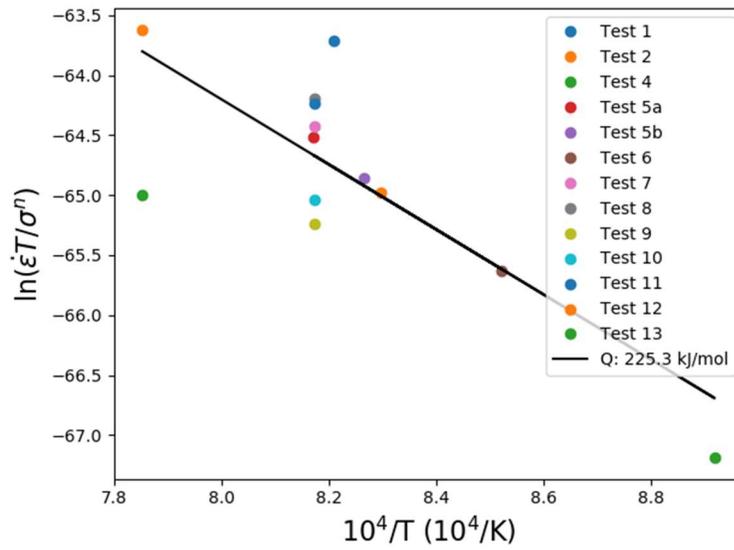
Figure 4.5: A = 3.388e-19, n = 3.1, Q = 225288.02 J/mol-K

As seen in Figure 4.6 below, power law seems to offer some evidence of contributing to

creep due to having a p-value lower than the point of significance. However, the this p-

value is much larger my more than an order of magnitude in comparison to the

empirical Mukherjee-Bird-Dorn relationship. This disparity implies that power law is

missing an important part of creep in U_3Si_2 and the majority of creep contribution must

be found in another mechanism.
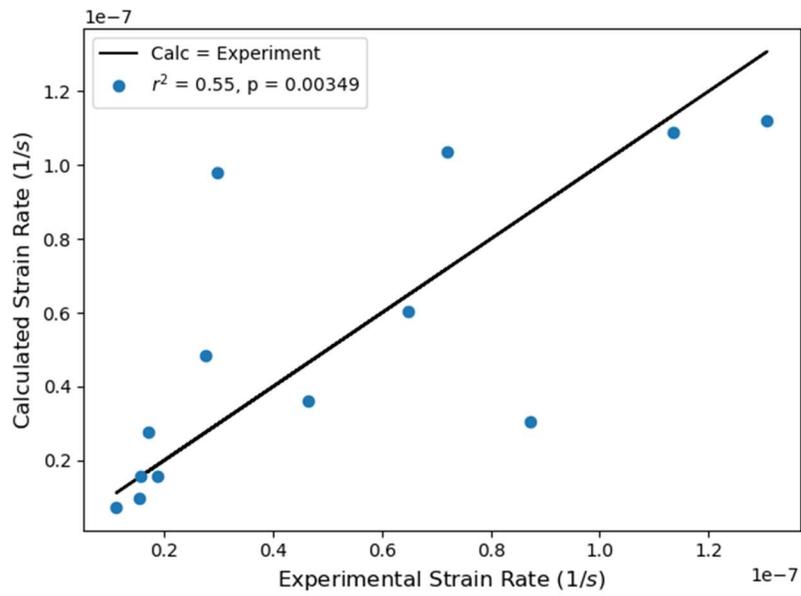
Figure 4.6:Equation 4.2 compared to data

4.1.3 "Cu$_3$Au" Rule

The possibility of U3Si2 following power law creep mechanism similar to other

intermetallics, i.e the Cu$_3$Au rule, is also investigated with n=5:
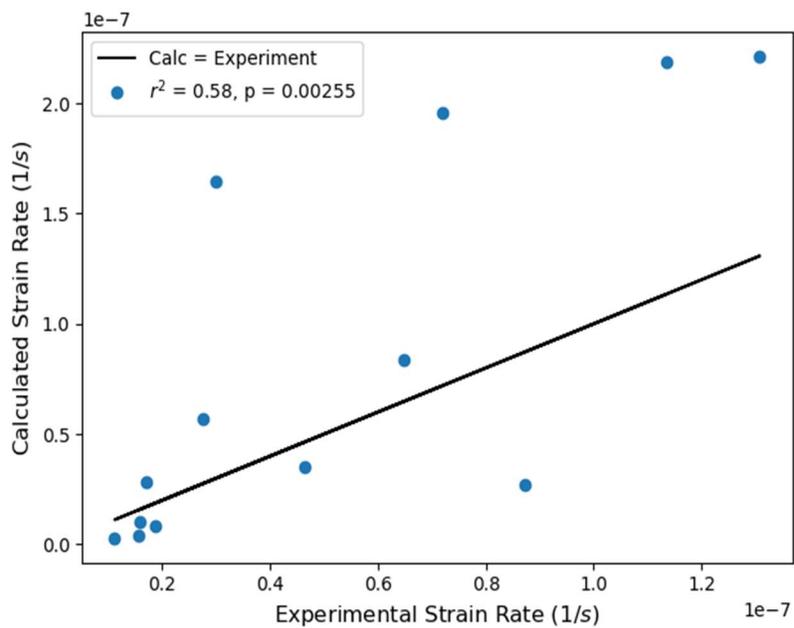
Figure 4.7: Power Law with n=5 compared to data

Figure 4.8 provides an indication that power law creep that follows the Cu_3Au rule may exist in certain tests. There appears to be a clear trend where some tests agree with the Cu_3Au rule and others do not. The lower of the two groups contains a mixture of U3Si2 pellets, and strain conditions that do not produce a trend. However, the highest four points that do not fit the Cu_3Au rule are the four highest stress states tested (Tests 2,4,5a, and 10. This result, and the indication from Equation 3.1 of the presence of both power law and diffusion creep mechanisms, is evidence of multiple creep modes evidencing from Mercado's experiment.
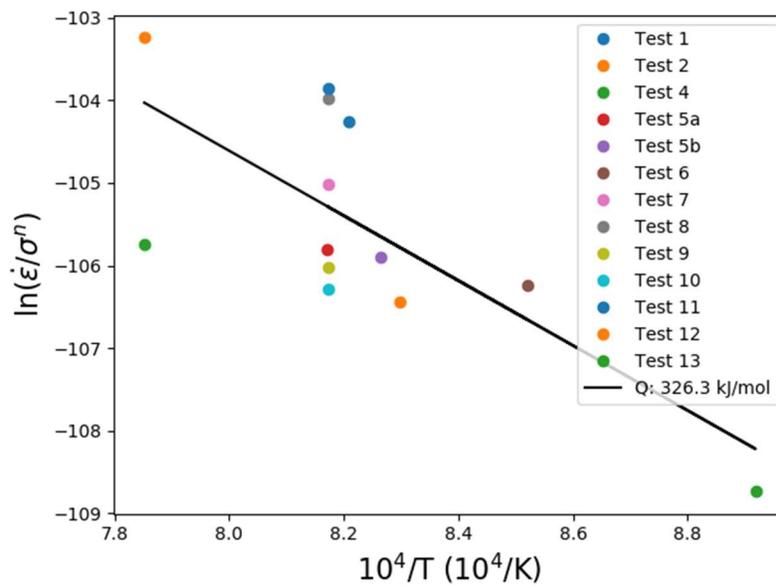
Figure 4.8: A = 1.596e-32, Q = 326304.34 J/mol-K

4.1.4 Coble Creep

The equation for Coble creep is linearized and plotted in the same manner as done above. Equation 4.3 is used to produce Figures 4.9 and 4.10:

$$\dot{\epsilon} = \frac{A\sigma}{Td^3}\ e^{-\frac{Q}{RT}} \qquad\qquad 4.3$$

Coble creep provides a better correlation as well as statistical likelihood of matching the data as compared to power law. Empirically speaking, the only difference between the Dartmouth power law relationship and diffusion models such as Coble and Nabarro-Herring is the grain size dependence. From this we can posit that grain size
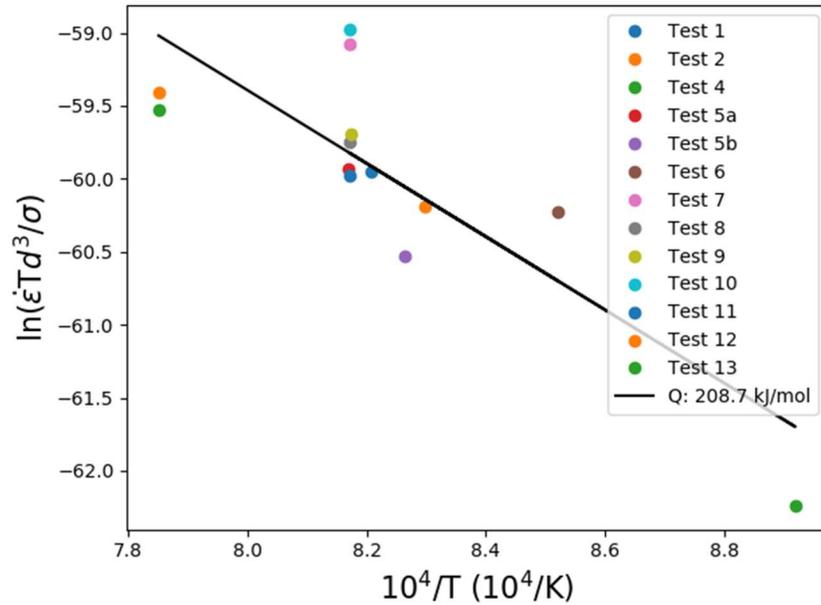
Figure 4.9: A = 8.492e-18, Q = 208729.42 J/mol-K
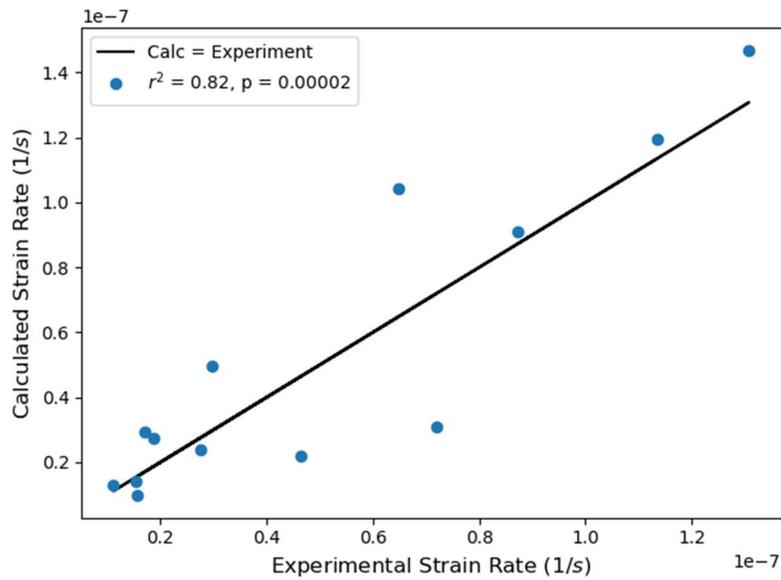
Figure 4.10: Equation 4.3 compared to data

dependence is important to the mechanism of creep in the majority of creep tests, i.e

diffusion modes of creep are the largest contributors to the creep rate of U3Si2 during

Mercado's experiment.

4.1.5 Nabarro-Herring

Though the only empirical difference between Coble and Nabarro-Herring creep

is the order of the grain size exponent, they are physically different in that NH creep

occurs at higher temperatures and involves the diffusion of atoms through the grains as

opposed to diffusion around grain boundaries in the case of Coble creep. Because of this

closely related diffusion behavior, NH and Coble creep are often competing mechanisms

with NH dominating at higher temperatures [38].

The creep coefficients for NH creep are expected to provide a similar result as

Coble but are included here for completeness:
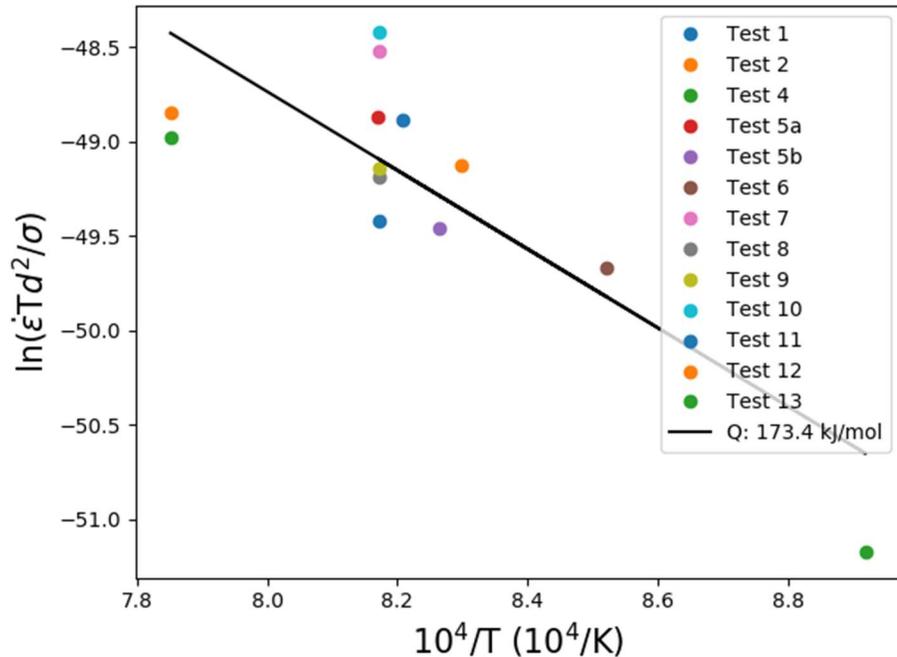
Figure 4.11:A = 1.201e-14, Q = 173358.92 J/mol-K
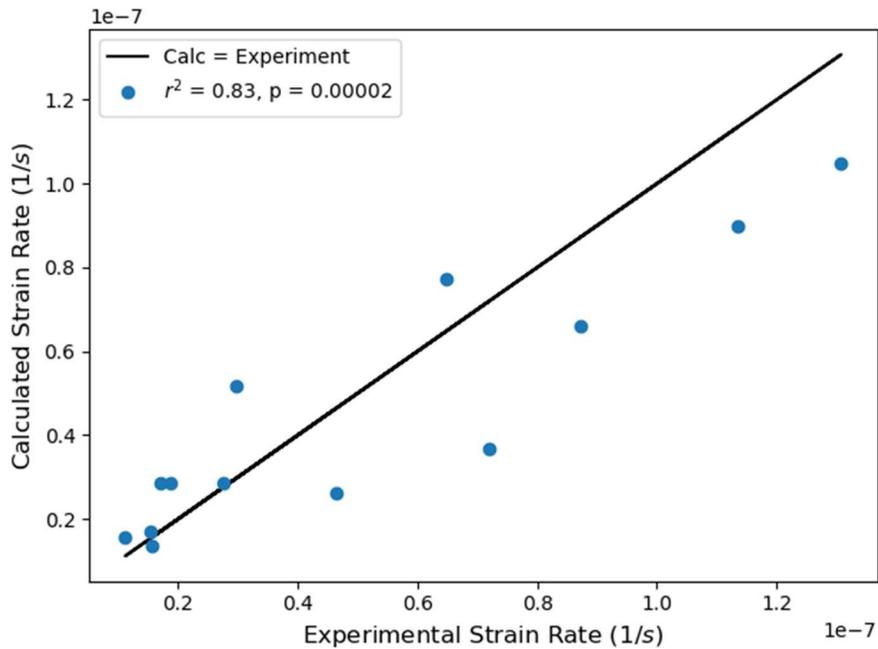
Figure 4.12:Coble creep compared to data

Two important differences exist between the Coble and NH results. First, one may observe visually by comparing Figures 4.10 and 4.12 that while both Coble and NH provide a very good fit to the data, the NH plot in Figure 4.12 show the model calculated creep rates track nearly in parallel to the experimental data whereas the Coble plot in Figure 4.10 do not show such an ideal trend. Second, the calculated activation energy between these two modes of diffusion creep are different, 209 kJ/mol and 173 kJ/mol for Coble and NH respectively.

Interestingly, the self-diffusion coefficients for uranium and silicon are 204 kJ/mol and 171 kJ/mol respectively [39]. Considering the relative amounts of uranium to silicon in U3Si2 this provides a weighted average self-diffusion coefficient of 190.8 kJ/mol which is very comparable to the calculated diffusion activation energies found in this work. Given the strong statistical improvement when using diffusional creep models

58

combined with the calculated activation energies corresponding very well with the self-diffusion activation energy, the author is of the opinion that Nabarro-Herring creep was the predominant creep mechanism found in Mercado's 2018 experiment.

4.1.6 Analysis of Creep Results

The reader is advised that while this work has come to a specific conclusion as to the dominant creep mode found in U3Si2 for the conditions of Mercado's experiment, the reality of the observed statistical agreement between all creep modes suggests that power law, Coble, and Nabarro-Herring creep each contributed in varying quantities to the overall creep rate. It is likely that variations in the experimental conditions between creep tests resulted in different primary modes of creep between tests.

For example, high stresses above 70 MPa were applied to Tests 2 and 4 which have smaller initial average grain size than Tests 6-13. Additionally, the average applied stress in Tests 6-13 is much lower than Tests 1-5. It is possible the higher average stress state during Tests 1-5 in addition to the smaller grain diameter Petch effect resulted in the observed considerably higher overall strains in Tests 1-5. The generally much higher amount of creep strain observed in earlier tests is some evidence that another creep mechanism was in effect for those tests that was not present in later tests. Unfortunately, isolating the early tests from the later tests removes all grain size differences from the regression and makes differentiation between power law and diffusional creep modes impossible.

The above results were calculated with the archival U3Si2 grain sizes for uncrept U3Si2 samples determined by Coleman Terrapin at the University of South Carolina. His

ongoing work on post creep U3Si2 samples has shown considerable grain size growth over the course of the creep tests despite experimental temperatures laying far below the recrystallization temperature of U3Si2. One avenue of explanation is a possible low-temperature grain growth mechanism due to high stress as described by Sharon and Boyce [40].Low-temperature grain growth may also contribute to the grain size disparity observed in U_3Si_2 samples prepared by INL using apparently identical techniques as the pre-sintering compacting pressure was not tightly controlled [41].

4.1.7 Suggested Continued Study

Further study on U3Si2 pellets with improved phase purity is recommended. In particular, the possibility of low temperature grain growth during apparently diffusion dominated thermal creep of U3Si2 is especially compelling. Certainly, the diffusional creep model developed in this work can benefit by the inclusion of greater grain size resolution along the different stages of the creep tests. Additionally, improvements in grain size resolution throughout the creep test data will allow for further differentiation between Coble and Nabarro-Herring creep. Inclusion of higher stress testing conditions would elaborate on the existence of any transition to power law creep at higher stresses.

4.1.8 BISON Creep Model

Though Nabarro-Herring creep appears to be the dominant creep mechanism, the model used in the BISON simulation results below will use the Mukherjee-Bird-Dorn relationship. Since the creep analysis of this work show contributions to overall creep from power law and diffusional creep, and in consideration of the strong empirical fit provided by Equation 3.1, the Mukherjee-Bird-Dorn model is used in BISON simulation

to retain some power law related behavior in addition to the diffusional creep

characteristics. In this manner the different creep regimes evident in experiment are

carried over to simulation.

4.2 BISON Simulation

4.2.1 UO2 vs U3Si2

The physical models developed in Chapter 3 are implemented here in simulation

to provide the reader with a direct comparative view of the steady-state performance

differences between UO2-Zry and U3Si2-SiC nuclear fuel systems. The parameters used

for this comparison follow those discussed in Chapter 3 and shown in Table 4.1 below.

Maximum fuel temperatures and cladding hoop stresses are compared since they are of

greatest importance in cylindrical geometries.

Table 4.1: Simulation conditions for U_3Si_2 vs UO_2 comparison

Linear Heat Rate	26.8 to 14.6 kW/m
Plenum Pressure	2 MPa
Coolant Pressure	15.31 MPa
Coolant Inlet Temperature	599.95 K
Coolant Flow Rate	3675.4 kg/(m^2-sec)
Rodlet Pitch	12.6 mm
Rodlet Radius	4.75 mm
Fuel to Cladding Gap	80 μm

For the comparison against UO2, standard thermal oxide material properties

from the BISON code set were used. Specifically, the material properties and geometry

provided in the 2D axisymmetric tensor mechanics examples were used after making

the appropriate modifications to have the same initial conditions as developed for the U3Si2-SiC. External geometry in the two simulations is identical.

Two differences between the U3Si2 and UO2 BISON cases that are expected to have minimal impact in the context of much more important differences, i.e different fuel and cladding materials, are (1) the UO2 model uses 10 discrete pellets for a total height of 11.86 cm and (2) UO2 simulation does not include a stress cracking model for the fuel. These two differences are expected to add little error considering the more global differences of material selection and overall cladding thickness. Lack of stress cracking in UO2 is not a source of error so long as the fuel stresses are not directly compared.

Initial attempts to produce solutions of these two simulations revealed difficulty in finite element solution convergence in the UO2 simulation due to the very high initial power history. The high initial LHGR caused UO_2 max temperatures to exceed 1700 K which led to excessive thermal expansion and very early contact prior to 8 GW-day/MTU. Since this power history makes finding a finite elements solution with BISON impossible, the power history function was scaled down to 60% of its nominal value to allow the solution to converge. The resulting range of LHGR values is 26.8 kW/m at BOL to 14.6 kW/m at EOL. This range of LHGR values are only used for the comparison between UO2-Zry and U3Si2-SiC fuel concepts. All other parameters as developed in Chapter 3 remain the same.

4.2.1.1 Fuel Temperature

Fuel temperature values are gathered by finding the maximum, average, and

minimum fuel temperature anywhere in the fuel portion of the mesh during each

timestep and outputting these values to a .csv file upon successful convergence. Figures

4.13-15 below show the maximum and minimum temperatures in the UO2 and U3Si2

fuel respectively.
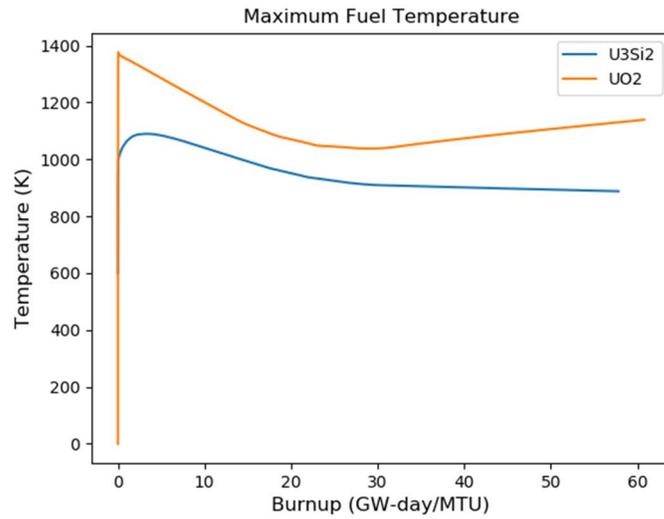
Figure 4.13: UO2 vs U3Si2, maximum fuel temperature
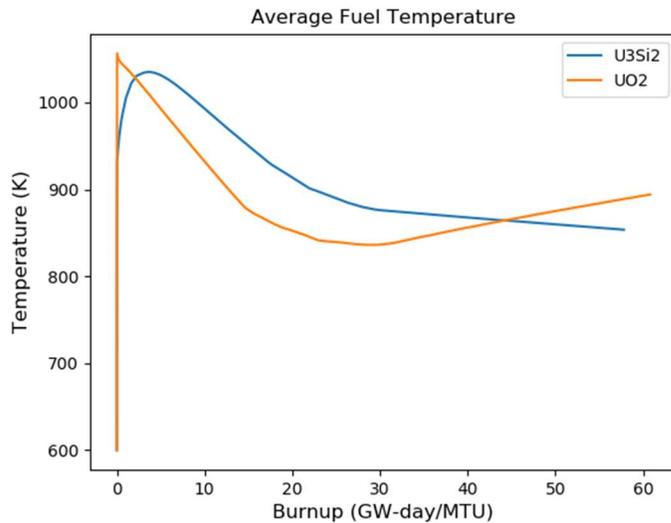
Figure 4.14: UO2 vs U3Si2, average fuel temperature
comparison
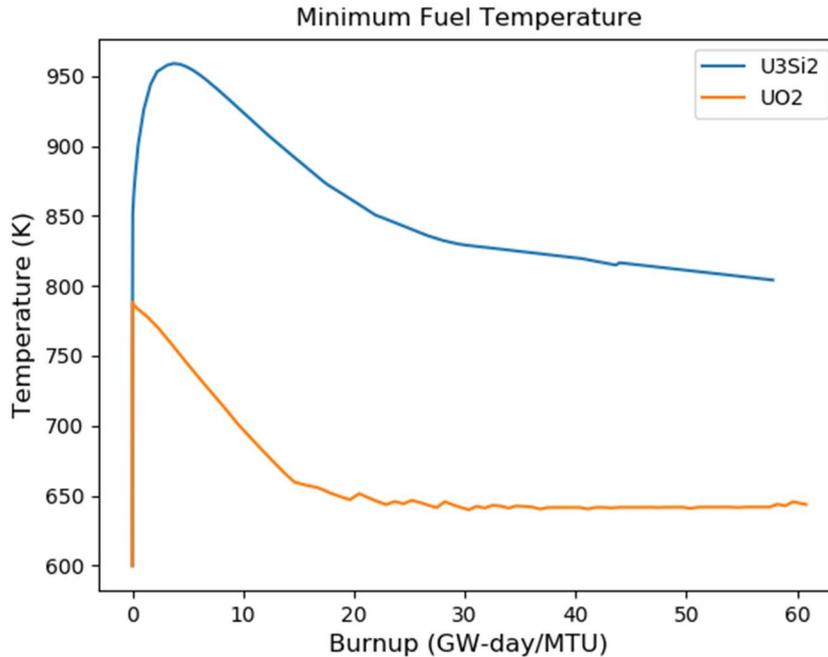
Figure 4.15: UO2 vs U3Si2, minimum fuel temperature comparison

Interestingly, the thermal conductivity advantage of U3Si2 isn't as significant as expected with only a 100-200K advantage to U_3Si_2. As evident by Figure 4.15, the minimum fuel temperature rapidly increases due to irradiative degradation of the SiC thermal conductivity. Since the heatflux from these two fuel concepts is identical we can see that the thermal conductivity advantage of U_3Si_2 is almost completely offset by the thermal conductivity disadvantage of SiC. This leads to marginally lower maximum temperatures but significantly higher minimum fuel temperatures when compared to UO2. For steady state operation this implies a marginal fuel performance advantage to U3Si2 since lower maximum temperatures make it capable of being operated at higher power densities. Ultimately however, fuel power densities are determined by each fuel's margin to melt and not their absolute operating temperature.

4.2.1.2 Homologous Temperature

Since the melting points of U3Si2 and UO2 are quite disparate, the operating

homologous temperature provides an indication of margin to melt in the fuel. Figure

4.16 below shows the homologous temperature calculated from the maximum fuel

temperature data above.
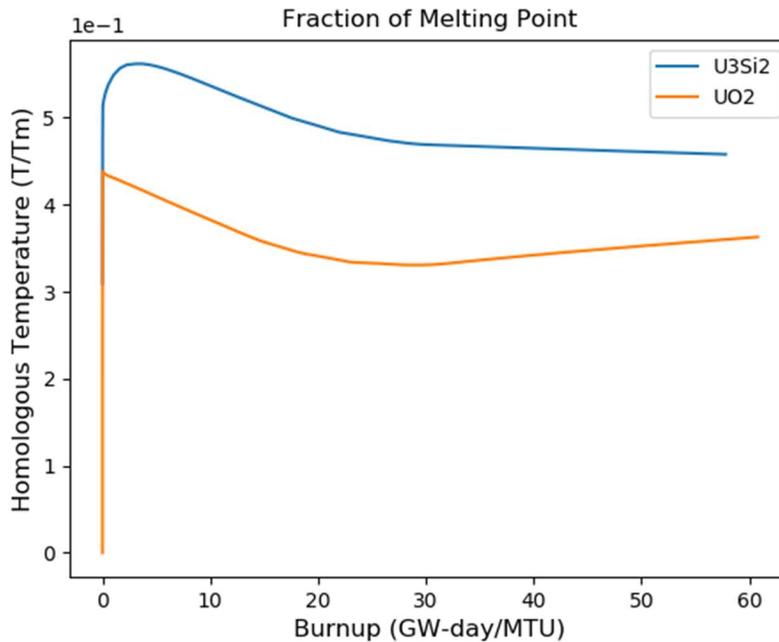
Figure 4.16: Homologous temperature comparison

A major concern for use of U3Si2 as a nuclear fuel is its relatively low melting

point. Due to this, a LOCA or RIA condition would have greater potential to cause the

fuel to melt. Adding to this concern is U3Si2's relatively low heat capacity which in the

event of a reactor casualty could cause rapid escalation of peak U3Si2 fuel

temperatures. As evident in Figure 4.16 above, the steady state operating homologous

temperature of U3Si2 is higher than that of UO2 generally by less than 0.1. Apparently,

steady state margin to melt in U3Si2 is no issue.

More interesting is the margin to melt under accident conditions. The modeling of LOCA and RIA conditions are very different than the present simulation due to the physics being in generally different regimes under which the current simulation's models break down. However, the trend in homologous temperature when operating at higher power densities can certainly be used to demonstrate each fuel's performance under more extreme conditions.

Figure 4.17 below shows the homologous temperature when power history is increased to 80% of the nominal value established in Chapter 3:
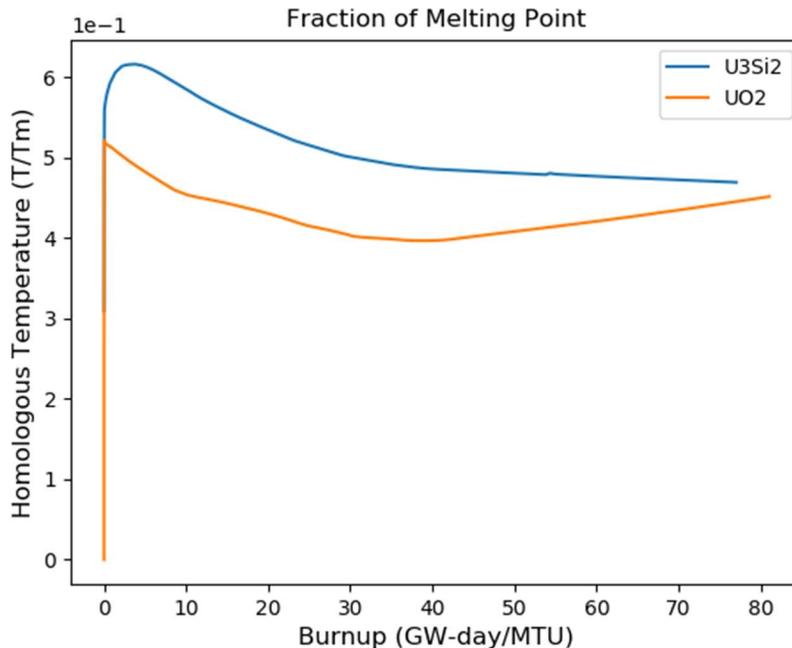
Figure 4.17: Homologous temperature at higher LHGR

Although the conditions here are not representative of a true RIA, the above illustrates that at higher steady-state conditions the difference in margin to melt between UO_2 and U_3Si_2 becomes smaller. This behavior indicates the performance advantage of U_3Si_2 under progressively more extreme conditions. Until more fully

developed reactor casualty scenarios are simulated which demonstrate U_3Si_2

performance under RIA and LOCA, it seems that there is little reason to use U_3Si_2 as a

reactor fuel for its marginal temperature performance improvements at steady state.

4.2.1.3 Plenum Volume and Pressure

The amount of available volume in the cladding plenum for thermal expansion of

the fuel and release of gaseous fission products impacts fuel performance by balancing

the amount of fuel available in the fuel rod against the need to allow space for

expansion and safe retention of released gaseous fission products. Generally, more fuel

in the same amount of available space results in higher possible fuel power densities at

the cost of much higher pressure due to insufficient volume for gases and thermal

expansion.
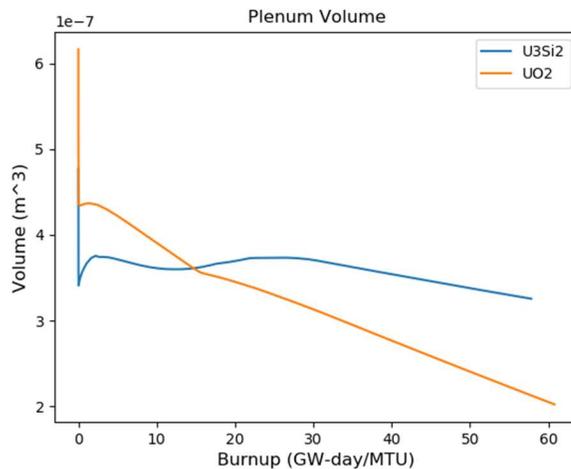
Figure 4.18: Plenum volume comparison

As previously discussed, due to slight design differences between the U3Si2 and

UO2 finite element meshes, a small difference in the initial cladding plenum volume

exists between the two simulated cases. Here in Figure 4.18 above, the UO2 simulation

is given the advantage of greater plenum volume. Despite the plenum volume

advantage for UO2, its lower thermal conductivity causes significantly more thermal expansion than is the case for U3Si2 despite having a lower coefficient of thermal expansion. As seen in Figure 4.20, this difference in pressure cannot be accounted for by gaseous fission product release which only occurs in UO_2 after about 60 GW-day/MTU.
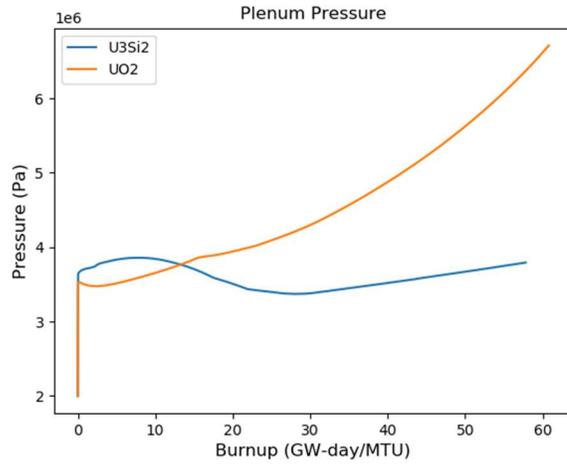
Figure 4.19: Plenum pressure comparison
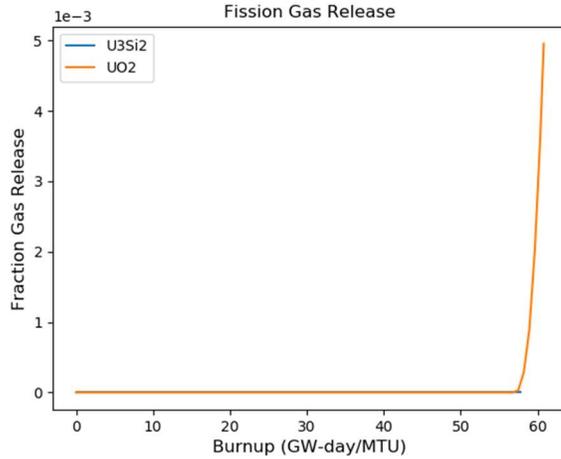
Figure 4.20:Fission gas release comparison

Though the simulations did not progress far enough to observe significant fission gas release in either case, it is notable that for UO2 onset of FGR appears earlier than in the U3Si2 case. This appears to be consistent with the INL post-irradiation examination

of U3Si2 that also found nearly zero FGR relative to what would be expected for similar

burnup UO2.

4.2.1.4 Cladding Hoop Stress

Hoop stress is an important measure for predicting cladding failure. Since the SiC

cladding is composed of two layers, these maximum, average, and minimum data were

generated for both layers combined.
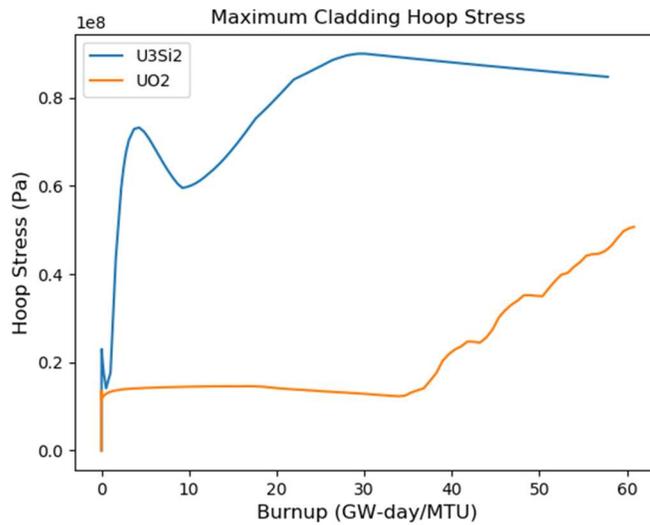
Figure 4.21: Maximum cladding hoop stress
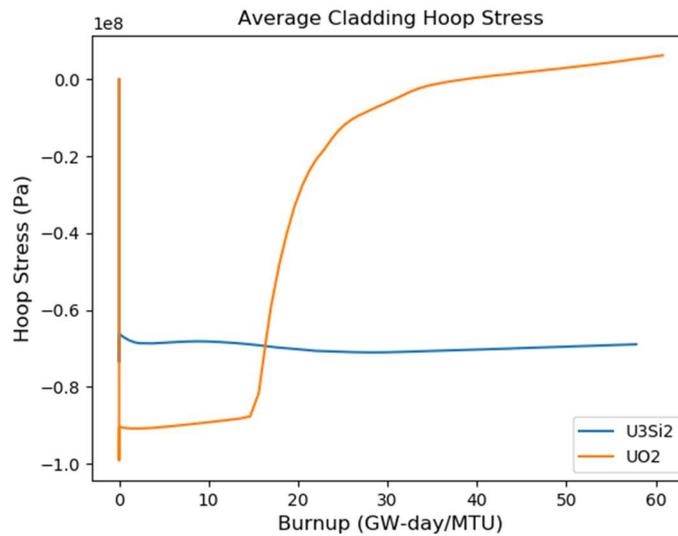
Figure 4.22:Average cladding hoop stress
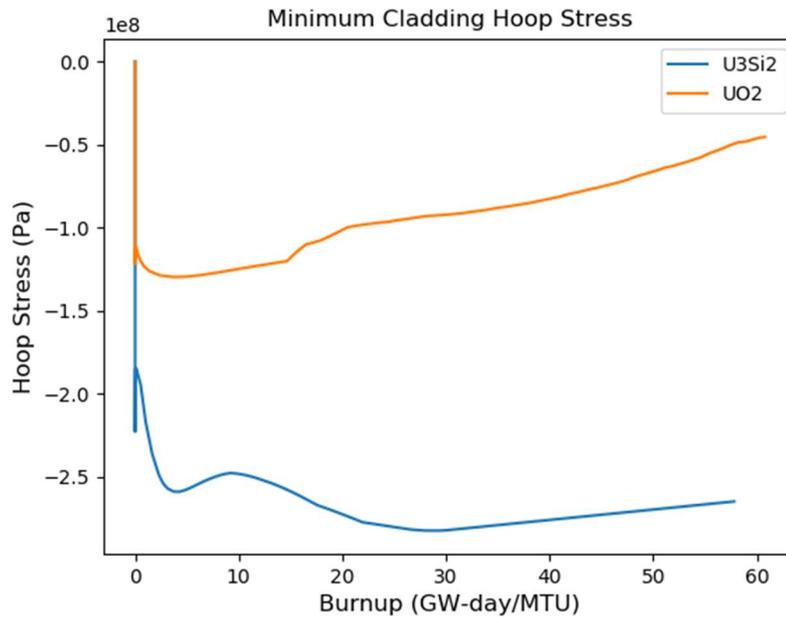
Figure 4.23: Minimum cladding hoop stress

A major result from this simulation is the large difference in operating time to

fuel-cladding contact. In Figure 4.22 it is apparent that while the UO_2 simulation

experiences contact after only about 15 GW-day/MTU, the U_3Si_2 simulation never

experiences contact. What is not clear from the above is which portions of the SiC

cladding are expected to remain in compressive or tensile stress. Although the average

stress is compressive, the difference between maximum and minimum stresses through

the SiC cladding is stark.

Clearly, Zircaloy and SiC cladding are completely different materials and respond

in drastically different manners. SiC is highly brittle when compared with Zircaloy. Thus,

the difference between maximum and minimum stresses within SiC is expected to be

higher than those seen in Zircaloy. Figure 4.24 below elucidates the stress distribution

through the cladding. In this figure, Paraview was used to visualize a small vertical

section of the cladding near the axial centerline during the middle timestep.
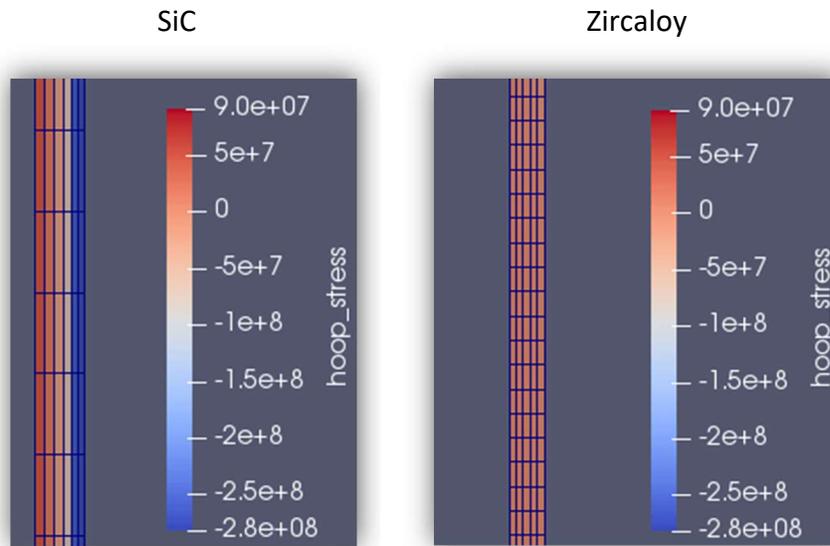
Figure 4.24: Stress distribution between SiC and Zircaloy claddings

This perspective allows us to observe that while Zircaloy tends to evenly distribute its

loading, the duplex SiC cladding has a clear bisection in its loading scheme. Generally,

the composite SiC carries the tensile loading from the fuel and the monolithic SiC carries

the compressive load from the pressurized coolant.

Large gradients of stress through a relatively thin material are concerning.

However, this behavior is important for successful implementation of CVI SiC claddings.

Since the inmost porous composite layer will microcrack under stress, integrity of the

monolithic layer is critical to maintain hermiticity of the cladding. So long as the

monolithic layer remains intact, high stress loading of the composite SiC is a favorable

condition. Hoop stress failure for monolithic cladding is modeled using two parameter

Weibull CDF statistics. The shape factor for this CDF is 3.82 with a characteristic failure

stress of 172.93MPa [42]. Satisfyingly, no failure of the monolithic cladding is predicted.

This result is expected since the monolithic portion of the cladding is maintained under compressive stress throughout the simulated timeframe.
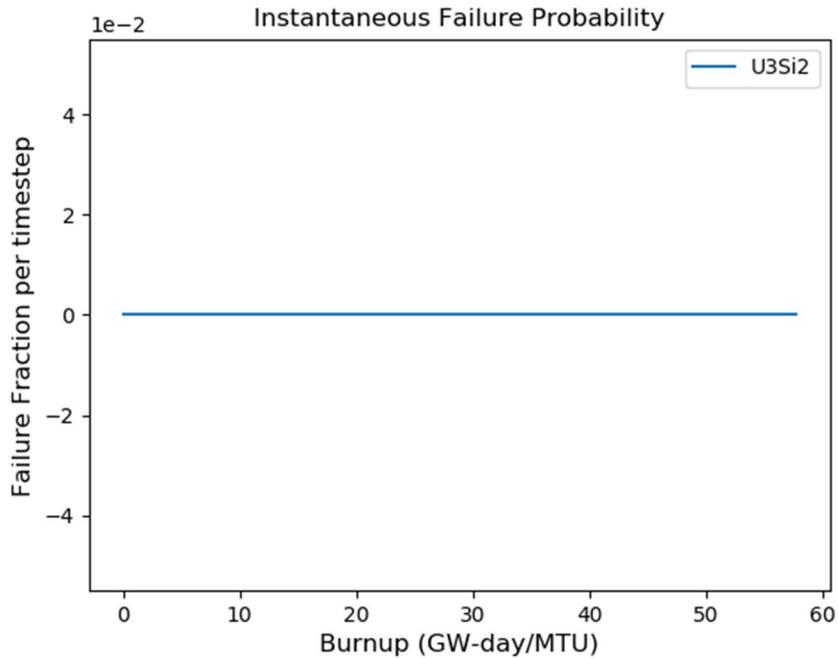
Figure 4.25:Weibull failure probability of the monolithic SiC layer

From the above results it is apparent that the U3Si2-SiC fuel concept would be an acceptable replacement for UO2-Zry fuels during steady state conditions. It is important to recognize that the current understanding of U3Si2-SiC fuel material properties continues to be developed, and that very high burnup post-irradiation examinations of U3Si2-SiC fuels are necessary to validate the predictions of this study. To guide the design of such studies, the present simulations are studied in terms of their sensitivity to various parameters to elaborate which of the incorporated models have the largest impact on simulated results and how variations in these models inform research priorities and engineering design targets.

4.2.2 U3Si2 Thermal Creep Sensitivity

Using the Mukherjee-Bird-Dorn thermal creep model developed earlier in this chapter, average hoop stress and strain in fuel and monolithic cladding are reported here for 1x, 5x, and 10x the nominal creep rate. The modified power history used earlier in this chapter was returned to its original amount as described in Chapter 3. Table 4.2 below indicates the conditions used for the various sensitivity studies:

Table 4.2: Simulation conditions used for U_3Si_2 sensitivity studies

Linear Heat Rate	44.62 to 24.3 kW/m
Plenum Pressure	2 MPa
Coolant Pressure	15.31 MPa
Coolant Inlet Temperature	599.95 K
Coolant Flow Rate	3675.4 kg/(m^2-sec)
Rodlet Pitch	12.6 mm
Rodlet Radius	4.75 mm
Fuel to Cladding Gap	80 μm
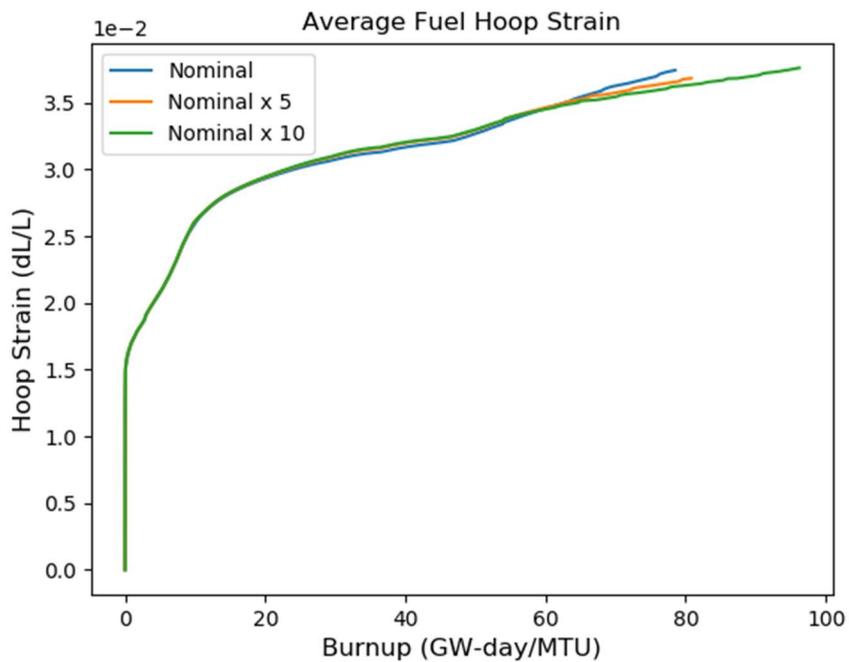
Figure 4.26: Fuel hoop strain vs U_3Si_2 thermal creep rate
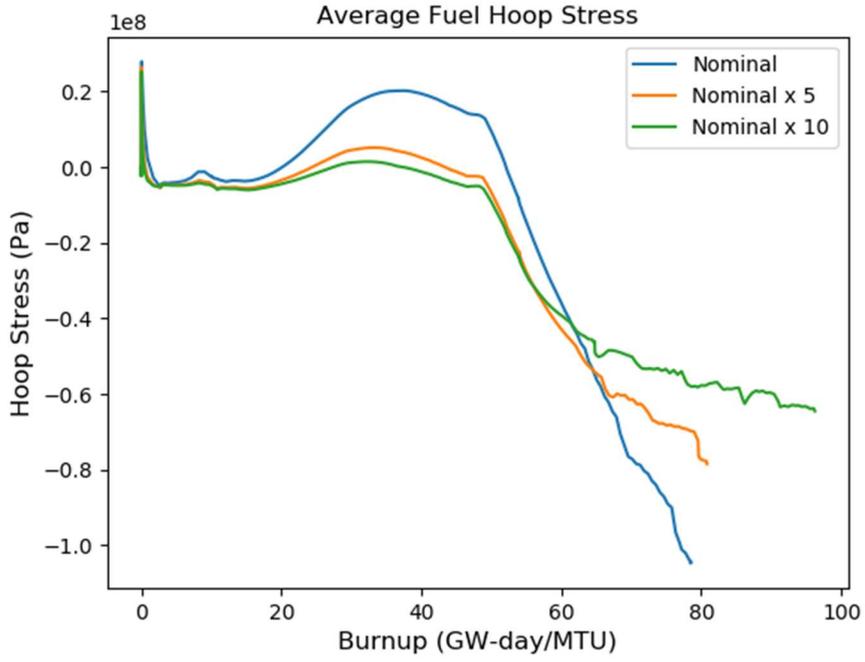
Figure 4.27: Fuel hoop stress sensitivity to U_3Si_2 creep rate
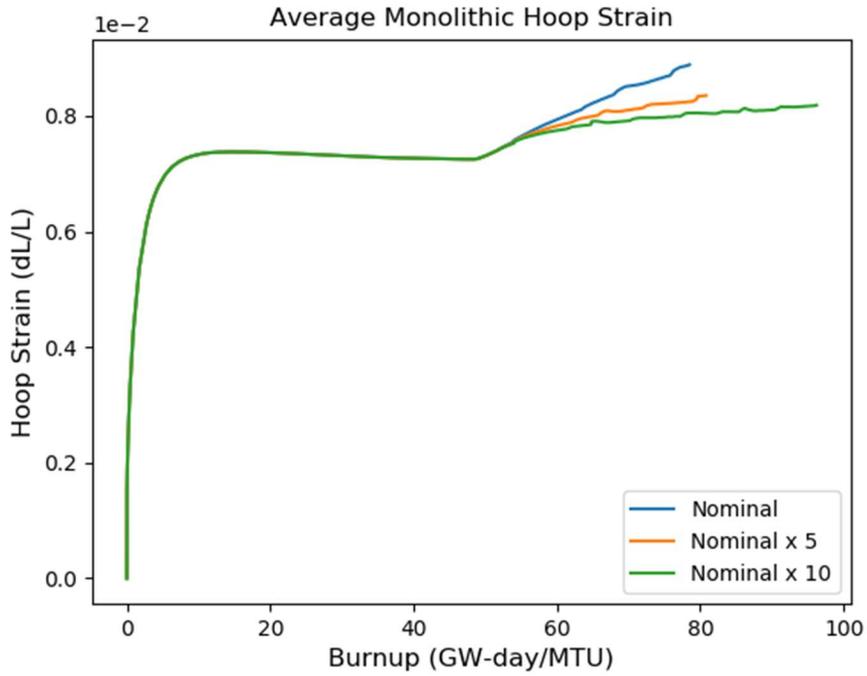
Figure 4.28: Cladding hoop strain sensitivity to creep rate
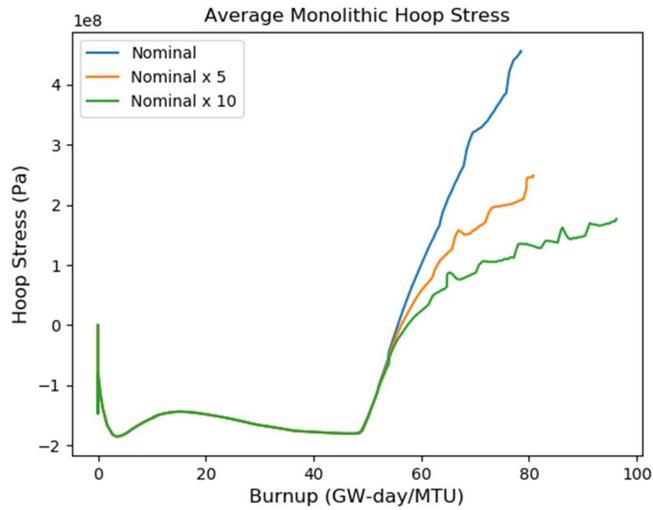
Figure 4.29: Cladding hoop stress sensitivity
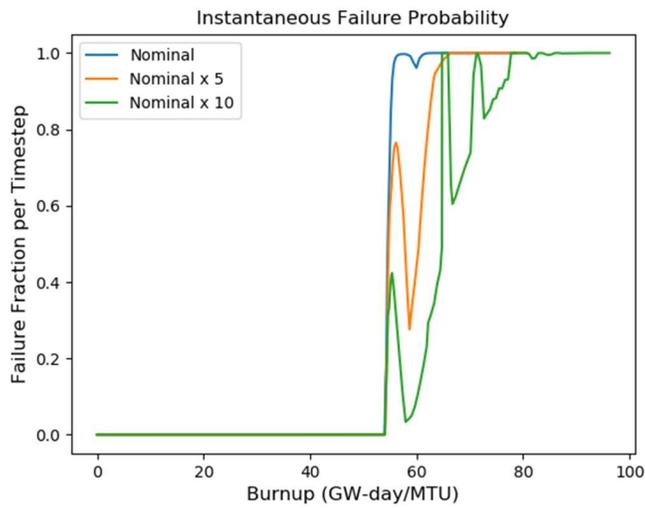
Figure 4.30: Cladding vs U_3Si_2 thermal creep rate

Of immediate interest from Figures 4.26-4.30 is the improvement in monolithic

hoop stress after contact in the cases of improved U3Si2 compliance. Notably the much

lower hoop stress is due to the higher secondary creep rate of U3Si2. Also, a large

improvement to the failure probability is evident. Instead of a nearly instantaneous

jump from zero failure to guaranteed failure, the progression between the two cases is

more gradual. The reader is advised that the seemingly unpredictable jumps seen in

Figure 4.30 are due to the large timesteps necessary in the simulation that can

sometimes result in very large variations in stress and strain within a single timestep.

This effect is particularly pronounced when the effect of the composite SiC Young's

modulus microcracking damage model is incorporated with large time steps and stress

states. Real cracking events would be expected to occur in a more progressive manner.

4.2.3 U3Si2 Densification

As previously discussed, U3Si2 shows very little change in porosity over

approximately 20 GW-day/MTU. For this reason, the comparison against UO2 did not

include any densification of U3Si2, a considerable disadvantage. However, since a U3Si2

production technique with consistent average grain size and porosity seems to be

unavailable, future burnup studies in full-scale U3Si2 rods may yet show burnup like

UO2 as was previously expected. Figures 4.31-4.33 below show how inclusion of

densification in U3Si2 affects the simulation:
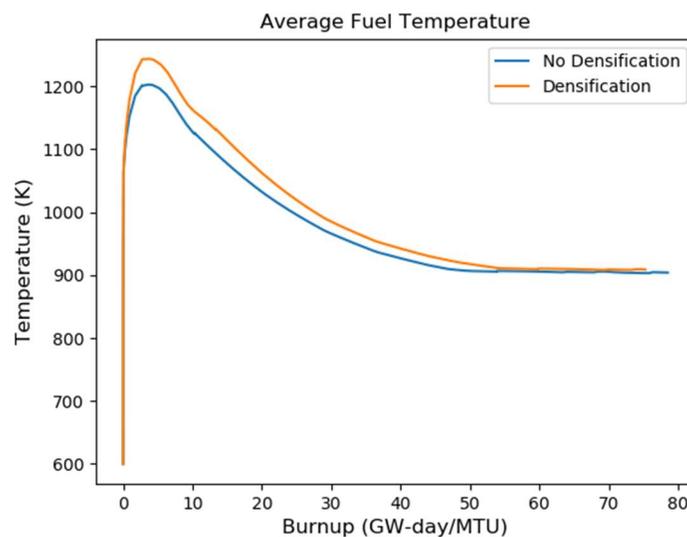
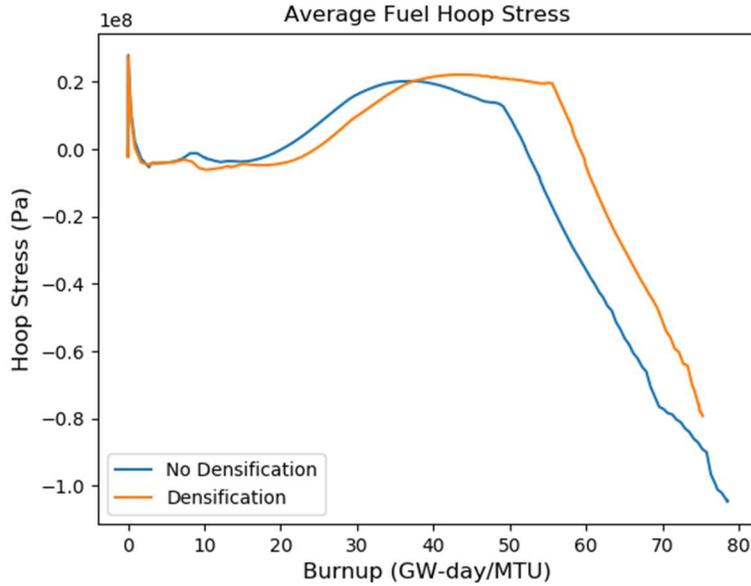Figure 4.31: Densification sensitivity on fuel temperature

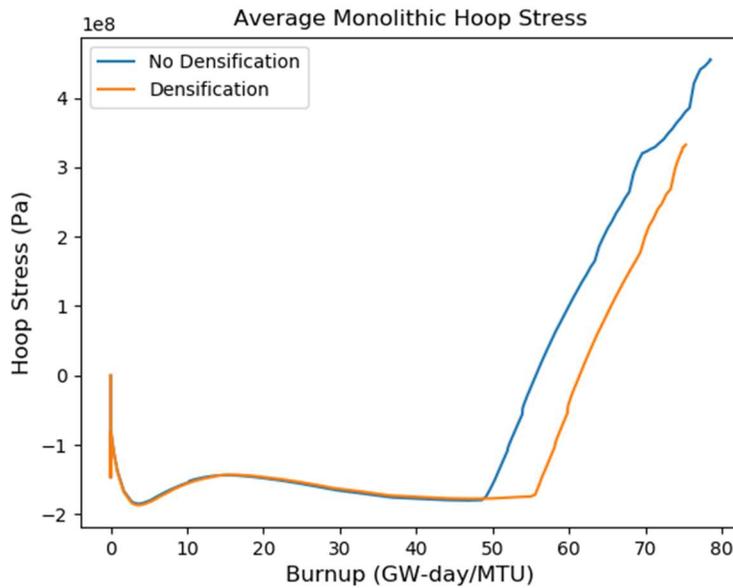Figure 4.33: Densification sensitivity on fuel hoop stress

Figure 4.32: Densification sensitivity on cladding hoop stress

Clearly, lack of densification is responsible for a loss of nearly 8 GW-day/MTU in

pre-contact operating time. On the other hand, densification causes average fuel

temperatures to be about 60K higher due to loss of heat transfer capability through a

wider cladding gap. These higher temperatures imply only slightly worse performance

for accident scenarios, while the amount of improved time to contact implies

significantly improved steady-state fuel performance. Notably, the increase in average

fuel temperature diminishes early in fuel life. Overall, the benefit to contact time

appears to outweigh the marginal increase in fuel temperature. Given the rapid failure

of the cladding upon contact, high burnup studies are needed to quantify the amount of

densification that occurs in U_3Si_2.

4.2.4 SiC Thermal Conductivity Sensitivity

Obviously, improving the thermal conductivity of the cladding is beneficial for all

nuclear fuels. However, manufacturers can only increase or decrease the nominal

thermal conductivity of a material by a certain amount. Figures 4.34-4.35 show U3Si2-

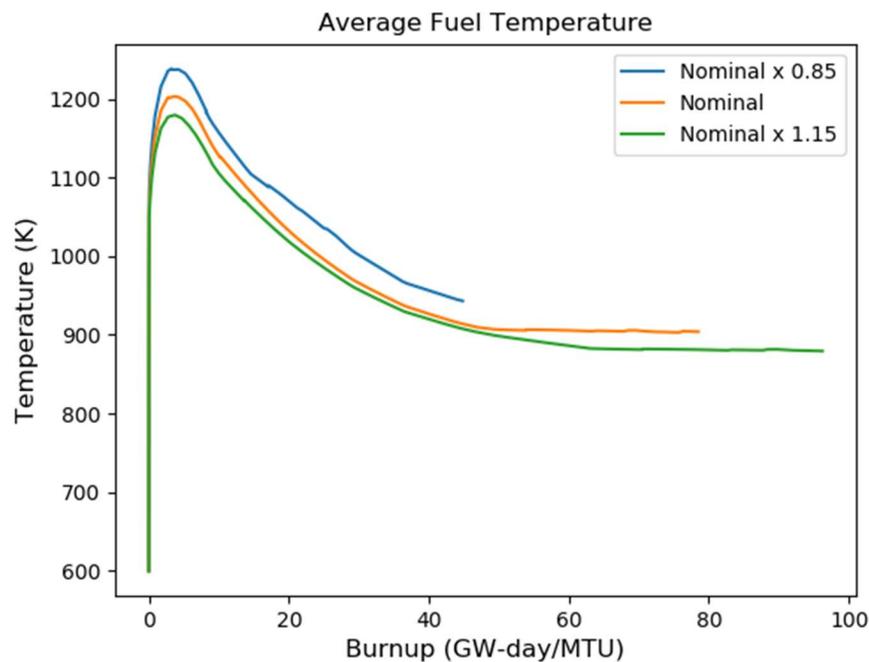SiC fuel performance when the thermal conductivity is increased and decreased by 15%:

Figure 4.34: Cladding thermal conductivity sensitivity on fuel
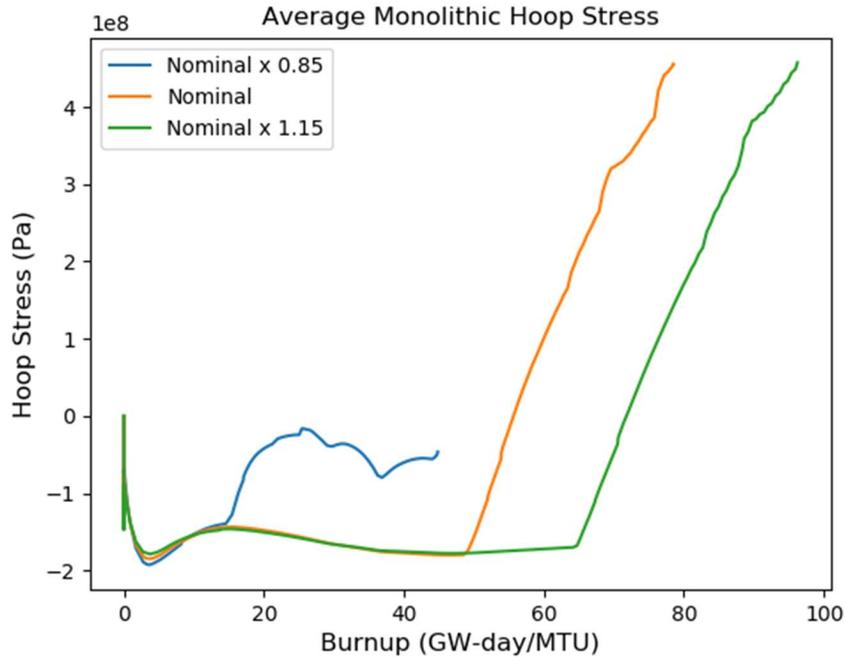temperature

Figure 4.35: Cladding thermal conductivity sensitivity on cladding hoop stress

Figure 4.35 above shows that for a 15% increase in nominal SiC thermal conductivity there is an associated 12-15 GW-day/MTU difference in available burnup prior to contact. Due to the thickness of the current production duplex SiC tubes, and the complex fuel clad interactions at the 0.85 nominal level, manufacturers do not have much room to allow thermal conductivities much lower than those provided by Koyanagi and used in this work [18].

4.2.5 No SiC Irradiation Creep

The majority of computational SiC studies assume that irradiation creep can be neglected in their simulations. To quantify the available difference in the present simulation, a case was run with irradiation creep set to zero:
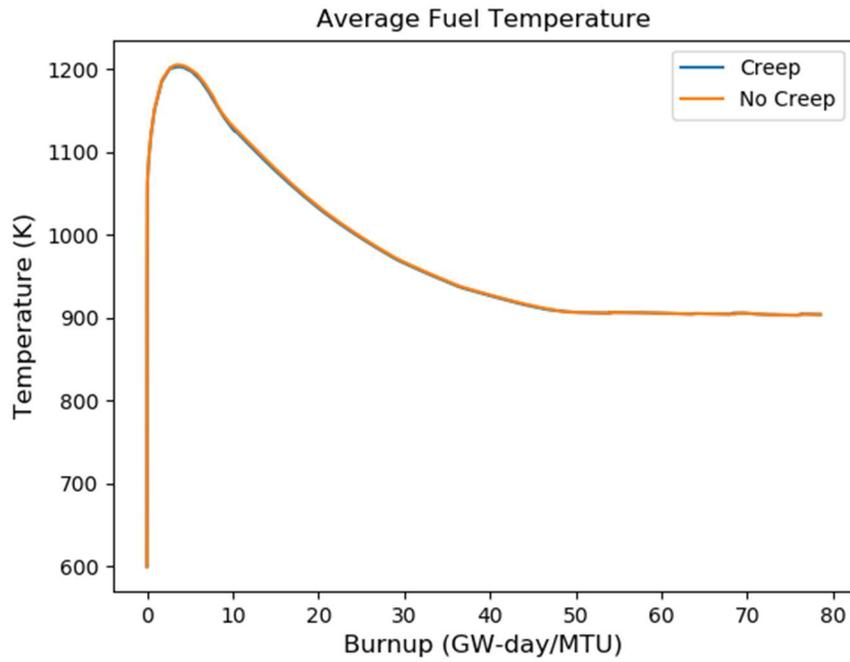
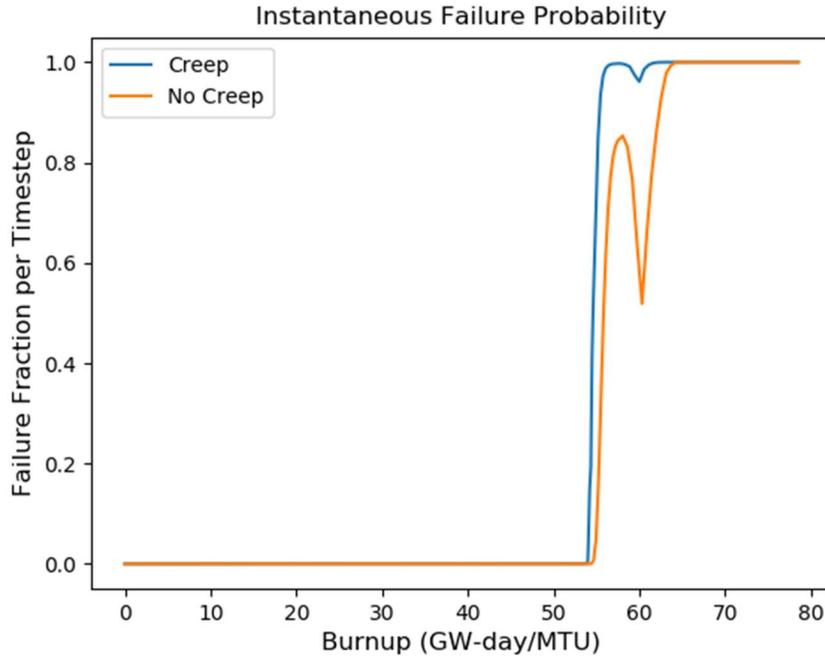Figure 4.37: Cladding irradiation creep sensitivity on fuel temperature

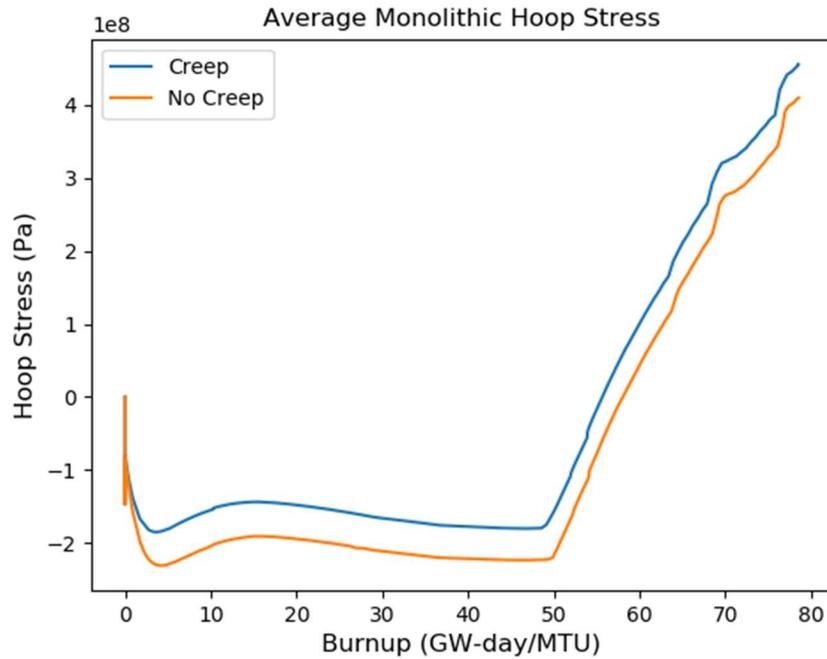Figure 4.36: Cladding irradiation creep sensitivity on cladding hoop stress

Figure 4.38: Cladding irradiation creep sensitivity on cladding failure probability

The literature's conclusions are verified in that there is minimal difference to fuel thermal-mechanical performance and time to contact. However, it is important to note that the inclusion of irradiation creep results in less compressive stress in the cladding. Additionally, Figure 4.38 shows that cladding failure profile is more sharp when irradiation creep is included. Thus, it is the opinion of the author that in the case of cladding failure studies it is important to consider the effect of irradiative creep on the monolithic and composite cladding.

4.2.6 Cladding Thickness Sensitivity

Composite SiC was shown in Chapter 2 to have a large amount of thickness variation based on fabrication technique. It is clear that a thinner cladding will improve the heat transfer characteristics of the fuel, a generally desirable characteristic, but

variations in cladding thickness will have secondary effects from the change in

temperature profile throughout the rod. Therefore, the sensitivity of composite cladding

thickness on the temperature, stress, and strain of the concept fuel is investigated.

Figures 4.39-4.43 below show how the fuel performs under various composite SiC

thicknesses. Monolithic thickness remains the same at 200 microns to preserve its

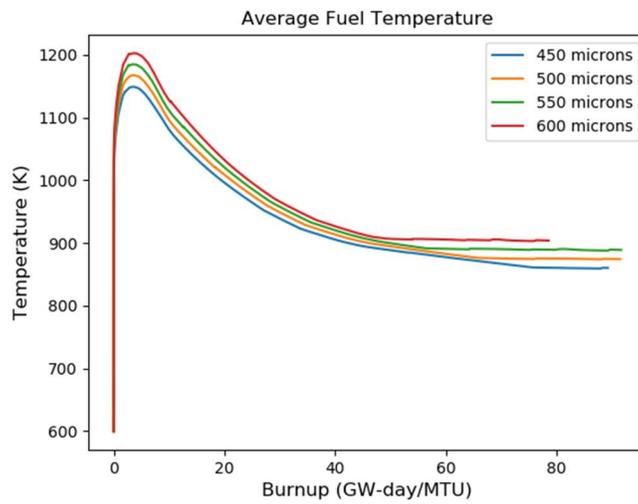performance as an environmental barrier and maintain rod hermeticity:

Figure 4.40:Composite layer thickness sensitivity
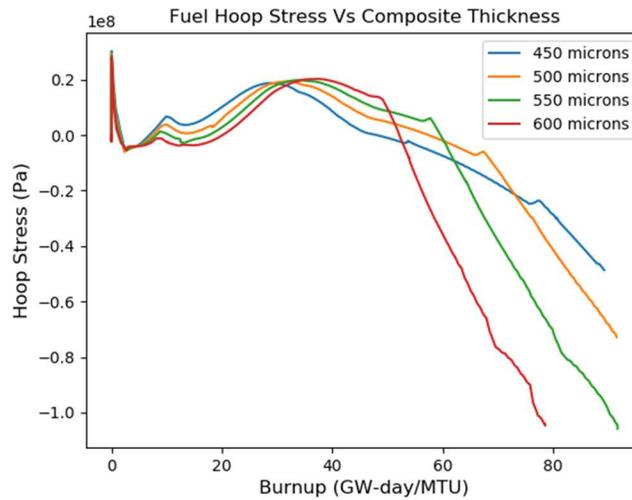on fuel temperature

Figure 4.39: Composite layer thickness
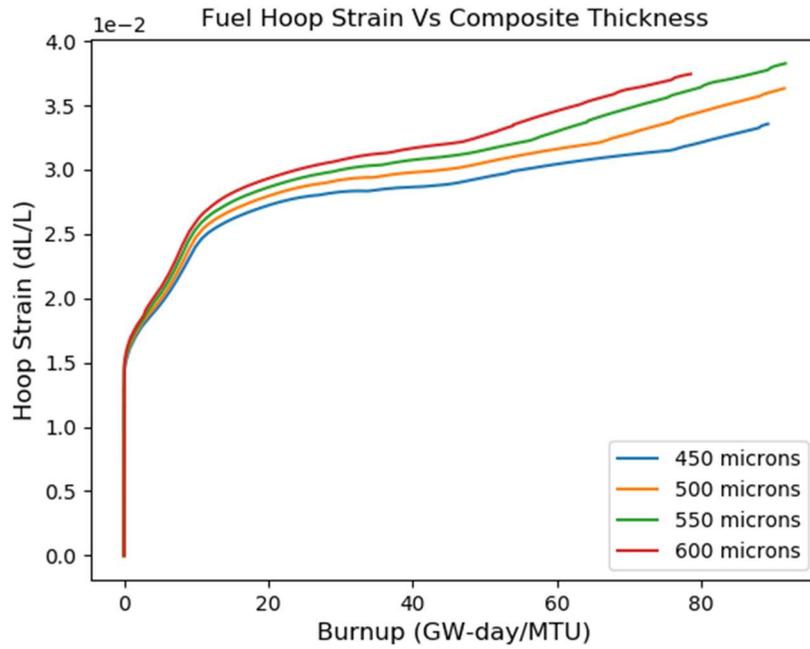sensitivity on fuel hoop stress

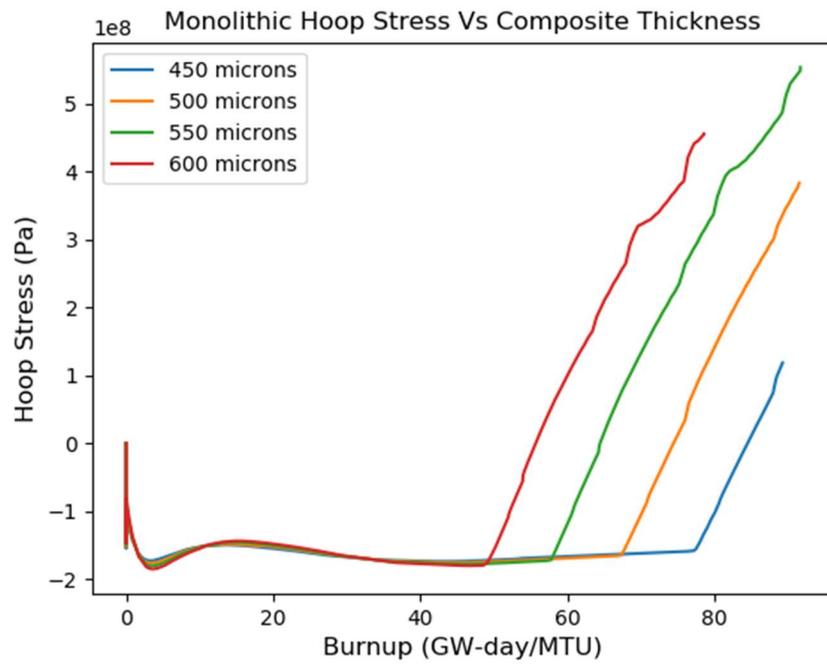Figure 4.41: Composite layer thickness sensitivity on fuel hoop strain

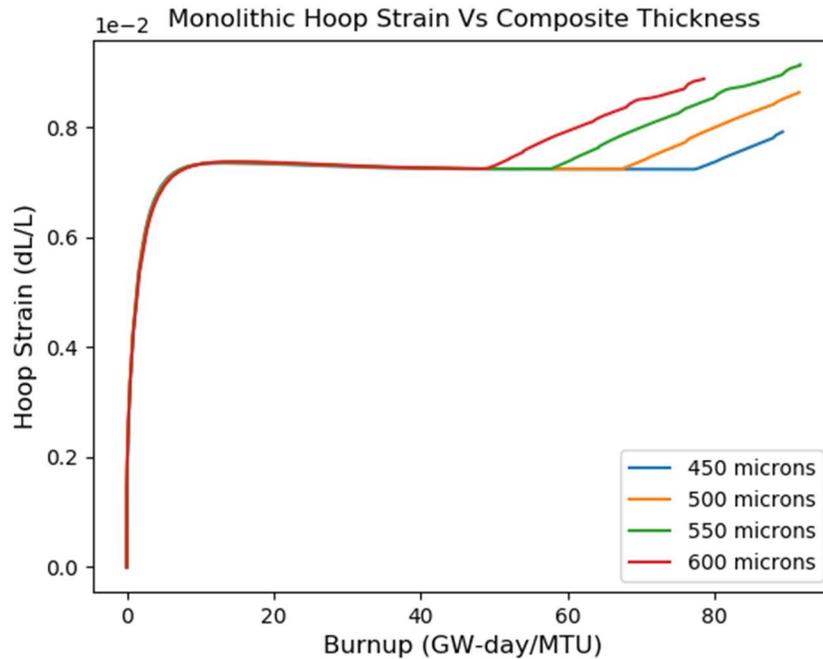Figure 4.42: Composite layer thickness sensitivity on cladding hoop stress

Figure 4.43: Composite layer thickness sensitivity on cladding hoop strain

Figure 4.42-4.43 shows post-contact performance seems to be unaffected by composite cladding thickness down to 450 microns. Given the very large improvement in time to contact and average fuel temperatures, however, cladding manufacturers should seek to reduce the thickness of composite CVI SiC claddings. Importantly, these results had the same cladding gap of 80 microns. Due to the high amount of thermal expansion in U3Si2, significant gains in operating burnup are achievable through reducing fuel temperatures with thinner cladding.

4.2.7 Cladding Gap Sensitivity

Freeman previously identified 80 microns as the ideal cladding thickness under the conditions of his original simulation [6]. However, given the sharp increase in cladding failure probability during contact, a larger cladding gap may be justified. To evaluate whether updated material properties have had any effect on the ideal cladding

gap, Figures 4.44-4.49 below show a comparison between cladding gaps of 60, 80, 90
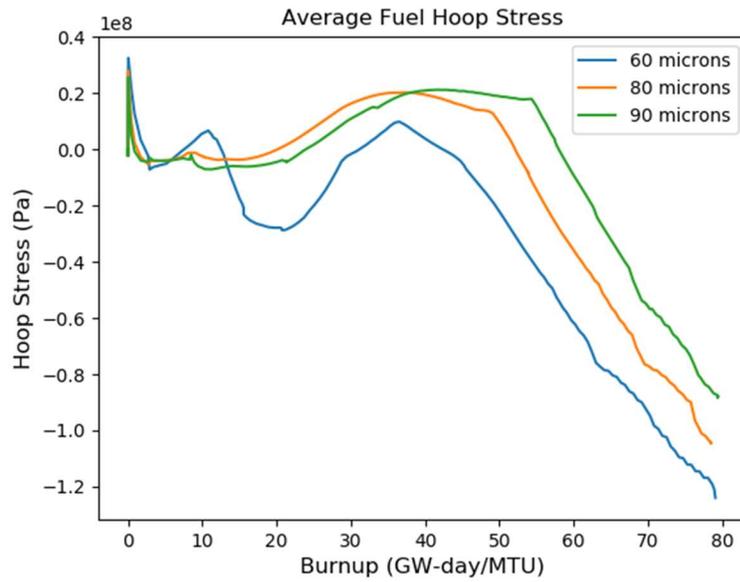
microns:

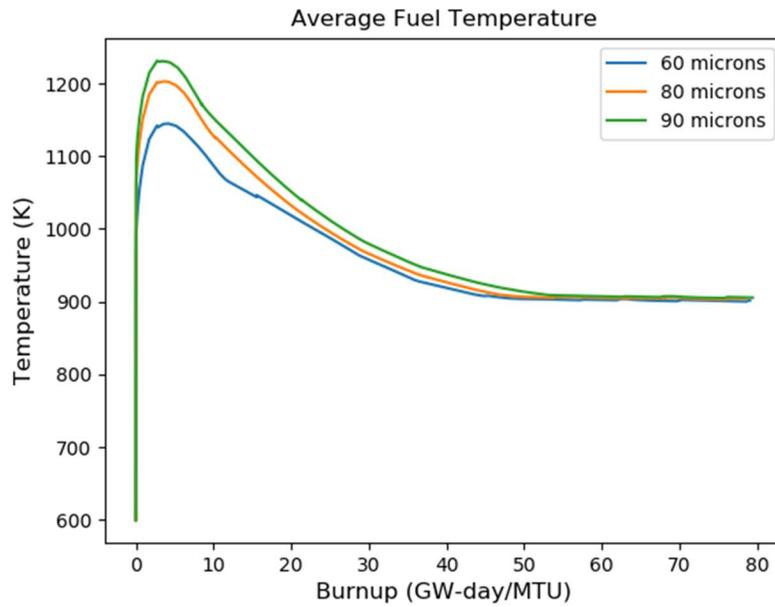Figure 4.44: Cladding gap sensitivity on fuel hoop stress

Figure 4.45: Cladding gap sensitivity on fuel temperature
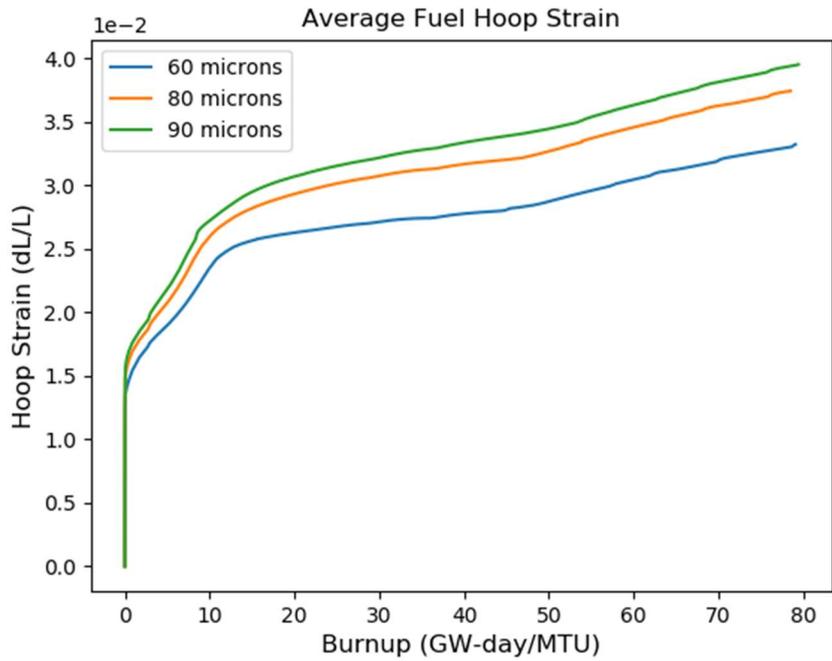
Figure 4.46: Cladding gap sensitivity on fuel hoop strain
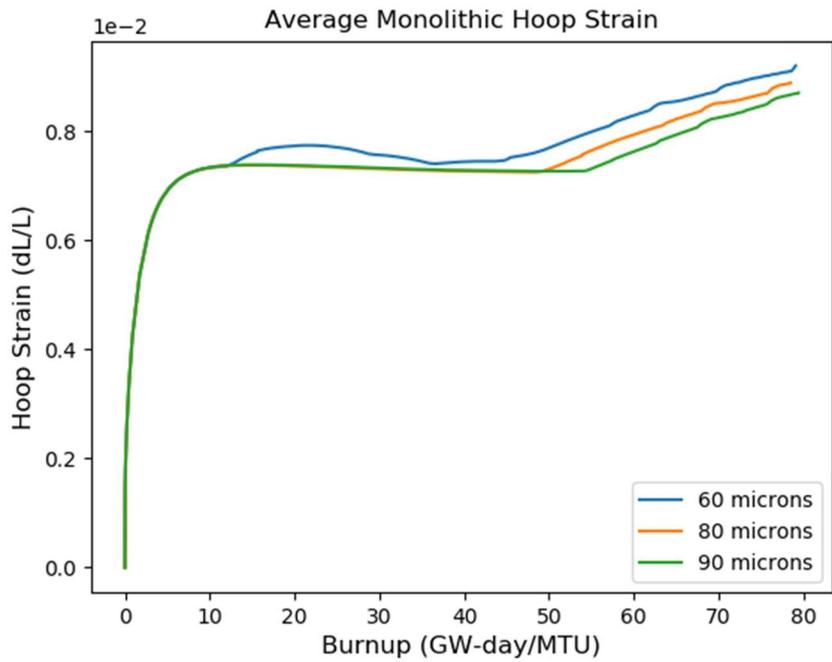
Figure 4.47: Cladding gap sensitivity on cladding hoop strain
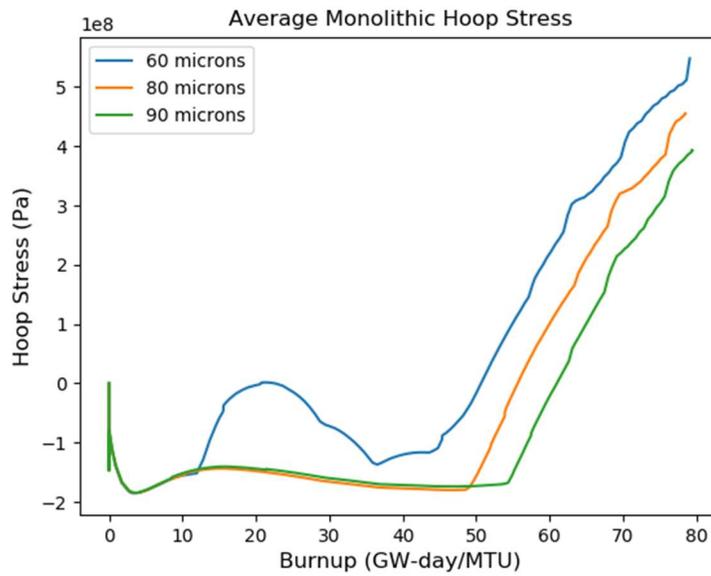
Figure 4.49: Cladding gap sensitivity on cladding hoop stress
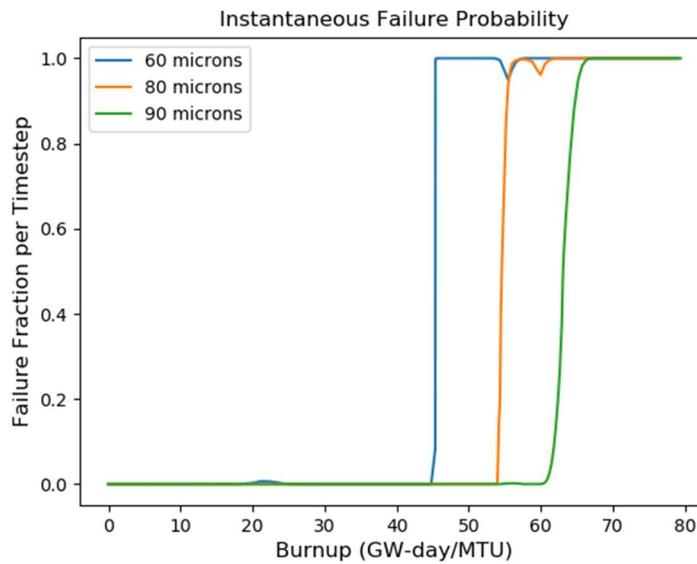
Figure 4.48: Cladding gap sensitivity on cladding failure probability

Figure 4.47 shows that with a cladding gap of 60 microns there is evidence of PCMI very early between 20-25 GW-day/MTU. As such a 60 micron gap is unacceptably small. Additionally, in Figure 4.44 the temperature gain by increasing the cladding gap to 90 microns is undesirable considering the relatively small 6 GW-day/MTU delay to

87

contact shown in Figure 4.47. These results indicate no compelling reason to increase

cladding gap much beyond 80 microns since other cladding design considerations

provide a larger delay to contact without compromising fuel temperatures.

Chapter 5 Conclusion

5.1 Thermal Creep Model
5.1.1 Nabarro-Herring

Original U3Si2 creep experimental data was used in this study to determine the thermal creep mechanism and develop an empirical model for use in finite element simulations. Evidence from statistical analysis of Mercado's thermal creep experiment strongly suggest a Nabarro-Herring diffusion creep mechanism. The reasons for this determination are:

1) High degree of correlation: N-H creep provides an r^2 value of 0.83 when the determined model is evaluated against the experimental data.

2) Very high statistical certainty: NH creep provides a p-value approaching zero. This result suggests that the probability of the model reflecting the data by random accident is nearly zero.

3) Calculated activation energy is 173.4 kJ/mol, a value that is similar to the weighted average of the self-diffusion energies of uranium and silicon in U3Si2 of 190.8 kJ/mol.

5.1.2 Mukherjee-Bird-Dorn

Though Nabarro-Herring creep is determined to be the predominant method of creep in Mercado's experiment, due to the presence of multiple creep modes, a more general empirical model is needed to capture the behavior of these creep mechanisms

for use in simulation. Thus, Equation 3.1 (A=4.841e-19, n=1.936, p=1.86, Q=223076 J/mol-K) is recommended for thermal creep modeling of U3Si2.

5.2 U3Si2 Design Priority

The completed BISON simulation shows that U3Si2-SiC fuel concept has marginal advantages in terms of steady state fuel operating temperatures and significant delay to contact compared to UO_2-Zry fuels. The steady state improvement in fuel temperatures is of minor benefit. Predicted fission product gas release over expected fuel lifetime is significantly lower than UO_2 and time to PCMI is vastly improved even under heightened power density conditions. These performance advantages are significant when combined with U3Si2's improved uranium densities.

However, the simulations completed in this study indicate that U3Si2, in combination with SiC cladding, are very likely to fail upon fuel-cladding contact. Despite the very long time to PCMI, it is unlikely that contact can be entirely avoided in all rods in a real core. Therefore, the U_3Si_2-SiC concept fuel performance advantages over traditional nuclear fuel are not enough to justify its use as a replacement for UO_2-Zry fuels.

The thermal creep sensitivity study completed in this work demonstrates that significant improvements to PCMI can be had when the fuel is behaves more plastically. Enhanced plasticity in U_3Si_2 would significantly reduce the probability of sudden monolithic SiC failure during PCMI. Since U_3Si_2 is an intermetallic, it seems likely that researchers could induce improved plasticity in the fuel without serious compromise. To the authors knowledge this line of research has yet to be pursued, though its lack of

development is understandable considering that consistent production of pure U3Si2 with highly controlled microstructure is a developing science.

5.3 Cladding Design Priority

Vast improvements to composite SiC design have resulted in a CMC that resists sudden failure. However, in the duplex SiC scheme with an outside environmental barrier of monolithic SiC, cracking of the monolithic SiC is still an eventuality upon contact with the fuel. Though efforts to improve composite SiC reduce the likelihood of monolithic SiC cladding failure, strategies to prevent contact are necessary in the U3Si2-SiC fuel concept.

The major priority to improve available lifetime of the fuel without cladding failure is to reduce composite SiC thickness. Improvements to thermal conductivity are also advantageous though less impactful as cladding thickness. A larger fuel to cladding gap may be used to reduce the probability of contact with the fuel, however, a nominal gap size of 80 microns provides adequate U3Si2-SiC fuel lifetime without failure through more than 50 GW-day/MTU under hot channel conditions and an initial LHGR of 44.62 kW/m.

References

[1]   K. E. Metzger, "Analysis of Pellet Cladding Interaction and Creep of U3Si2 Fuel for Use in Light Water Reactors," University Of South Carolina, Columbia, 2016.

[2]   F. Cappia and J. M. Harp, "Postirradiation examinations of low burnup U3Si2 fuel for light water reactor applications," Journal of Nuclear Materials, pp. 62-79, 2019.

[3]   J. T. White, Update to the U3Si2 Property Handbook, Los Alamos: U.S. Department of Energy, 2018.

[4]   E. A. C. Mercado, "High Temperature Compression Creep of U3Si2," University of South Carolina, Columbia, 2018.

[5]   J. G. Stone, R. Schleicher, C. P. Deck, G. M. Jacobsen, H. E. Khalifa and C. A. Back, "Stress analysis and probabilistic assessment of multi-layer SiC-based accident tolerant nuclear fuel cladding".

[6]   R. A. Freeman, "Analysis Of Pellet-Cladding Mechanical Interaction on U3Si2 Fuel With a Multi-Layer SiC Cladding Using BISON," University of South Carolina, Columbia, 2018.

[7]   Y. S. Kim and G. L. Hofman, "Interdiffusion in U3Si-Al, U3Si2-Al, and USi-Al dispersion fuels during irradiation," Journal of Nucleear Materials, pp. 1-9, 2011.

[8]   Y. Miao, K. A. Gamble, D. Andersson, B. Ye, Z.-G. Mei, G. Hofman and A. M. Yacout, "Gaseous swelling of U3Si2 during steady-state LWR operation: A rate theory investigation," Nuclear Engineeering and Design, pp. 336-344, 2017.

[9]   A. Mohamad, Y. Ohishi, H. Muta, K. Kurosaki and S. Yamanaka, "Thermal and mechanical properties of polycrystalline U3Si2 synthesized by spark plasma sintering," Journal of Suclear Science and Technology 55, pp. 1141-1150, 2018.

[10] E. G. Obbard, K. D. Johnson, P. A. Burr, D. A. Lopes, D. J. Gregg, K. D. Liss, G. Griffiths, N. Scales and S. C. Middleburgh, "Anisotropy in the thermal expansion of

uranium silicide measured by neutron diffraction," Journal of Nuclear Materials 508, pp. 516-520, 2018.

[11] Electric Power Research Institute, "Fuel Analysis and Licensing Code: FALCON MOD01: Volume 1: Theoretical and Numerical Bases," EPRI, 2004.

[12] T. Barani, G. Pastore, D. Pizzocri, C. Matthews, A. Alfonsi, K. A. Gamble, P. V. Uffelen, L. Luzzi and J. D. Hales, "Multiscale modeling of fission gas behavior in U3Si2 under LWR conditions".

[13] N. M. George, K. Terrani, J. Powers, A. Worrall and I. Maldonado, "Neutronic analysis of candidate accident-tolerant cladding concepts in pressurized water reactors," Annals of Nuclear Energy 75, pp. 703-712, 2015.

[14] L. L. Snead, T. Nozawa, Y. Katoh, T.-S. Byun, S. Kondo and D. A. Petti, "Handbook of SiC properties for fuel performance modeling," Journal of Nuclear Materials 371, pp. 329-377, 2007.

[15] G. Singh, S. Gonczy, C. Deck and E. Lara-Curzio, "Interlaboratory round robin study on axial tensile properties of SiC-SiC CMC tubular test specimens," International Journal of Applied Ceramic Technology, pp. 1334-1349, 2018.

[16] J. Braun, C. Sauder, J. Lamon and F. Balbaud-Célérier, "Influence of an original manufacturing process on the properties and microstructure of SiC/SiC tubular composites," Composites Part A 123, pp. 170-179, 2019.

[17] G. Singh, T. Koyanagi, C. Petrie, C. Deck, K. Terrani, J. D. Arregui-Mena and Y. Katoh, "Elastic moduli reduction in SiC-SiC tubular specimen after high heat flux neutron irradiation measured by resonant ultrasound spectroscopy," Journal of Nuclear Materials 523, pp. 391-401, 2019.

[18] T. Koyanagi, Y. Katoh, G. Jacobsen and C. Deck, "Handbook of LWR SiC/SiC Cladding Properties - Rev 1," Oak Ridge National Laboratory, 2018.

[19] Y. Katoh, K. Ozawa, C. Shih, T. Nozawa, R. J. Shinavski, A. Hasegawa and L. L. Snead, "Continuous SiC fiber, CVI SiC matrix composites for nuclear applications: Properties and irradiation effects," Journal of Nuclear Materials 488, pp. 448-476, 2014.

[20] Y. Katoh, T. Koyanagi, J. L. McDuffee, L. L. Snead and K. Yueh, "Dimensional stability and anisotropy of SiC and SiC-based composites in transition swelling regime," Journal of Nuclear Materials 499, pp. 471-479, 2018.

[21] T. Koyanagi, Y. Katoh, K. Ozawa, K. Shimoda, T. Hinoki and L. L. Snead, "Neutron-irradiation creep of silicon carbide materials beyond the initial transient," Journal of Nuclear Materials 478, pp. 97-111, 2016.

[22] T. Koyanagi, K. Terrani, T. Karlsen, V. Andersson, D. Sprouster, L. Ecker and Y. Katoh, "In-pile tensile creep of chemical vapor deposited silicon carbide at 300C," Journal of Nuclear Materials 521, pp. 63-70, 2019.

[23] C. A. Lewinsohn, M. L. Hamilton, G. E. Youngblood, R. H. Jones, F. A. Garner, S. L. Hecht and A. Kohyama, "Irradiation-enhanced creep in SiC: data summary and planned experiments," Journal of Nuclear Materials, pp. 36-46, 1998.

[24] Y. Katoh, T. Nozawa, C. Shih, K. Ozawa, T. Koyanagi, W. Porter and L. Snead, "High-Dose Neutron Irradiation of Hi-Nicalon Type S Silicon Carbide Composites Part 2: Mechanical and Physical Properties," Oak Ridge National Laboratory, 2014.

[25] D. J. Antonio, K. Shrestha, J. Harp, C. Adkins, Y. Zhang, J. Carmack and K. Gofryk, "Thermal and transport properties of U3Si2," Journal of Nuclear Materials 508, pp. 154-158, 2018.

[26] T. Wang, N. Qiu, X. Wen, Y. Tian, J. He, K. Luo, X. Zha, Y. Zhou, Q. Huang, J. Lang and S. Du, "First-principles investigations on the electronic structures of U3Si2," Journal of Nuclear Materials 469, pp. 194-199, 2016.

[27] M. F. Ashby and J. Frost, Deformation-mechanism maps, the Plasticity and Creep of Metals and Ceramics, Oxford: Pergamaon Press, 1982.

[28] Y. Harada and D. C. Dunand, "Creep Properties of Al3Sc and Al3Sc,x Intermetallics," Acta Materialia 48, pp. 3477-3487, 2000.

[29] M. A. Meyers and K. K. Chawla, Mechanical Behavior of Materials, Cambridge: Cambridge University Press, 2009.

[30] Q. Auzoux, L. Allais, C. Caes, I. Monnet, A. F. Gourgues and A. Pineau, "Effect of pre-strain on creep of three AISI 316 austenitic stainless steels in relation to reheat cracking of weld-affected zones," Journal of Nuclear Materials 400, pp. 127-137,

2010.

[31] R. B. Fancher, I. B. Fiero, H. Freeburn, A. M. Garde, M. W. Kennard, M. A. Krammen, P. G. Smerd and N. T. Yackle, "ESCORE: the EPRI steady-state core reload evaluator code: General description: Final report," Oak Ridge National Laboratory, 1987.

[32] M. Meyers and K. Chawla, "Fracture Mechanics," in Mechanical Behavior of Materials 2nd Edition, New York, Cambridge University Press, 2008, p. 426.

[33] Idaho National Laboratory, "Exponential Softening," [Online]. Available: https://bison.inl.gov/Documentation/source/materials/ExponentialSoftening.aspx. [Accessed 01 08 2019].

[34] G. Singh, K. Terrani and Y. Katoh, "Thermo-mechanical assessment of full SiC/SiC composite cladding for LWR applications with sensitivity analysis," Journal of Nuclear Materials, vol. 499, pp. 26-143, 2018.

[35] N. E. Todreas and M. S. Kazimi, Nuclear Systems: Volume 1 2nd Edition, Boca Raton: CRC Press, 2011.

[36] S. Liu, J. Liang, Q. Wu, J. Guo, S. Huang, X. Tang, Z. Li and K. Wang, "BEAVRS full core burnup calculation in hot full power condition by RMC code," Annals of Nuclear Energy, vol. 101, pp. 434-446, 2017.

[37] J. D. Stempien, D. M. Carpenter, G. Kohse and M. Kazimi, "Characteristics of Composite Silicon Carbide Fuel Cladding after Irradiation under Simulated PWR Conditions," Nuclear Technology, vol. 183, no. 1, pp. 13-29, 2017.

[38] Dartmouth University, "Chapter 2: Rate Equations," [Online]. Available: http://engineering.dartmouth.edu/defmech/chapter_2.htm. [Accessed 17 09 2019].

[39] D. Andersson, C. Stanek, M. Noordhoek, T. M. Besmann, S. Middleburgh, E. J. Lahoda, A. Chernatynskiy and R. Grimes, "Modeling defect and fission gas properties in U-Si fuels," Los Alamos National Laboratory, 2017.

[40] J. A. Sharon and B. L. Boyce, "Concepts on Low Temperature Mechanical Grain Growth," Sandia National Laboratory, Albuquerque, 2013.

[41] R. E. Hoggan, K. R. Tolman, F. Cappia, A. R. Wagner and J. M. Harp, "Grain size and

phase purity characterization of U3Si2 fuel pellets," Journal of Nuclear Materials, vol. 512, pp. 199-213, 2018.

[42] Y. Deng , D. Shirvan, Y. Wu and G. Su, "Probabilistic view of SiC-SiC composite cladding failure based on full core thermo-mechanical response," Journal of Nuclear Materials, vol. 507, pp. 24-37, 2018.

[43] H. Shimizu, "The properties and irradiation behavior of U3Si2," Atomics International, Canoga Park, 1965.
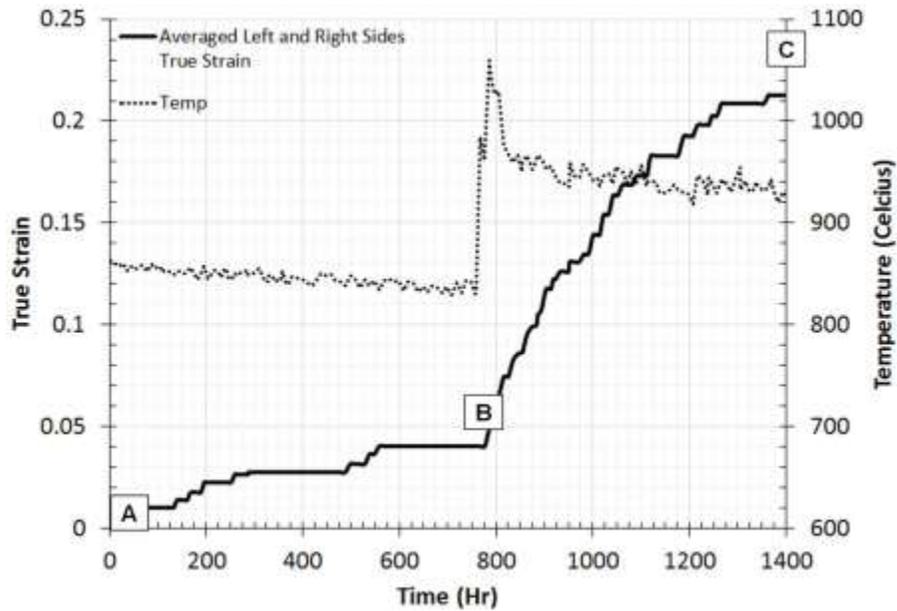
Appendix A: U3Si2 Compressive Creep Data From Mercado 2018

Strain and Temperature vs Time

Sample 150813a (Tests 1-3)
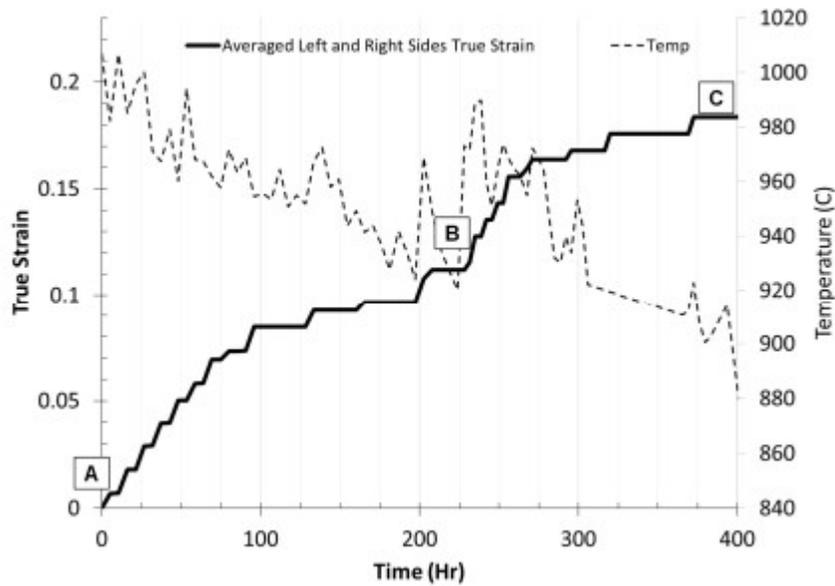
Sample 150813b (Test 4-5)

Sample 161214b (Tests 6-7)

Sample 161214a (Tests 8-10)

Sample 161214c (Tests 11-13)

Pressure and Stress vs Time
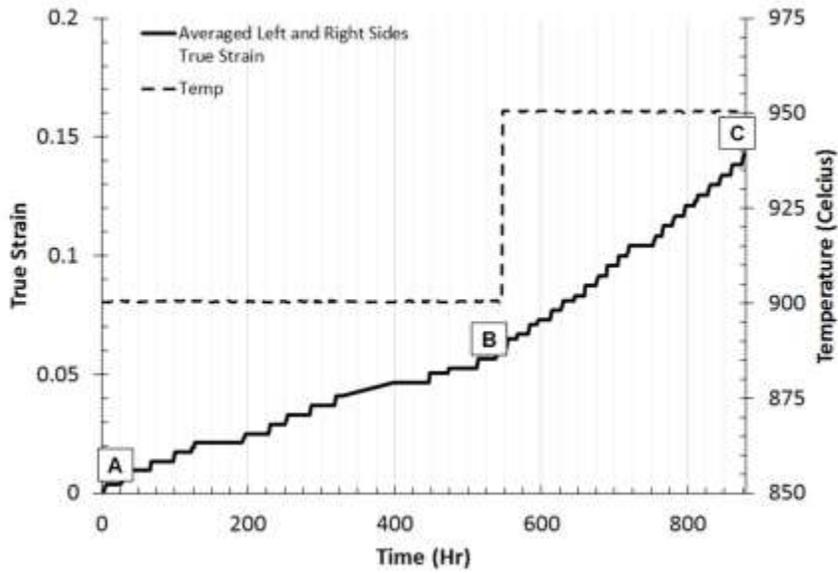
Sample 150813a (Tests 1-3)
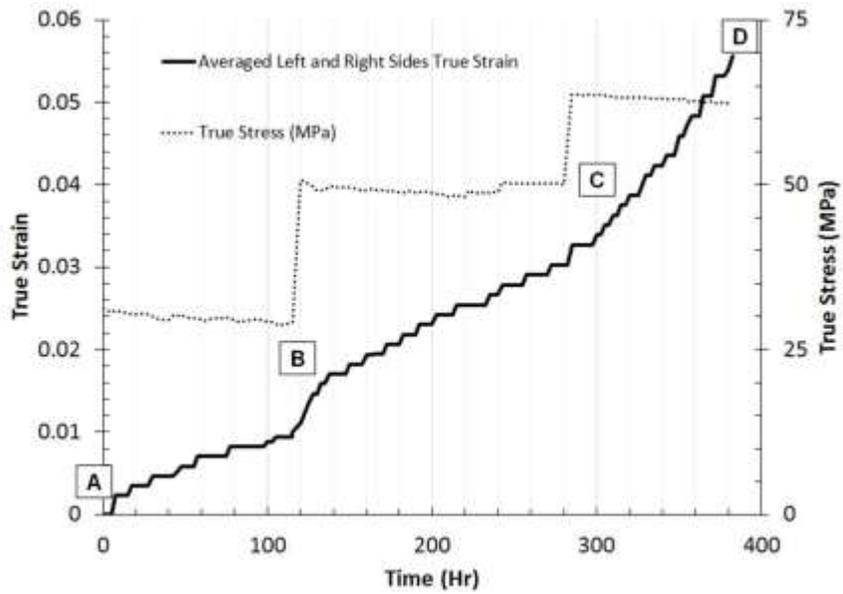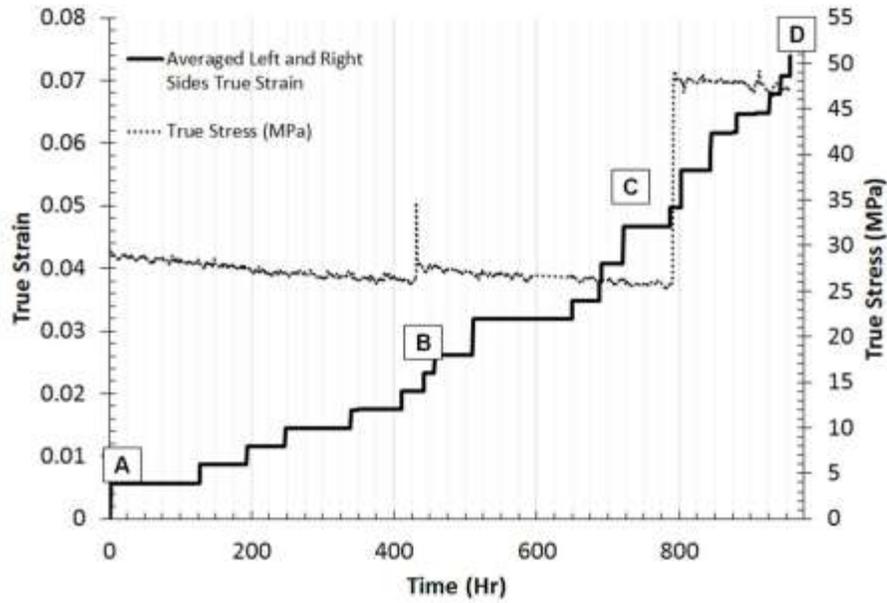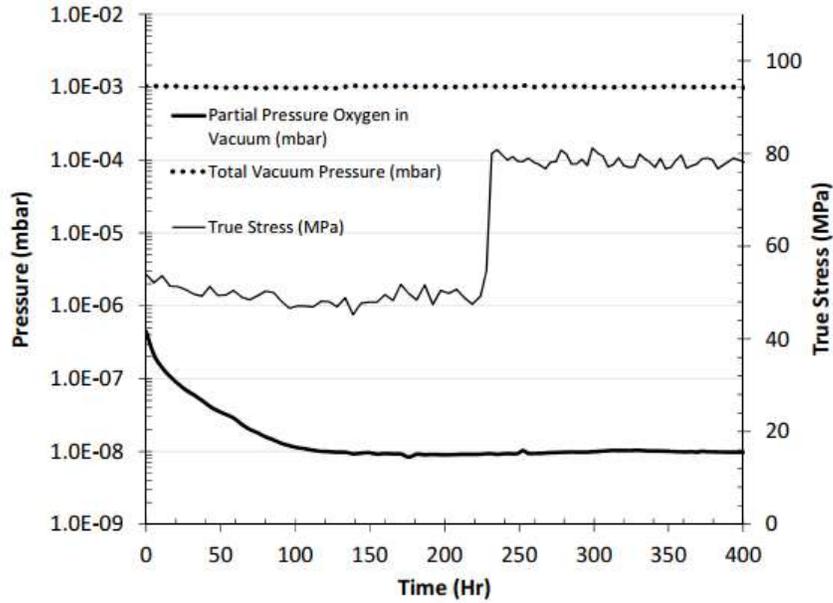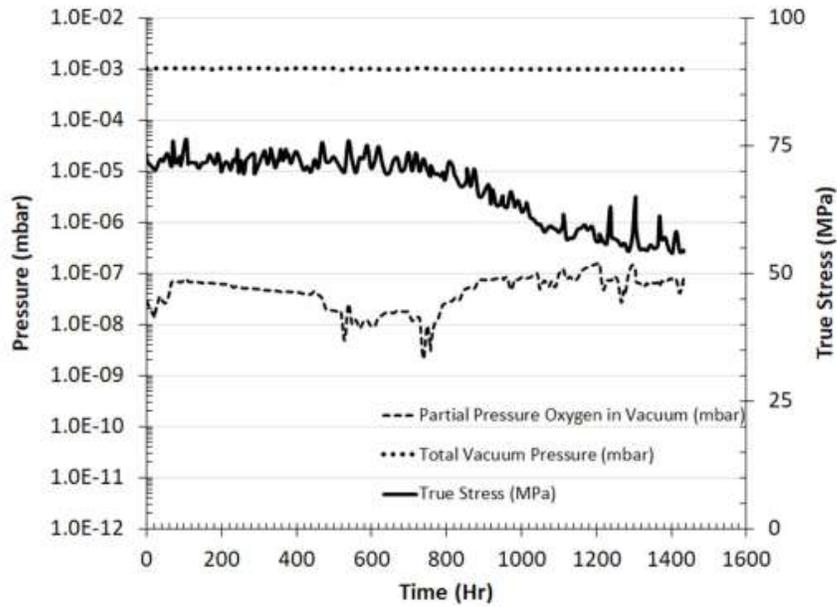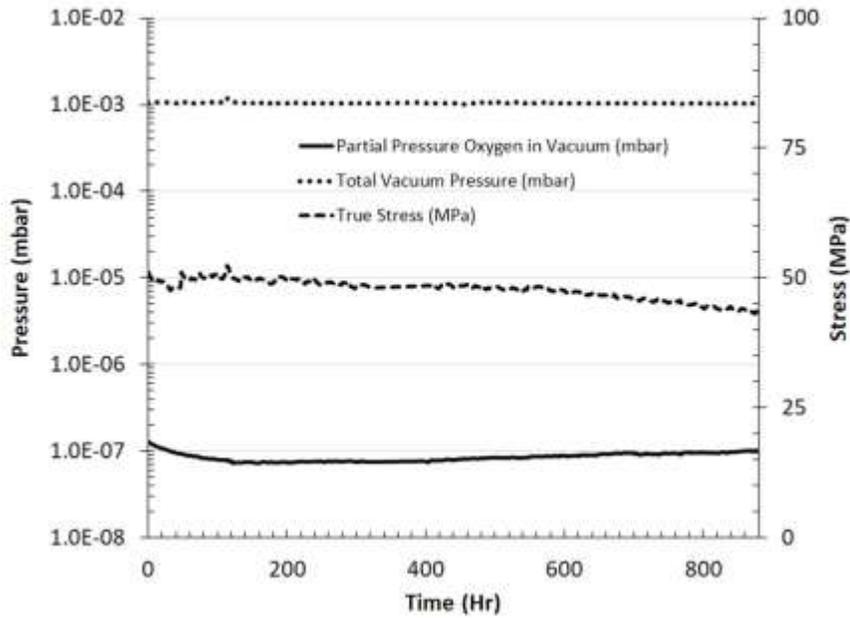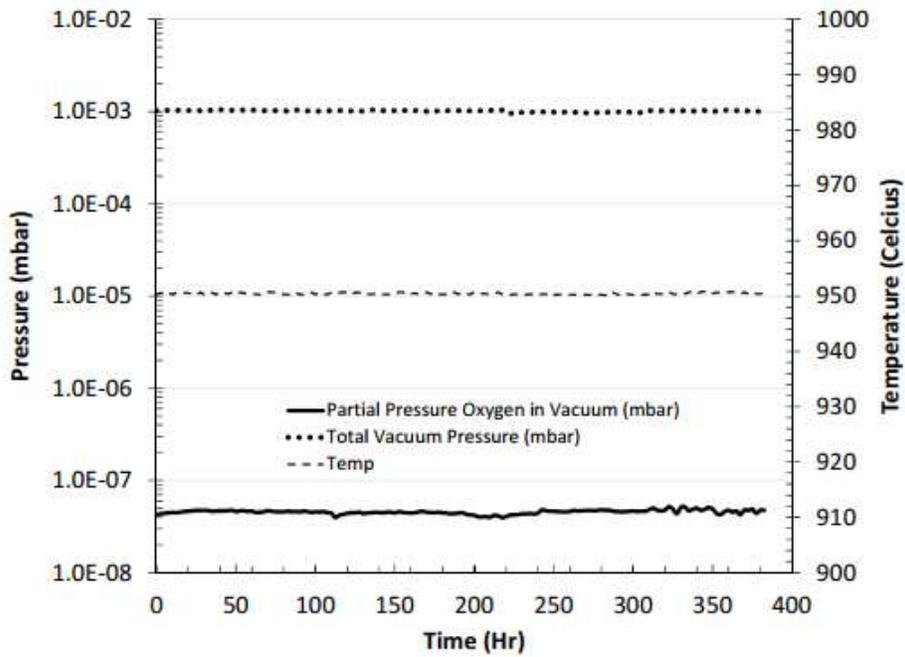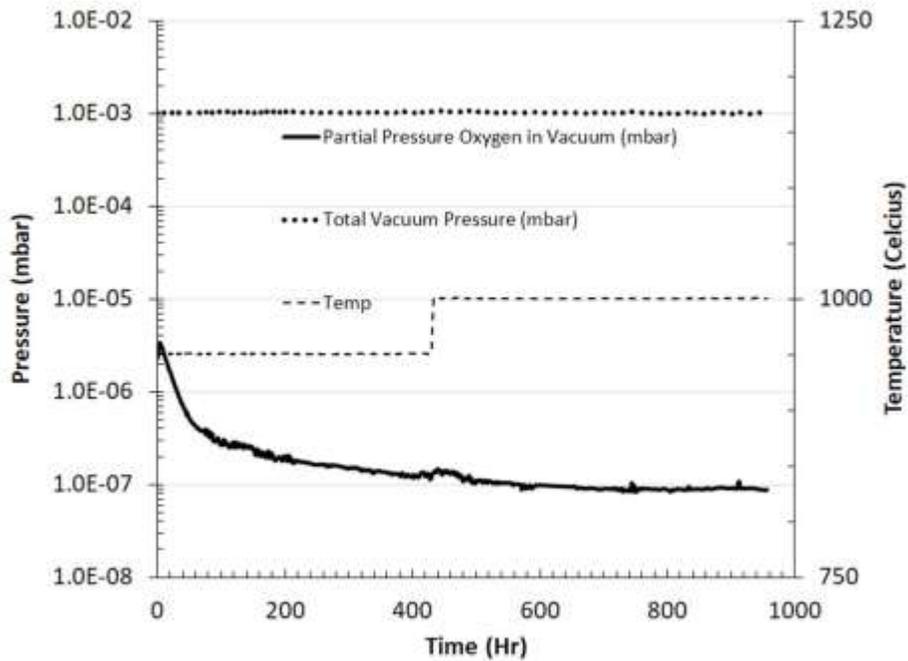
Sample 150813b (Test 4-5)

Sample 161214b (Tests 6-7)

Sample 161214a (Tests 8-10)

Sample 161214c (Tests 11-13)

Appendix B: Example Python 2.3 Code for Data Processing

The following python 2.3 template code is provided to show how the experimental data was handled.

```
from pylab import *
from openpyxl import load_workbook
from scipy import stats

numOfTests = 3

# Load in information from workbook
wb = load_workbook(filename = 'pellet1.xlsx',data_only=True)
ws = wb['data']

numRows = ws.max_row

time = zeros(numRows-1)
temperature = zeros(numRows-1)
eng_stress = zeros(numRows-1)
true_stress = zeros(numRows-1)
left_vert_eng_strain = zeros(numRows-1)
right_vert_eng_strain = zeros(numRows-1)
top_horz_eng_strain = zeros(numRows-1)
bottom_horz_eng_strain = zeros(numRows-1)
left_vert_true_strain = zeros(numRows-1)
right_vert_true_strain = zeros(numRows-1)
top_horz_true_strain = zeros(numRows-1)
bottom_horz_true_strain = zeros(numRows-1)
avg_vert_eng_strain = zeros(numRows-1)
avg_vert_true_strain = zeros(numRows-1)
avg_horz_eng_strain = zeros(numRows-1)
avg_horz_true_strain = zeros(numRows-1)

strain_holder = zeros(numOfTests)

for i in range(2,numRows+1,1):
    time[i-2] = ws.cell(row=i,column=3).value
    temperature[i-2] = ws.cell(row=i,column=4).value
    eng_stress[i-2] = ws.cell(row=i,column=5).value
    true_stress[i-2] = ws.cell(row=i,column=6).value
    left_vert_eng_strain[i-2] = ws.cell(row=i,column=19).value
```

```
    right_vert_eng_strain[i-2] = ws.cell(row=i,column=20).value
    top_horz_eng_strain[i-2] = ws.cell(row=i,column=21).value
    bottom_horz_eng_strain[i-2] = ws.cell(row=i,column=22).value
    left_vert_true_strain[i-2] = ws.cell(row=i,column=23).value
    right_vert_true_strain[i-2] = ws.cell(row=i,column=24).value
    top_horz_true_strain[i-2] = ws.cell(row=i,column=25).value
    bottom_horz_true_strain[i-2] = ws.cell(row=i,column=26).value
    avg_vert_eng_strain[i-2] = ws.cell(row=i,column=27).value
    avg_vert_true_strain[i-2] = ws.cell(row=i,column=28).value
    avg_horz_eng_strain[i-2] = ws.cell(row=i,column=29).value
    avg_horz_true_strain[i-2] = ws.cell(row=i,column=30).value

testRanges = zeros(2*numOfTests)

for i in range(2,2*numOfTests+2,1):
    testRanges[i-2] = ws.cell(row=i,column=31).value


time_frame = 100.0*3600.0
sample_seating = 100.0*3600.0
skip_time = 20.0*3600.0

labels = array(["null","null"])
for i in range(1,numOfTests,1):
    labels = append(labels,"null")
    labels = append(labels,"null")

color1 = array(['b','g','r'])
color2 = array(['b--','g--','r--'])
color3 = array(['c','m','k'])

for i in range(0,numOfTests,1):
    if i == 0:
        skip = sample_seating
    else:
        skip = skip_time

    lowBounds = int(testRanges[i*2])
    highBounds = int(testRanges[i*2+1])
    time_temp = time[lowBounds-2:highBounds-1]
    temperature_temp = temperature[lowBounds-2:highBounds-1]
    eng_stress_temp = eng_stress[lowBounds-2:highBounds-1]
    true_stress_temp = true_stress[lowBounds-2:highBounds-1]
    left_vert_eng_strain_temp = left_vert_eng_strain[lowBounds-2:highBounds-1]
    right_vert_eng_strain_temp = right_vert_eng_strain[lowBounds-2:highBounds-1]
    top_horz_eng_strain_temp = top_horz_eng_strain[lowBounds-2:highBounds-1]
    bottom_horz_eng_strain_temp = bottom_horz_eng_strain[lowBounds-2:highBounds-1]
    left_vert_true_strain_temp = left_vert_true_strain[lowBounds-2:highBounds-1]
```

```
right_vert_true_strain_temp = right_vert_true_strain[lowBounds-2:highBounds-1]
top_horz_true_strain_temp = top_horz_true_strain[lowBounds-2:highBounds-1]
bottom_horz_true_strain_temp = bottom_horz_true_strain[lowBounds-2:highBounds-1]
avg_vert_eng_strain_temp = avg_vert_eng_strain[lowBounds-2:highBounds-1]
avg_vert_true_strain_temp = avg_vert_true_strain[lowBounds-2:highBounds-1]
avg_horz_eng_strain_temp = avg_horz_eng_strain[lowBounds-2:highBounds-1]
avg_horz_true_strain_temp = avg_horz_true_strain[lowBounds-2:highBounds-1]

print avg_vert_true_strain_temp[-1]

test1 = "Test"
test2 = str(i+1)
labels[i*2] = test1
labels[i*2 + 1] = test2

max_r = 0.0

for j in range(1,size(time_temp),1):
    time_accum = 0.0
    count = 0
    time_array = array([time_temp[j-1]])
    strain_array = array([avg_vert_true_strain_temp[j-1]])
    temp_array = array([temperature_temp[j-1]])
    stress_array = array([true_stress_temp[j-1]])
    full_range = True
    while time_accum < time_frame:
        if count+j < size(time_temp):
            time_array = append(time_array,time_temp[count+j])
            strain_array = append(strain_array,avg_vert_true_strain_temp[count+j])
            temp_array = append(temp_array,temperature_temp[count+j])
            stress_array = append(stress_array,true_stress_temp[count+j])
            time_accum += time_temp[count+j]-time_temp[count+j-1]

            count += 1
        else:
            full_range = False
            break
    slope,intercept,r_value,p_value,std_err = stats.linregress(time_array,strain_array)
    if r_value > max_r and full_range==True and time_temp[j] > skip+time_temp[0]:
        max_r = r_value
        f = polyfit(time_array,strain_array,1)
        strain_new = f[0]*time_array + f[1]
        time_new = time_array
        temp_new = temp_array
        stress_new = stress_array


temperature_plot = figure("Temperature")
```

```python
    temperature_plot_ax = temperature_plot.add_subplot(1, 1, 1)
    if time_temp[-1] - time_temp[0] > skip+time_frame:
        temperature_plot_ax.plot(time_temp,temperature_temp,color1[i],label=labels[i*2] + " " +
labels[i*2+1] + " (" + '{:.2f}'.format(average(temp_new)) + " $^\circ$C)")
        temperature_plot_ax.plot([time_new[0],time_new[-
1]],[average(temp_new),average(temp_new)],color2[i])
    else:
        temperature_plot_ax.plot(time_temp,temperature_temp,color1[i],label=labels[i*2] + " " +
labels[i*2+1] + " (N/A)")

    eng_stress_plot = figure("Engineering Stress")
    eng_stress_plot_ax = eng_stress_plot.add_subplot(1, 1, 1)
    eng_stress_plot_ax.plot(time_temp,eng_stress_temp,label=labels[i*2] + " " + labels[i*2+1])

    true_stress_plot = figure("True Stress")
    true_stress_plot_ax = true_stress_plot.add_subplot(1, 1, 1)
    if time_temp[-1] - time_temp[0] > skip+time_frame:
        true_stress_plot_ax.plot(time_temp,true_stress_temp,color1[i],label=labels[i*2] + " " +
labels[i*2+1] + " (" + '{:.2f}'.format(average(stress_new)) + " MPa) - True")
        true_stress_plot_ax.plot([time_new[0],time_new[-
1]],[average(stress_new),average(stress_new)],color2[i])
    else:
        true_stress_plot_ax.plot(time_temp,true_stress_temp,color1[i],label=labels[i*2] + " " +
labels[i*2+1] + " (N/A) - True")
    true_stress_plot_ax.plot(time_temp,eng_stress_temp,color3[i],label=labels[i*2] + " " +
labels[i*2+1] + " - Engineering")

    left_vert_eng_strain_plot = figure("Left/Right Vertical Engineering Strain")
    left_vert_eng_strain_plot_ax = left_vert_eng_strain_plot.add_subplot(1, 1, 1)

left_vert_eng_strain_plot_ax.plot(time_temp,left_vert_eng_strain_temp,color1[i],label=labels[i
*2] + " " + labels[i*2+1] + " - Left")

left_vert_eng_strain_plot_ax.plot(time_temp,right_vert_eng_strain_temp,color1[i],label=labels
[i*2] + " " + labels[i*2+1] + " - Right")

    top_horz_eng_strain_plot = figure("Top Horizontal Engineering Strain")
    top_horz_eng_strain_plot_ax = top_horz_eng_strain_plot.add_subplot(1, 1, 1)

top_horz_eng_strain_plot_ax.plot(time_temp,top_horz_eng_strain_temp,color1[i],label=labels[
i*2] + " " + labels[i*2+1] + " - Top")

top_horz_eng_strain_plot_ax.plot(time_temp,bottom_horz_eng_strain_temp,color1[i],label=la
bels[i*2] + " " + labels[i*2+1] + " - Bottom")

    left_vert_true_strain_plot = figure("Left Vertical True Strain")
    left_vert_true_strain_plot_ax = left_vert_true_strain_plot.add_subplot(1, 1, 1)
```

```python
left_vert_true_strain_plot_ax.plot(time_temp,left_vert_true_strain_temp,color1[i],label=labels[
i*2] + " " + labels[i*2+1] + " - Left")

left_vert_true_strain_plot_ax.plot(time_temp,right_vert_true_strain_temp,color1[i],label=label
s[i*2] + " " + labels[i*2+1] + " - Right")

    top_horz_true_strain_plot = figure("Top Horizontal True Strain")
    top_horz_true_strain_plot_ax = top_horz_true_strain_plot.add_subplot(1, 1, 1)

top_horz_true_strain_plot_ax.plot(time_temp,top_horz_true_strain_temp,color1[i],label=labels
[i*2] + " " + labels[i*2+1] + " - Top")

top_horz_true_strain_plot_ax.plot(time_temp,bottom_horz_true_strain_temp,color1[i],label=la
bels[i*2] + " " + labels[i*2+1] + " - Bottom")

    avg_vert_eng_strain_plot = figure("Average Vertical Engineering Strain")
    avg_vert_eng_strain_plot_ax = avg_vert_eng_strain_plot.add_subplot(1, 1, 1)
    avg_vert_eng_strain_plot_ax.plot(time_temp,avg_vert_eng_strain_temp,label=labels[i*2] + "
" + labels[i*2+1])

    avg_vert_true_strain_plot = figure("Average Vertical True Strain")
    avg_vert_true_strain_plot_ax = avg_vert_true_strain_plot.add_subplot(1, 1, 1)
    if time_temp[-1] - time_temp[0] > skip+time_frame:

avg_vert_true_strain_plot_ax.plot(time_temp,avg_vert_true_strain_temp,color1[i],label=labels[
i*2] + " " + labels[i*2+1] + " (" + '{:.4E}'.format(f[0]) + " 1/s, r = " + '{:.2f}'.format(max_r) + ")")
        avg_vert_true_strain_plot_ax.plot(time_new,strain_new,color2[i],linewidth=2)
        strain_holder[i] = f[0]
    else:

avg_vert_true_strain_plot_ax.plot(time_temp,avg_vert_true_strain_temp,color1[i],label=labels[
i*2] + " " + labels[i*2+1] + " (N/A)")

    avg_horz_eng_strain_plot = figure("Average Horizontal Engineering Strain")
    avg_horz_eng_strain_plot_ax = avg_horz_eng_strain_plot.add_subplot(1, 1, 1)
    avg_horz_eng_strain_plot_ax.plot(time_temp,avg_horz_eng_strain_temp,label=labels[i*2] + "
" + labels[i*2+1])

    avg_horz_true_strain_plot = figure("Average Horizontal True Strain")
    avg_horz_true_strain_plot_ax = avg_horz_true_strain_plot.add_subplot(1, 1, 1)
    avg_horz_true_strain_plot_ax.plot(time_temp,avg_vert_true_strain_temp,color1[i]+'--
',label=labels[i*2] + " " + labels[i*2+1] + " - Axial")

avg_horz_true_strain_plot_ax.plot(time_temp,avg_horz_true_strain_temp,color1[i],label=labels
[i*2] + " " + labels[i*2+1] + " - Diametral")

temperature_plot_ax.legend(loc=2)
```

```python
temperature_plot_ax.set_xlabel("Time (s)",fontsize=16)
temperature_plot_ax.set_ylabel("Temperature ($^\circ$C)",fontsize=16)
temperature_plot_ax.ticklabel_format(style='sci', axis='x', scilimits=(0,0))
temperature_plot.tight_layout()
temperature_plot.savefig("temperature.png")

eng_stress_plot_ax.legend(loc=4)
eng_stress_plot_ax.set_xlabel("Time (s)",fontsize=16)
eng_stress_plot_ax.set_ylabel("Engineering Stress (MPa)",fontsize=16)
eng_stress_plot_ax.ticklabel_format(style='sci', axis='x', scilimits=(0,0))
eng_stress_plot.tight_layout()
eng_stress_plot.savefig("eng_stress.png")

true_stress_plot_ax.legend(loc=3)
true_stress_plot_ax.set_xlabel("Time (s)",fontsize=16)
true_stress_plot_ax.set_ylabel("Stress (MPa)",fontsize=16)
true_stress_plot_ax.ticklabel_format(style='sci', axis='x', scilimits=(0,0))
true_stress_plot.tight_layout()
true_stress_plot.savefig("true_stress.png")

left_vert_eng_strain_plot_ax.legend(loc=2)
left_vert_eng_strain_plot_ax.set_xlabel("Time (s)",fontsize=16)
left_vert_eng_strain_plot_ax.set_ylabel("Engineering Strain",fontsize=16)
left_vert_eng_strain_plot_ax.ticklabel_format(style='sci', axis='x', scilimits=(0,0))
left_vert_eng_strain_plot.tight_layout()
left_vert_eng_strain_plot.savefig("left_right_vert_eng_strain.png")

top_horz_eng_strain_plot_ax.legend(loc=2)
top_horz_eng_strain_plot_ax.set_xlabel("Time (s)",fontsize=16)
top_horz_eng_strain_plot_ax.set_ylabel("Engineering Strain",fontsize=16)
top_horz_eng_strain_plot_ax.ticklabel_format(style='sci', axis='x', scilimits=(0,0))
top_horz_eng_strain_plot.tight_layout()
top_horz_eng_strain_plot.savefig("top_bottom_horz_eng_strain.png")

left_vert_true_strain_plot_ax.legend(loc=2)
left_vert_true_strain_plot_ax.set_xlabel("Time (s)",fontsize=16)
left_vert_true_strain_plot_ax.set_ylabel("True Strain",fontsize=16)
left_vert_true_strain_plot_ax.ticklabel_format(style='sci', axis='x', scilimits=(0,0))
left_vert_true_strain_plot.tight_layout()
left_vert_true_strain_plot.savefig("left_right_vert_true_strain.png")

top_horz_true_strain_plot_ax.legend(loc=2)
top_horz_true_strain_plot_ax.set_xlabel("Time (s)",fontsize=16)
top_horz_true_strain_plot_ax.set_ylabel("True Strain",fontsize=16)
top_horz_true_strain_plot_ax.ticklabel_format(style='sci', axis='x', scilimits=(0,0))
top_horz_true_strain_plot.tight_layout()
top_horz_true_strain_plot.savefig("top_bottom_horz_true_strain.png")
```

```
avg_vert_eng_strain_plot_ax.legend(loc=2)
avg_vert_eng_strain_plot_ax.set_xlabel("Time (s)",fontsize=16)
avg_vert_eng_strain_plot_ax.set_ylabel("Engineering Strain",fontsize=16)
avg_vert_eng_strain_plot_ax.ticklabel_format(style='sci', axis='x', scilimits=(0,0))
avg_vert_eng_strain_plot.tight_layout()
avg_vert_eng_strain_plot.savefig("avg_vert_eng_strain.png")

avg_vert_true_strain_plot_ax.legend(loc=4)
avg_vert_true_strain_plot_ax.set_xlabel("Time (s)",fontsize=16)
avg_vert_true_strain_plot_ax.set_ylabel("True Strain",fontsize=16)
avg_vert_true_strain_plot_ax.ticklabel_format(style='sci', axis='x', scilimits=(0,0))
avg_vert_true_strain_plot.tight_layout()
avg_vert_true_strain_plot.savefig("avg_vert_true_strain.png")

avg_horz_eng_strain_plot_ax.legend(loc=4)
avg_horz_eng_strain_plot_ax.set_xlabel("Time (s)",fontsize=16)
avg_horz_eng_strain_plot_ax.set_ylabel("Engineering Strain",fontsize=16)
avg_horz_eng_strain_plot_ax.ticklabel_format(style='sci', axis='x', scilimits=(0,0))
avg_horz_eng_strain_plot.tight_layout()
avg_horz_eng_strain_plot.savefig("avg_horz_eng_strain.png")

avg_horz_true_strain_plot_ax.legend(loc=2)
avg_horz_true_strain_plot_ax.set_xlabel("Time (s)",fontsize=16)
avg_horz_true_strain_plot_ax.set_ylabel("True Strain",fontsize=16)
avg_horz_true_strain_plot_ax.ticklabel_format(style='sci', axis='x', scilimits=(0,0))
avg_horz_true_strain_plot.tight_layout()
avg_horz_true_strain_plot.savefig("avg_horz_true_strain.png")

savetxt("results.txt",strain_holder)
```